EFFECTS OF INTERNAL WAVES AND TURBULENT FLUCTUATIONS ON UNDERWATER ACOUSTIC PROPAGATION

A thesis submitted
by
Stefanie E. Wojcik
to
WORCESTER POLYTECHNIC INSTITUTE
in partial fulfillment of the requirement for the degree of
MASTER OF SCIENCE
in
Mechanical Engineering

Stefanie E. Wojcik

March 03, 2006

Approved by:

Dr. William W. Durgin, Advisor

Dr. Michael A. Demetriou, Committee Member

Dr. David J. Olinger, Committee Member

Dr. M. Padmanabhan, Committee Member

Dr. Mark W. Richman, Graduate Committee Representative

Abstract

A predictive methodology for received signal variation as a function of ocean perturbations is developed using a ray-based analysis of the effects of internal waves and ocean turbulence on long and short range underwater acoustic propagation. In the present formulation the eikonal equations are considered in the form of a second-order, nonlinear ordinary differential equation with harmonic excitation due to an internal wave. The harmonic excitation is taken imperfect, i.e., with a random phase modulation due to Gaussian white noise, accounting for both chaotic and stochastic behavior. Simulated turbulence is represented using the potential theory line vortex approach. Simulations are conducted for long range propagation, 1000km, containing internal wave fields with added deterministic effects and are compared to those fields with non-deterministic properties. These results show that long range acoustic propagation has a very strong dependence on the intensity of deterministic fluctuations. Numerical analysis for short range propagation, 10km, was constructed for sound passage through the following perturbation scenarios: simulated turbulence, an internal wave field, and a field of internal waves and simulated turbulence combined. Investigation over varied initial conditions and perturbation strengths suggests internal wave environments supply the majority of spatial variation and turbulent eddy fields are primarily responsible for delay fluctuation. Spectra of the variations in mean travel velocity reveal internal wave dominance to be dependent on the intensity of the wave.

Acknowledgements

This work is primarily supported by the G.I. Alden fellowship, an endowed fund created by G.I. Alden to promote the advancement of hydraulic research at Worcester Polytechnic Institute.

I would like to express my sincere gratitude to my advisor, Professor W. Durgin, for his guidance during this thesis work, as well as for the financial support. Your encouragement and assistance throughout my graduate career has inspired me to work harder and extend my capabilities to the fullest. I will apply both your academic and life advice to all of my future endeavors. Also, a great deal of thanks to T. Andreeva, without your knowledge and prior research, this project would not have been possible. I would also like to acknowledge Professors M. Demetriou, D. Olinger, M. Padmanabhan, and M. Richman for all of your valuable input and for serving on this thesis committee.

Special thanks to B. St. Rock, S. Alexander, K. Liadis, B. Edilberti, B. Furman, P. St. Louis, N. Hickman, E. Soltan, G. Hayes, and S. Najafi, for your friendship. You have truly made this experience both worthwhile and memorable for me. Thank You.

Table of Contents

Table of Figures

Table of Tables

Nomenclature

A	Amplitude of internal wave
$A(z)$	Amplitude of plane wave
B	Stratification scale depth
C	Universal Kolmogorov constant
$c(z)$	Sound velocity as a function of depth
c_0	reference sound speed
c_{ch}	Speed of sound at sound channel axis
D_1	Noise intensity for ξ
D_2	Noise intensity for ς
$E(f)$	Energy as a function of frequency
$E(k)$	Energy as a function of wavenumber
$E(k,m)$	Garrett-Munk Spectrum of internal waves
$F(z,r)$	Forcing Function
f	Frequency
$H(z,p)$	Classical Hamiltonian
$H_{PE}(z,p)$	Hamiltonian for Parabolic Approximation
k	Wavenumber
L_o	Ozmidov length scale
ℓ	Inertial length scale
m	Vertical components of the wavevector

m^*	Reference vertical wavenumber
N	Brunt-Väisälä frequency
P	Pressure
p	Ray momentum
$q(r)$	Phase of internal wave
R	Wavelength of internal wave
$R(\tau)$	Autocovariance
$R_N(\tau)$	Autocorrelation function
r	Range
r_{vortex}	Radial Polar Coordinate
Re	Reynolds number
S	Salinity
T	Temperature
$T(z)$	Classical action variable
U_{L_o}	Ozmidov velocity scale
U_∞	Ambient flow velocity
$u(\ell)$	Inertial velocity scale
$u(r,z,t)$	Horizontal velocity of vortex array
u_η	Kolmogorov velocity scale
$V(z)$	Potential Energy
$v_r(t)$	Flow velocity at fixed point in time
$v_{r_{vortex}}$	Eddy induced velocity in radial direction

$v_{\theta_{vortex}}$	Eddy induced velocity in angular direction
z	Depth
z_a	Depth of sound channel axis
Γ	Circulation
γ_a	Adiabatic velocity gradient
ε	Dissipation rate
ε_{ssp}	Perturbation Coefficient
θ_{vortex}	Angular Polar Coordinate
ς	Gaussian white noise parameter for phase of internal wave
η	Kolmogorov length scale
λ	Acoustic Wavelength
ν	Kinematic viscosity
ξ	Gaussian white noise parameter for phase of internal wave
σ^2	Variance
τ	Travel time
$\tau(\ell)$	Inertial time scale
τ_{L_o}	Ozmidov time scale
τ_η	Kolmogorov time scale
ϕ	Ray angle measured with respect to the horizon
X	Eddy perturbation strength
ψ	Acoustic wave

ω	Angular frequency of acoustic source
ω_{vortex}	Vorticity of line vortex

Superscripts

‘	Turbulent Fluctuations
¯	Time averaged mean

1 INTRODUCTION

The ocean is a random medium having both deterministic and nondeterministic characteristics. This behavior often leads to difficulty in performing such underwater applications as telemetry and tomography. These methods involve sound wave propagation as a means to study and monitor the ocean medium or serve as a means of underwater communication.

1.1 Limitations of Acoustic Telemetry

Since its development in the 1940s, acoustic telemetry has most commonly been used by the Navy to support underwater communication. In recent years however, its use has gained commercial interest. Potential applications for both commercial and private use include: autonomous underwater vehicles (AUV), underwater acoustic networks (acoustic modems), tsunami early warning systems, and simultaneous data transmissions (EvoLogics, 2006). These applications require high bit rates, low error probability and long distance capabilities which are extremely difficult to achieve, given the ocean is a highly complex medium (Baggeroer, 1984). The ocean acoustic channel creates strong amplitude and phase fluctuations in acoustic transmissions. These fluctuations can be induced by internal waves, turbulence, temperature gradients, density stratification or by other related phenomena that cause local perturbations in the sound speed. Perturbations interact with the regular wave fronts through diffractive and refractive effects, causing temporal, spatial, and frequency-dependant fluctuations in the received waveforms, there are also multiple propagation paths from transmitter to receiver for most underwater propagation geometries (Catipovic, 1990). Received signal fluctuations arise from these medium fluctuations and cause the signal to oftentimes become unreadable. These underwater acoustic communications systems rely heavily on having prior knowledge of the underwater acoustic environment. Predictions of pulse behavior may also aid in developing smoothing or filtering techniques of the waveforms. This information will directly impact the optimality of receiver design, as well as the actual information rate that the underwater channel can support (Gendron, 2005).

1.2 Limitations of Acoustic Tomography

The state of the ocean traversed by a sound pulse or sound field can be reconstructed from precise measurements of the travel times, or from other properties of acoustic propagation (Munk & Wunsch, 1979). Tomography was introduced by Munk and Wunsch in the late 1970s, and is based on the fact that travel time and other measurable acoustic parameters are functions of temperature, water velocity, and other ocean variables and can be interpreted to provide information about the intervening ocean using inverse methods (Andreeva, Wojcik, & Durgin, 2005). A broadband pulse is emitted from a spherical acoustic source to a hydrophone receiver, see Figure 1-1.

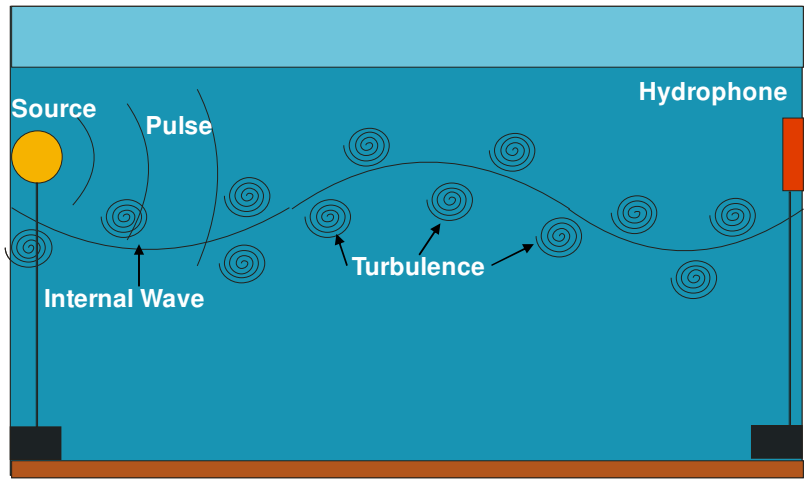

Figure 1-1: Schematic of tomographic sound wave propagation.

The travel time of the received signals determines the average sound speed. Changes in sound speed can then be related to variations in temperature, water velocity, and other parameters of oceanographic interest. The primary concern surrounding ocean acoustic tomography is the lack of precision in the travel time measurement. This inaccuracy is caused by acoustic fluctuations induced by variations within the ocean medium, induced by internal waves, turbulence, temperature gradients, density stratification or by other related phenomena that cause local perturbations in the sound speed, as well as source and receiver motion. Arrival time has been the primary characteristic from which tomographic inversions have been performed to reconstruct ocean structure. However for propagation over long ranges, ranges exceeding several hundred kilometers, it has been noted that pulse arrivals sometimes become so smeared

together due to fluctuations that they cannot be used for travel-time measurements (Simmen, Flatte, & Wang, 1997). Perturbations can interact with regular wave fronts through diffraction and refraction, causing temporal, spatial, and frequency-dependent fluctuations, severally affecting ray behavior. Ray divergence can eventually cause the ray to intersect the ocean surface or become reflected or absorbed by the ocean floor. Once a wave ray reaches the surface, it looses a significant portion of its energy and displaces the real propagation time.

Ultimately such perturbations lead to a variety of challenging problems, which include multi-path propagation, transmission loss, and the temporal or time varying nature of the channel (Gendron, 2005). These obstacles would be better understood if it was possible to predict and observe the effect each has on the acoustic signal. Accurately modeling the behavior and producing an estimation of the time of arrival for each emitted signal is crucially important for these applications. If arrival times and path behavior can be predicted the reduction of the cancellation of the multi-path effect can ultimately be performed, developing more precise signal processing techniques (A. Jarrot & A. Quinquis, 2005).

1.2.1 *Matched- field Processing*

In recent years, researchers have suggested an important improvement of the tomographic scheme. The deployment of an array of hydrophones as the measuring device instead of a single hydrophone unit makes applications to improve signal processing, such as matched-field techniques, more feasible (Taroudakis & Markaki, 1997). A broadband pulse is emitted from a spherical acoustic source (either moored or towed) and received by a vertical line array (VLA) of hydrophones, this is a typical set-up for most modern acoustic propagation experiments.

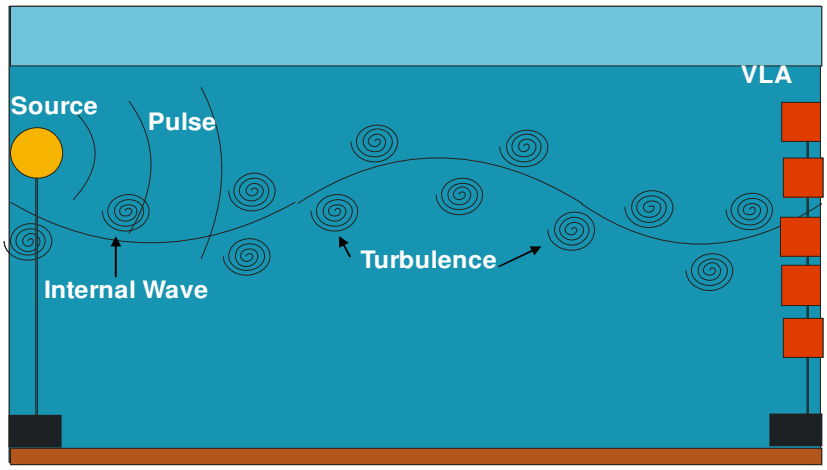

Figure 1-2: Schematic of underwater acoustic propagation experiment

A number of different approaches for processing received signals have been proposed; in general these methods utilize the information of the arrival pattern of the signal obtained in the time domain. Predictions of arrival patterns can be used for the classification of acoustic channels affected by varying turbulent environments. The travel times and arrival depths of these pulses are dependent on the encountered environmental parameters, i.e. turbulence and internal waves (Taroudakis and Markaki, 1997). Matched-field processing, involves "matching" the arrival pattern of a received signal to those of simulated candidate environments. The approach as described by Taroudakis and Markaki, (1997) utilizes a reference environment defined by a simulation. The differences of the actual arrival times with respect to those predicted for the reference environment are calculated and define a linear inverse problem. These differences have a functional relationship with the actual environmental parameters with respect to those of the reference environment. The sound-speed function $c(r,z)$ corresponding to the set of measured data can then be recovered (Taroudakis and Markaki, 1997). The temperature and depth fluctuations of the sound speed profile may indicate the presence of mesoscale eddies, mixing, and/or internal waves.

1.3 Quantification of Internal Waves and Turbulence

Characterizing the effect that fluctuations have on transmitted pulses is the goal of many researchers. However, sound pulses emitted at the sound channel axis encounter

perturbations from both internal waves and small scale turbulence. Stewart (Stewart, 1969) commenting on the study of stably stratified turbulence wrote,

> [It is greatly complicated by the fact that we have two quite different types of flows intermingled: turbulence and internal gravity waves. In addition, the inferences that we should like to draw for the unmeasured aspects of the field are totally different for the two kinds of motion. Also there is the further complication of a nonlinear coupling that causes energy to flow between them…It is clearly desirable to be able to distinguish between the effects of turbulence and waves, but it is not clear that it is possible to do so. To the first question, I would reply that it is clearly desirable to attempt to make the distinction. It is never possible to measure all the features of the particular field. One must measure some aspects and infer the rest. The inferences which would be drawn from a measurement of some aspects of a wavefield should be quite different from the inferences drawn from similar measurements in turbulence field.] (Stewart, 1969)

Since 1969, methods for quantifying turbulence have improved however there is still no exact means to discriminate between internal waves and turbulence. For instance, an internal wave packet of highly non-linear waves can grow regions of strong turbulence, this "breaking wave" is neither strictly wave nor strictly turbulence, but contains aspects of both (D'Asaro & Lien, 2000). It thereby becomes an impossible task to form a distinction between the two.

Some flows however are more turbulent or more wavelike than others (D'Asaro & Lien, 2000). In general, internal waves are the dominant cause for temporal fluctuation during long range propagation (Tang and Tappert 1997). For short range propagation, these internal waves may break causing small scale turbulence and the dominance of one feature over the other is unknown (D'Asaro & Lien, 2000). Internal waves are assumed to dissipate and drive turbulence, this combination has been found to have a substantial effect on arrival time fluctuations during short range propagation (Henyey *et al*., 1997).

1.4 Review of Chaotic and Stochastic Internal Wave Models

The behavior of the pulse during its transmission is also a complex issue. Recent theoretical and experimental studies by Simmon et al. (1999), have suggested that the breakdown in identifying isolated and resolved signal arrivals at long ranges is due to ray chaos induced by a range-dependent ocean structure. This chaotic behavior has been investigated in numerous works ((Smith, Brown, & Tappert, 1992); (Duda & Bowlin, 1994); (Colosi, Flatte, & Bracher, 1994); (Zaslavsky & Abullaev, 1997); (Simmen & Flatte, 1999); (Wiercigroch, Badiey, Simmen, & Cheng, 1999)). In his recent work, Wiercigroch *et al.* (1999), studied the non-linear dynamic behavior of basic ray equations in the presence of a wave-like forcing assuming a single-mode sound speed perturbation is superimposed onto a generic range independent sound speed profile, Munk's canonical sound speed profile (Munk, 1974). This model vastly simplifies nature by only accounting for the chaotic behavior caused by internal waves, and ignoring the randomness of the process. Other researchers suggest that the motion of sound trajectories in deep ocean environments exhibits stochastic behavior, which can be attributed to internal waves (Brown & Viechnicki, 1998). In their recent work, Colosi and Brown (1998) developed a method to construct statistically realistic random realizations of internal wave induced sound speed perturbation fields, despite its simplicity and efficiency, the method has certain limitations. It is the intension of this work to demonstrate that the consideration of both chaotic behavior and stochastic influences produce more realistic predictions for underwater wave propagation.

1.5 Objectives and Approach

The primary objective of this research is to develop a predictive methodology for received signal variation as a function of ocean perturbations that occur during short and long range propagation. The motivations for the work presented in this thesis are the limitations of underwater acoustic propagation. The classification of ocean environments will provide information that will be useful in enhancing the processing techniques for transmitted signals. The approach here is twofold. The first is to consider internal waves only, since it is typical that these perturbations dominate turbulent effects at the sound channel axis during long range propagation (Colosi, Flatte, & Bracher, 1994). Our theoretical development will consider both the chaotic and stochastic effects of internal

waves; this dual contribution has not been considered in prior acoustic propagation models. The eikonal equation is considered in the form of a second order, nonlinear ordinary differential equation with internal waves. The internal waves are considered to have random phase or amplitude modulation in the form of zero-mean Gaussian white noise. Bifurcation analysis can illustrate that consideration of only chaotic behavior somewhat simplifies the real problem, where the stochastic behavior may have a substantial input, thereby providing a more realistic characterization of acoustic arrivals.

The second portion of this work is to expand the model to consider other perturbations affecting ray behavior during ocean sound transmission typical to short range propagation. The improved computational ray tracing model simulates three typical turbulent states that can occur in the ocean's main thermocline along the sound channel axis. These scenarios include:

- ◊ Sound passage through simulated turbulence
- ◊ Sound passage through internal gravity waves
- ◊ Sound passage through a field containing both internal gravity waves and simulated turbulence combined

Each vortex in the eddy field is treated as a line vortex based on potential theory assumptions. For each perturbation scenario the developed acoustical propagation model:

- ◊ Illustrates the multi-path structure induced by the sound speed profile through presentation of ray tracing diagrams for varying initial conditions.
- ◊ Estimates signal delay and arrival behavior induced by the turbulent medium by predicting arrival times, arrival depth, and velocity fluctuations for a geophysical time series.
- ◊ Presents energy-frequency spectra of the fluctuating mean travel velocity based on predicted arrival times.

These simulations provide the necessary information for the classification of perturbation scenarios in a multi-path underwater environment. This analysis is useful in predicting impulse response as well as for providing the necessary data for improvement of filtering and smoothing techniques. It is the intention of this research to provide the

groundwork for enhancing transmission capabilities as well as to provide some analysis of typical ocean turbulent flows and its impact on high-frequency propagation.

This thesis is organized as follows. In Chapter 2, the ocean acoustic environment is discussed to demonstrate the complexity of the ocean medium. Chapter 3 details the development of the theory behind our acoustic propagation model including those equations derived to represent internal wave perturbations as well as those used to model the eddy field. Chapter 4 reviews the statistical representation of turbulence as a precursor for the proceeding analysis chapters. Chapter 5 outlines the developed algorithms for the simulations. Chapter 6 is devoted to the statistical analysis of the numerical results, as well as chaos analysis to support the internal wave theory. Finally, Chapter 7 provides a summary of the work and formulated conclusions, ending with future work and recommendations.

2 ENVIORNMENTAL BACKGROUND

This chapter presents an overview of the complexity of the ocean acoustic environment, which is necessary for understanding the theoretical approach of the computational model.

2.1 Sound Velocity in Water

The sound speed in the ocean is an increasing function of temperature, salinity, pressure, and depth. The following is an empirical function for sound velocity, c, in terms of three independent variables: temperature - $T\ (^{\circ}C)$, salinity - $S\ (parts/1000)$, depth - $z\ (m)$, (Brekhovskikh, 1982).

$$c = 1449.2 + 4.6T - 0.055T^2 + 0.00029T^3 + (1.34 - 0.01T)(S - 35) + 0.016z \qquad \textbf{(2-1)}$$

Oceanographers perform CTD (Conductivity, Temperature, and Depth) scans of the ocean to determine the sound speed over a region. Figure 2-1 shows a plot of three sound speed profiles calculated using CTD data obtained from the National Oceanographic and Atmospheric Administration, Table 2-1 lists the date and location of each cast.

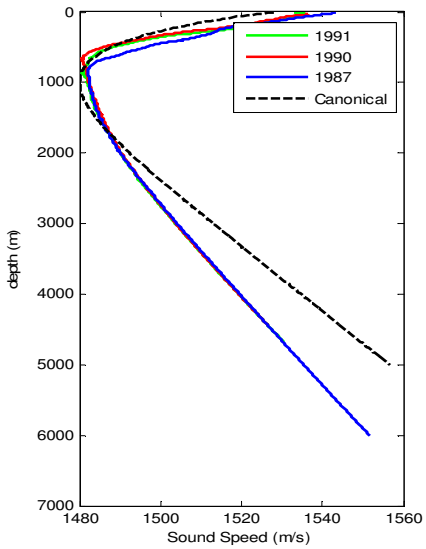

Figure 2-1: Sound Speed Profiles based on Pacific Ocean CTD scans (NOAA/EPIC, 2005).

Table 2-1: Date and location of CTD casts used for Figure 2-1 (NOAA/EPIC, 2005).

Date of CTD cast	Longitude	Latitude
04 August 1987	$24^{\circ}0.5^{'}N$	$165^{\circ}0.3^{'}E$
24 July 1990	$22^{\circ}47.1^{'}N$	$158^{\circ}0.6^{'}W$
09 July 1991	$22^{\circ}45.0^{'}N$	$158^{\circ}0^{'}W$

The ocean is considered a horizontally stratified medium, having several layers; the upper most are depicted in Figure 2-2, which indicates the regions of variability based on the sound speed profile. Sound speed increases linearly toward the ocean floor and increases exponentially toward the ocean surface. The coordinate system is two-dimensional, referencing the (r,z)plane, where *r* is range and *z* is depth. The properties of the water nearest to the surface result from mixing due to surface winds and wave activity at the ocean-air interface. This layer holds for varying temperature, except during severe environmental conditions. The next layer is the thermocline. The warming of the sea surface by the sun creates a temperature gradient, the temperature decreases with depth and thereby so does the sound speed. Below the thermocline lies the deep isothermal layer, in this layer, there is less fluctuation in temperature, and the pressure becomes greater, leading to an increase in sound speed. Between the mixed layer and the deep isothermal region, there is a sound speed minimum at a certain depth, which varies for different geographic regions. This depth is referred to as the underwater sound channel axis. For example, in the Polar Regions the water is coldest near the surface and hence the sound speed minimum is at the ocean-air or ocean-ice interface. A typical depth of the axis in other regions of the world, is 1000-1500m, in the tropical zone it falls to 2000m, but rises closer to the surface at higher latitudes.

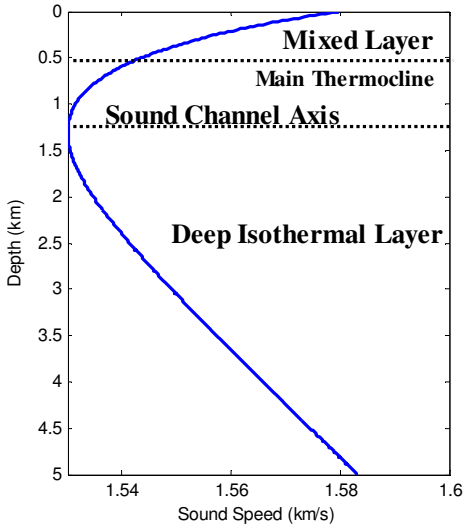

Figure 2-2: Sound Speed profile with regions of instability.

The sound channel is one particular case of a natural waveguide for the sound waves transmitted along it, analogous to the acoustic waveguide in the atmosphere. Sound waves tend to bend toward regions of lower sound speeds, illustrated in Figure 2-3, where $z = z_a$ shows the boundaries of the sound channel and $c = c_{ch}$ is the sound speed at the sound channel axis.

Interest lies in modeling sound behavior generated by a source and received by a hydrophone. Pulses emitted at small or moderate angles (with respect to the horizontal) from a spherical sound source placed on or near the sound channel axis will be redirected to the sound channel axis repeatedly, and their energy will remain trapped in the sound channel. These pulses propagate without reaching the bottom or surface, and do not undergo scattering or substantive absorption. This is the ideal case for the prior mentioned applications.

2.1.1 *Canonical Sound Speed Profile*

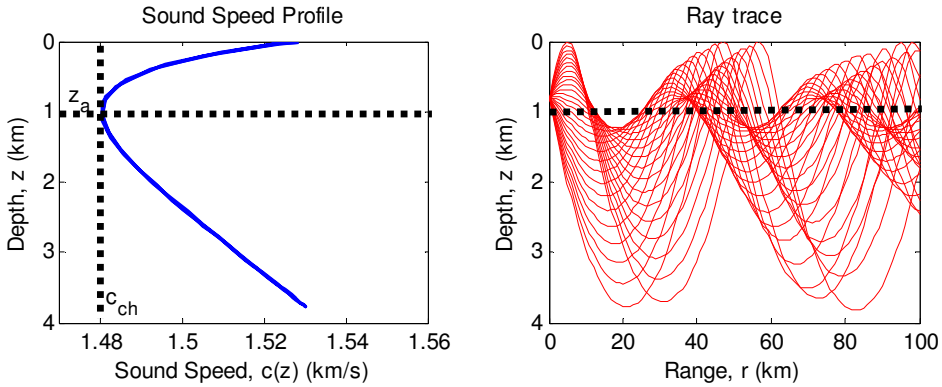

Figure 2-3: Munk Sound Speed Profile and resulting Ray Path behavior

Ray paths typical to a ray traveling through an ocean with a canonical sound speed profile are depicted in the ray trace diagram seen in Figure 2-3, launch angles range from $-15^{\circ} \le \phi(0) \le 15^{\circ}$. This canonical sound speed profile was developed by Munk in 1974 to represent an idealized sound channel (Munk, 1974). He based his derivation on the stability of the water column beneath the thermocline, the Brunt-Väisälä or buoyancy frequency of the stratification,

$$N = \sqrt{\frac{g}{\rho}\frac{\partial p}{\partial z}} \tag{2-2}$$

where $\partial p/\partial z$ is the vertical potential density (Munk, 1974). His canonical profile is represented below.

$$\begin{aligned} c(z) &= c_{ch}\left(1 + \varepsilon_{ssp}\left(\eta_{ssp} + e^{-\eta_{ssp}} - 1\right)\right), \\ \eta_{ssp} &= \frac{2}{B}\left(z - z_a\right) \end{aligned} \tag{2-3}$$

Here z_a is the depth (km) of the sound channel axis and c_{ch} is the sound speed (km/s) at the sound channel axis. The parameter ε_{ssp} is the perturbation coefficient (dimensionless) defined to be:

$$\varepsilon_{ssp} = \frac{1}{2} B \gamma_a \tag{2-4}$$

where B is the stratification scale depth (km) and $\gamma_a = 0.0114 km^{-1}$, is the calculated adiabatic velocity gradient. The parameters in this equation are based on the temperature, salinity, pressure coefficients of *c(z),* and the salinity coefficients of $\partial p/\partial z$. This is sound speed profile representation for the simulations of this work.

2.1.2 *SLICE89: Long Range Propagation Experiment*

In order to establish a more realistic ocean model, observed sound speed parameters from the SLICE89 experiment, an acoustic propagation experiment conducted in the Pacific Ocean in 1989, were used in the canonical sound speed profile described above. The background of the experiment is briefly described to illustrate its relevance to this thesis. The review of the SLICE89 experiment is taken from "Measured wave-front fluctuations in 1000-km pulse propagation in the Pacific Ocean," (Duda *et al.* 1992). The SLICE89 long range propagation experiment was a collaboration of the Institute of Marine Sciences at the University of California, Scripps Institution of Oceanography at the University of California, and the Applied Physics Laboratory at the University of Washington.

The SLICE89 experiment was a 1000km acoustical transmission experiment conducted in the North Pacific during July of 1989. Pulses were sent between a moored broadband source with a 250Hz center frequency and a moored sparse vertical line array (VLA) of receivers. The source was moored at a depth of 804m near the $32^{\circ}0^{'}N, 150^{\circ}26^{'}W$. East-northeast of the source a VLA was suspended from a research platform called FLIP, which was moored near the $34^{\circ}0^{'}N, 140^{\circ}0^{'}W$. The source was placed near the depth of the sound channel axis. A CTD cast near the transmission path showed the axis to vary from 700m-800m depth. The receiving array, 3km in length, was suspended near the surface from the moored platform with a weight at the end. The VLA had a separation distance of 60m between each hydrophone. The SLICE89 provided fluctuation observations with high resolution in both depth and time for duration of a few days with sampling at multiple depths. The parameters listed in Table 2-2 serve as the sound speed parameters for this simulation.

Table 2-2: Initial Conditions and Parameters from SLICE89 experiment.

B	1.3km
ε_{ssp}	0.0074
z_a	0.75km
c_{ch}	1.49km/s
$z(0)$	0.804km
$\phi(0)$	$-10^\circ \le \phi(0) \le 10^\circ$

2.2 Variability of the Ocean

The ocean is extremely variable containing such fluctuations as currents, internal waves, mesoscale eddies, and other small-scale turbulence that perturb the nature of sound velocity and cause spatial and temporal fluctuations of the propagating sound path. Such disturbances can lead to the destruction of coherence along the ray path. These features are typical of the sound channel axis and are further discussed in the subsequent subsections. Mathematical descriptions of the structures are formulated in Chapter 4.

2.2.1 *Mesoscale Eddies*

Wind-driven surface currents are prominent throughout the earth's oceans. As these currents flow along the coastline or in the middle of the ocean, they can encounter resistance from landmasses or water with varying CTD properties. This causes the current to wind or bend and form two-dimensional rotating structures with either a vertical or horizontal axes of rotation, which extract kinetic and potential energy from the mean flow (Chamberlin, 2005). These formations are known as large scale eddies. Those with a horizontal axis are known as mesoscale eddies and those with a vertical axis of rotation are geostrophic eddies. These large ocean eddies are analogous to atmospheric weather systems, such as hurricanes; as they form they acquire a certain rotational velocity, net direction, and characteristic temperature structure.

Eddies range in diameter from one to several hundred kilometers and can be several meters deep, depending on their size; they may retain their properties for months.

A recent study of mesoscale eddies in the Bering Sea, done by the NOAA, found typical geostrophic eddy diameters to range from 25 to 100 km, depth to range from 2 to 5km, and to propagate at a few cm/s, with rotational speeds of 80 cm/s (NOAA, 1997).

There are two types of eddies that can evolve: warm core eddies and cold core eddies. Figure 2-4 is a satellite sea-surface temperature image of geostrophic eddies in the Gulf Stream. The blue and green colors indicate cold water and the red and orange represents warm water. This image shows both warm core and cold core eddies.

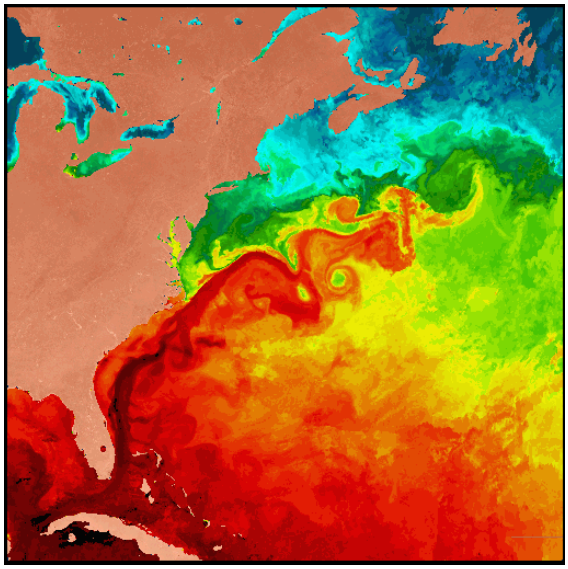

Figure 2-4: Satellite Image of Geostrophic Eddies off the Gulf Coast (Chamberlin, 2005).

2.2.2 *Small Scale Turbulence*

The wind blowing over the ocean surface generates surface waves which form small scale turbulence and currents below the ocean surface. In coastal environments, the mixing of water properties often occurs due to strong tidal currents caused by these surface waves. This turbulent mixing is typically found in relatively shallow and narrow channels formed by coastal islands, which can cause scattering and other such degeneration in signal transmission. Di Iorio and Farmer (1997) observed the dominance of turbulent fluctuations during their short range shallow acoustic propagation experiments. At small scales, less than about several meters, the variability can be assumed to be caused by isotropic, locally homogeneous turbulence (Henyey *et al.*, 1997). Di Iorio and Farmer used this approach during simulations and found agreement

with acoustic observations seen in the conducted experiments (Di Iorio & Farmer, 1997). Small scale turbulence is also be produced by breaking internal waves. For short range propagation it becomes necessary to consider the combination of these effects (Henyey *et al.*, 1997).

2.2.3 *Internal Waves*

The stratified layers of the ocean (Figure 2-2) vary in density. The main thermocline and the deep isothermal layer have a very large density contrast and the interface between these layers is subject to wave motion, occurring when gravitational forces act on changes in the mean density of the medium and displace water. This oscillating motion does not affect the surface and is described as an internal wave. The buoyancy force is the restoring force required to return particles to their average position and is proportional to the product of gravity and the density difference between the two layers.

$$F_B = -g\left(\rho_{layer1} - \rho_{layer2}\right) = -g\Delta\rho \qquad \textbf{(2-5)}$$

If the buoyancy force is positive, $F_B > 0$, if $\Delta\rho$ is negative an upward force results. In general, the frequency of a wave increases with the strengthening of the buoyancy force. The density difference between layers is much smaller than the density difference between air and water (by several orders of magnitude); therefore internal waves have larger amplitudes than surface waves and have wavelengths several kilometers long (Wadzuk & Hodges, 2004). Internal waves have periods of 10-20 minutes to several hours much longer than surface waves, which have periods of a few seconds to minutes (Brekhovskikh, 1982).

The Brunt-Väisälä or buoyancy frequency, *N*, provides a measure for the strength of the ocean's stratification. More strongly stratified fluids have higher frequency oscillations, because the restoring force for vertical displacements is larger, the Brunt-Väisälä frequency equation is described in Equation 2-2, but is repeated here (Munk, 1974):

$$N = \sqrt{\frac{g}{\rho}\frac{\partial\rho}{\partial z}} \qquad \textbf{(2-6)}$$

Where ρ is the density of the ocean layer, g is the acceleration due to gravity, and z is vertical displacement. The frequency squared, N^2 gives a measure of stability; N is real and has the dimensions of frequency. This is the frequency at which internal waves will oscillate and is typically a few cycles per hour (10^{-3} Hz) in the main thermocline (Gill, 1982).

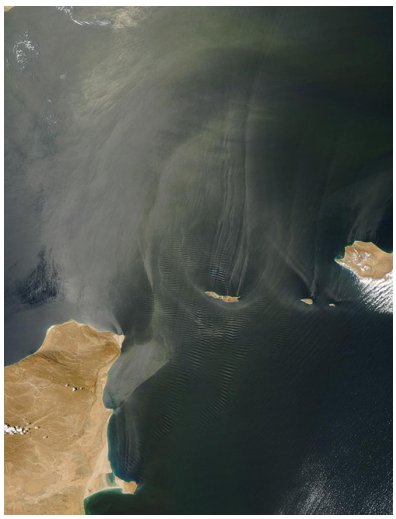

Figure 2-5: Satellite view of internal waves off Somalia (NASA, 2005).

Figure 2-5 is a satellite photo taken of internal waves propagating off the coast of Somalia. Convergence of surface particle movement above the wave troughs near the surface often collects floating matter and makes the waves visible as slick marks (Tomczak, 1996).

3 WAVE PROPAGATION THEORY

This chapter presents a derivation of the equations used to describe the behavior of the propagation of waves in inhomogeneous moving media. Development of the acoustic propagation model with addition of internal waves represented by an imperfectly harmonic forcing function was done following Andreeva (2004).

3.1 The Acoustic Propagation Model

This research considers fixed frequency wave fields, which satisfy a depth dependant Helmholtz equation.

$$\nabla^2\psi + \frac{\omega}{(c(z))^2}\psi = 0 \qquad \textbf{(3-1)}$$

Here $\omega = 2\pi f$ is the angular frequency of the acoustic source and $c(z)$ is the depth dependant sound speed profile of the ocean derived by W. Munk (1974) and previously discussed in Section 2.1.1,

$$\begin{aligned} c(z) &= c_{ch}\left[1 + \varepsilon_{ssp}\left(\eta_{ss} + e^{-\eta_{ssp}} - 1\right)\right], \\ \eta_{ssp} &= \frac{2}{B}(z - z_a) \end{aligned} \qquad \textbf{(3-2)}$$

The short wave approximation can be applied when the properties of the medium vary more slowly on a scale compared to the acoustic wavelength, λ where $\lambda = 2\pi/k$ and k is the wavenumber taken as $k = 2\pi f/c(z)$.

$$\omega >> \nabla c(z) \qquad \textbf{(3-3)}$$

This leads the solution to the Helmholtz equation to be represented as a ray series or the sum of local plane waves.

$$\psi(z) = \sum_j A_j(z) e^{i\omega T_j(z)} \qquad \textbf{(3-4)}$$

where $A(z)$ is the amplitude of the plane wave, and *T(z)* is the classical action variable, an unknown function of depth. Substitution of Equation 3.4 into the Helmholtz equation, (Equation 3.1), and collecting terms in descending powers of ω, yields the eikonal and transport equations, respectively.

$$\left(\nabla^2 T\right) = \frac{1}{c^2(z)}$$
$$\nabla\left(A^2 \nabla T\right) = 0 \qquad \textbf{(3-5)}$$

The solution of the eikonal equation describes the behavior of ray trajectories and the travel time along them. The transport equation, characterizes the signal along each ray, which is beyond the scope of this research, thereby only the solution to the eikonal equation is considered.

For guided wave propagation in the direction of increasing *r*, the variable *r* can operate as the "time-step" variable, and the solution to the eikonal equation can be reduced to have a Hamiltonian form, known as the one-way ray equations:

$$\frac{dz}{dr} = \frac{\partial H}{\partial p},$$
$$\frac{dp}{dr} = -\frac{\partial H}{dz}, \qquad \textbf{(3-6)}$$
$$\frac{dT}{dr} = p\frac{dz}{dr} - H$$

H is the Hamiltonian represented as:

$$H(z,p) = -\sqrt{\frac{1}{c^2(z)} - p^2} \qquad \textbf{(3-7)}$$

p, (kg-m/s) is the momentum vector, $p = \tan\phi$, ϕ is the ray angle measured with respect to the horizontal. Figure 3-1 illustrates a schematic of these variables. The classic action variable, *T* is related directly through the travel time, τ of the acoustic ray by,

$$T = c_0\tau - r \qquad \textbf{(3-8)}$$

Solving for τ and taking its derivative with respect to *r*, we obtain:

$$\frac{d\tau}{dr} = \frac{1}{c_0}\left[\frac{dT}{dr} + 1\right] \qquad \textbf{(3-9)}$$

Substituting dT/dr into Equation 3.9 produces a differential equation for the travel time, τ of the acoustic ray.

$$\frac{d\tau}{dr} = \frac{1}{c_0}\left[p\frac{dz}{dr} - H + 1\right] \qquad \textbf{(3-10)}$$

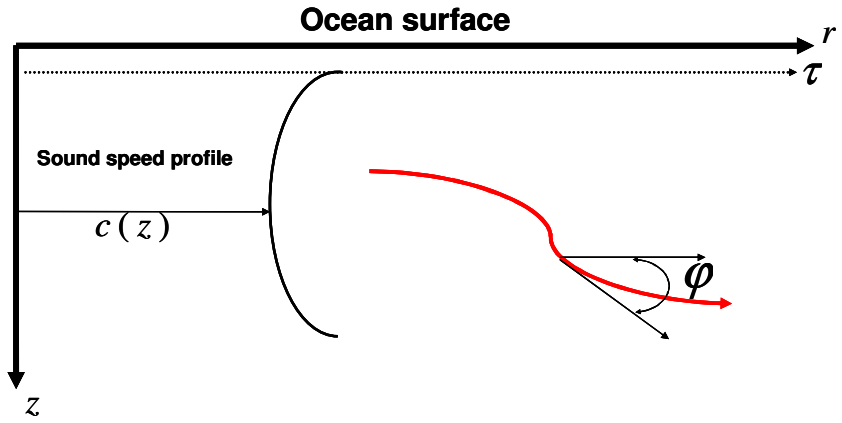

Figure 3-1: Schematic of propagating ray

3.1.1 *The Parabolic Equation Approximation*

It is often useful to use assumptions about the moving medium in question in order to simplify methods. As discussed in Chapter 1, a practical application of this research is ocean acoustic tomography, which utilizes the propagation of high-frequency ultrasonic waves to study the properties of the ocean. Therefore it is sensible to use the parabolic condition to neglect the backscattered portion of the wave in the Helmholtz equation (Jenson *et al*. 1994). The parabolic approximation is valid when ray angles are small and deviations of *c(z)* from c_0 are small, where c_0 is the reference sound speed, which is true in this case. The solution to the Helmholtz equation can be expressed as:

$$\psi(z) \approx \Psi(z) e^{ik_0 z}, k_0 = \omega / c_0 \qquad \textbf{(3-11)}$$

Substitution of Equation 3.11 into the Helmholtz equation, (Equation 3.1) gives the standard parabolic wave equation,

$$-\frac{i}{k_0}\frac{\partial \Psi}{\partial r} = \left(\frac{1}{2k_0}\frac{\partial^2}{\partial z^2} - c_0 V(r) \right) \Psi \qquad \textbf{(3-12)}$$

where *V(z)* is the potential energy.

$$V(z) = \frac{1}{2}\left(1 - \left(\frac{c_0}{c(z)} \right)^2 \right) \qquad \textbf{(3-13)}$$

Again, *c(z)* is the average sound speed profile calculated after W. Munk. The Hamiltonian with parabolic approximation is represented as:

$$H_{PE}(z,p)=\frac{1}{2}p^2+V(z) \tag{3-14}$$

3.2 Internal Wave Model

Internal waves are usually considered an external source of perturbations, which interfere with acoustic wave long-range propagation causing, among other phenomena, ray chaos. Considerable effort has been expended in investigating chaotic properties of the travel time of sound pulses passing through individual rays ((Smith, Brown, & Tappert, 1992); (Duda & Bowlin, 1994); (Colosi, Flatte, & Bracher, 1994); (Zaslavsky & Abullaev, 1997); (Simmen & Flatte, 1999); (Wiercigroch, Badiey, Simmen, & Cheng, 1999)).

In the works listed above, researchers have not accounted for the possible nondeterministic contribution from the internal waves, due to the unknown variations of such parameters as buoyancy. In the following derivation an imperfect forcing function will be used to account for both the chaotic and stochastic effects that internal waves present. The theory uses fairly simple techniques to construct a more realistic description of the ocean with little to no limitations. So far, the propagated rays have been modeled as an energy conserving system, which in reality is subjected to perturbations from the internal waves in the mesoscale of the ocean, (Weircigroch *et al.*, 1999). These perturbations are described by adding a range and depth dependant forcing function to the Hamiltonian with the parabolic approximation.

$$H(z,p)=\frac{1}{2}p^2+V(z)+F(z,r), \tag{3-15}$$

$F(z,r)$ are external perturbations represented by a single-mode wave:

$$F(z,r)=\sqrt{2}Ae^{-3z/2B}\sin\left(\frac{2\pi r}{R}\right) \tag{3-16}$$

The range-dependent perturbation (internal wave) has magnitude A and wavelength R *(km)*. Such a system has been studied extensively in Wiercigroch *et al.*, (1999). It is reasonable to assume that the perturbation due to the internal waves is not perfectly harmonic, but rather imperfectly harmonic. To model the fluctuations of the internal waves an imperfectly harmonic wave, a harmonic function with randomly perturbed phase and/or amplitude is used. The amplitude and the phase of the internal wave are

randomly perturbed with additive Gaussian white noise (GWN). The GWN can simply be added to the amplitude; however the phase of the internal wave must be represented using the stochastic differential equation with additive noise.

$$F(z,r) = \sqrt{2}(A+\zeta)e^{-3z/2B}\sin(q(r))$$
$$\frac{dq}{dr} = \frac{2\pi}{R} + \xi \qquad \textbf{(3-17)}$$

ξ and ς are Gaussian white noises with zero mean and delta correlation, Equation 3.18. Noise intensities are D_1 and D_2 and angular brackets denote averaging (only D_1 or D_2 are assumed non-zero during the calculations).

$$<\xi(r)>=0, <\xi(r)\xi(r+\tau)>=D_1\delta(\tau),$$
$$<\varsigma(r)>=0, <\varsigma(r)\varsigma(r+\tau)>=D_2\delta(\tau) \qquad \textbf{(3-18)}$$

This governing system of equations is obtained by substituting the new Hamiltonian with imperfect forcing function into Equation 3.6, to produce a system of nonlinear differential equations with internal waves (both deterministic and nondeterministic contributions), formally described as:

$$\frac{dz}{dr} = p,$$
$$\frac{dp}{dr} = -\frac{2}{B}c_0^2 c_{ch}\varepsilon\frac{1-e^{-2(z-z_a)/B}}{c(z)^3} + \frac{\sqrt{3}}{2B}e^{-3z/2B}(A+\zeta)\sin q(r),$$
$$\frac{dq}{dr} = \frac{2\pi}{R} + \xi \qquad \textbf{(3-19)}$$
$$\frac{d\tau}{dr} = \frac{1}{2c_0}\left[1+p^2+\left(\frac{c_0}{c(z)}\right)^2\right] + \frac{1}{c_0}\left[\sqrt{2}e^{-3z/2B}(A+\zeta)\sin q(r)\right]$$

3.3 Eddy Representation

The potential theory assumption is based on the fact that for most fluids the viscosity is small, resulting in large Reynolds numbers so that viscous effects are only important close to the boundaries. The viscosity of the ocean is $\nu_{ocean} \approx 10^{-6}\, m^2/s$, lengths are large and velocities significant, so for many process the potential assumption is reasonable. Potential flow theory however, is not applicable on all scales of the flow. At small length scales, or the Kolmogorov scale, viscous effects are important and cannot be neglected. The Kolmogorov scale is discussed at length in Chapter 4. For brevity here,

the Kolmogorov scale is the length scale at which turbulence dissipates. The Kolmogorov scale is proportional to viscosity, and viscous dissipation. The Kolmogorov scale holds for small Reynolds numbers $\left(\mathrm{Re} \approx O(10^0)\right)$, whereas the energy containing and inertial length scales the Re is much larger $\left(\mathrm{Re} \approx O(10^8)\right)$. Viscous effects remain confined to the Kolmogorov scale and the bulk flow is unaffected by them. It is thereby reasonable to apply the potential theory in high Re flow situations.

Each eddy in the field is treated as an ideal line or free vortex. Free vortex motion is irrotational and its flow field is generally described by its stream function and velocity potential, respectively.

$$\psi_{vortex} = -\frac{\Gamma}{2\pi}\ln\left(\sqrt{r^2+z^2}\right) \quad \textbf{(3-20)}$$

$$\phi_{vortex} = \frac{\Gamma}{2\pi}\tan^{-1}\left(\frac{z}{r}\right) \quad \textbf{(3-21)}$$

These equations can be represented in polar coordinates, where $r_{vortex} = \sqrt{r^2+z^2}$ and $\theta_{vortex} = \tan^{-1}(z/r)$.

$$\psi_{vortex} = -\frac{\Gamma}{2\pi}\ln r_{vortex} \quad \textbf{(3-22)}$$

$$\phi_{vortex} = \frac{\Gamma}{2\pi}\theta_{vortex} \quad \textbf{(3-23)}$$

The total circulation at which particles rotate around the origin of the vortex is Γ (Alexandrou, 2001). The vorticity of the field, $\omega_{vortex} = \nabla \times V$, where V is the resultant velocity, is equal to 0 everywhere in the flow except the origin (Alexandrou, 2001). There is a singularity that occurs at the core, $r_{vortex} = 0$, where the flow is rotational and thereby has non-zero vorticity, here viscous effects are important. The core is treated as a solid body and contains distributed vorticity equal to that of the line vortex velocity. The velocity field induced by the vortex is directly related to circulation. The tangential velocity varies inversely with the distance from the origin; this is depicted in Figure 3-2, where the concentric circles represent lines of the increasing stream function (Alexandrou, 2001).

$$v_{r_{vortex}} = 0 \tag{3-24}$$

$$v_{\theta_{vortex}} = \frac{\Gamma}{2\pi r_{vortex}} \tag{3-25}$$

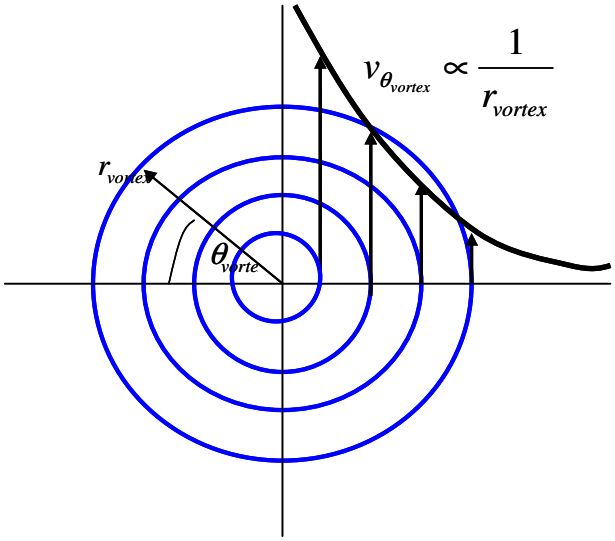

Figure 3-2: Schematic of Line Vortex.

4 STATISTICAL DESCRIPTION OF TURBULENT FLOW

The turbulent flows simulated in this work are described through a statistical representation of the fluctuating velocity. Each perturbation that causes the mean traveling velocity (MTV) of the pulse, to fluctuate is characterized by a length scale. The energy produced by each scale is represented by a velocity spectrum. This chapter serves as a prerequisite for the analysis that is used to characterize our simulated turbulence environments. The materials in the subsections that follow are discussed only in brief; please refer to the original sources for further detail ((Tennekes & Lumley, 1972); (Pope, 2001); (Hinze, 1959); (Tatarskii, 1961); (White, 1976/2004)).

4.1 Stationary Random Functions and Moments

A typical feature of a turbulent flow, is that the fluid velocity fluctuates significantly and irregularly over space and time (Pope, 2001). Figure 4-1 illustrates fluid velocity fluctuations over time in a turbulent ocean.

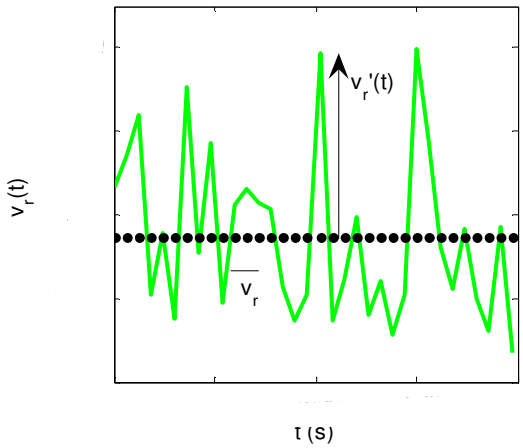

Figure 4-1: Turbulent velocity fluctuations.

The fluid velocity is a random variable in time, which can be decomposed into the time average of $\bar{v}_r$, and some fluctuation, v_r'.

$$v_r(t) = \bar{v}_r + v_r' \tag{4-1}$$

The time average of $v_r(t)$ is defined as

$$\bar{v}_r = \frac{1}{T}\int_{t_o}^{t_0+T} v_r(t)dt \qquad \textbf{(4-2)}$$

The integration interval T is chosen to be larger than any significant period of the fluctuations, v_r'.

The fluctuations may be further depicted by other statistical characteristics of the random field, referred to as moments. The first moment is the mean, the time average of the turbulent velocity, Equation 4.2. The second moment is the variance, defined to be the mean-square of the fluctuation or the mean square departure from the mean,

$$\sigma^2 = \bar{v}_r'^2 = \frac{1}{T}\int_{t_0}^{t_0+T} v_r'^2\, dt \qquad \textbf{(4-3)}$$

The square-root of the variance is the standard deviation or r.m.s. (root mean square) of $v_r(t)$.

$$\sqrt{\sigma^2} = \left\langle \bar{v}_r'^2 \right\rangle^{1/2} \qquad \textbf{(4-4)}$$

The most important characteristic of a random function, for the purposes here in, is its autocorrelation function (Tatarskii, 1961). The autocorrelation function is the normalized form of the autocovariance.

$$R(\tau) \equiv \left\langle v_r'(t) v_r'(t+\tau) \right\rangle \qquad \textbf{(4-5)}$$

The autocorrelation function,

$$R_N(\tau) \equiv \frac{\left\langle v_r'(t) v_r'(t+\tau) \right\rangle}{\left\langle v_r'(t)^2 \right\rangle} \qquad \textbf{(4-6)}$$

has the following properties,

$$R_N(0) = 1 \qquad \textbf{(4-7)}$$

$$\left| R_N(\tau) \right| \le 1 \qquad \textbf{(4-8)}$$

A random process is statistically stationary if all statistics are invariant under a shift in time. For stationary random functions there exists a Fourier expansion. The Fourier transform of the autocovariance is twice the frequency spectrum of the fluctuation; hence they form a Fourier-transform pair.

$$E(f) = \frac{1}{\pi}\int_{-\infty}^{\infty} R(\tau)e^{-i2\Pi f\tau}d\tau = \frac{2}{\pi}\int_{0}^{\infty} R(\tau)\cos(2\pi f\tau)d\tau \quad \textbf{(4-9)}$$

$$R(\tau) = \frac{1}{2}\int_{-\infty}^{\infty} E(f)e^{-i2\pi f\tau}df = \int_{0}^{\infty} E(f)\cos(2\pi f\tau)df \quad \textbf{(4-10)}$$

It is clear that $R(\tau)$ and $E(f)$ contain the same information, just in different forms, $R(\tau)$ is real and even and therefore so is the frequency spectrum. The velocity fluctuation v_r' has a spectral representation of the weighted sum of Fourier modes of different frequencies f.

$$e^{i2\pi ft} = \cos(2\pi ft) + i\sin(2\pi ft) \quad \textbf{(4-11)}$$

The fundamental properties of the frequency spectrum is that for $f_a < f_b$ the integral,

$$\int_{\omega_a}^{\omega_b} E(f)df \quad \textbf{(4-12)}$$

is the contribution to the variance of all modes in the frequency range $f_a \le f < f_b$. These statistical representations are applied to all simulated turbulent scenarios because they are stationary random functions.

4.2 Length Scales

Turbulence spectral models depict the amount energy present on the basis of a turbulent length scale. This subsection provides a description of those length scales needed for understanding the pertinent spectra.

Length scales are used to describe the scale of turbulence, that is, the size of the eddy relative to other perturbations in the flow. The non-dimensional parameter, Reynolds number, $\mathrm{Re}_{flow} = U_{flow}L_{flow}/\nu$, describes the behavior of a flow, specifically whether laminar or turbulent. A flow with $\mathrm{Re}_{flow} > 4000$ and characteristic velocity U_{flow}, length scale L_{flow}, and fluid viscosity υ will be turbulent. In 1941, A. Kolmogorov proposed that for large Reynolds number Re_{flow}, turbulent flow, the statistical properties of this turbulence for the largest scale L depend only on the rate at which energy is produced and are independent of viscosity, and energy is cascaded down

to smaller eddies and ultimately dissipated by viscosity (White, 1974/2006). The largest scale eddies have a characteristic eddy velocity V, dimensional analysis implies the dissipation to be proportional to

$$\varepsilon \propto \frac{V^3}{L} \tag{4-13}$$

Therefore the dissipation timescale will be the eddy turnover timescale $T = L/V$, typically $O(1000s)$ (Gill 1982). This suggests that if the large scale energy source is terminated, turbulence will decay within a few turnover times. Table 4-1 illustrates ranges for the horizontal scales of oceanic process, the wavelengths of waves and the horizontal diameters of eddies, (Gill, 1982).

Table 4-1: Scales of Oceanic Processes (Gill, 1982).

Process	Velocity (m/s)	Horizontal Scale (m)
Sound Wave (300Hz)	1500	$\lambda = 5$
Oceanic Turbulence	0.001 – 1	0.001 – 100
Internal Waves	1 – 3	R = 1000 – 40 000
Mesoscale Eddies	0.01 – 1	1000 – 100 000
Surface Gravity Waves	1 - 20	1 - 100

The energy cascade shown in Figure 4-2 describes how energy is transferred to successively smaller and smaller eddies. Turbulent kinetic energy is extracted from the mean flow at the largest scales; this is referred to as the energy containing range. The smallest scales are determined by the viscosity of the flow υ, and the rate at which energy is supplied by the largest scale eddy. This is the dissipation range. There is an intermediate range, know as the inertial subrange. Here the turbulent energy is neither produced nor dissipated but merely transferred from the larger scales to the smaller scales.

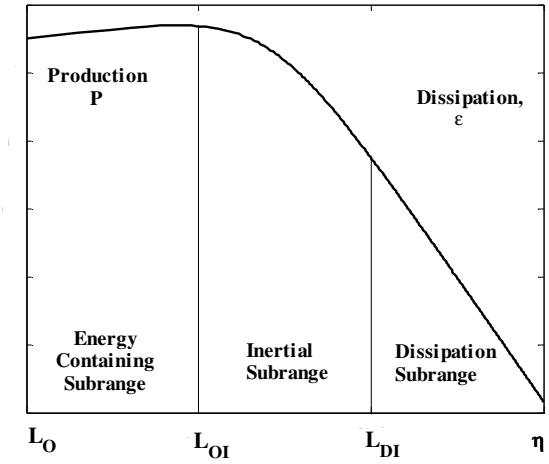

Figure 4-2: Energy Cascade versus Length Scale

4.2.1 *Determination of length scales*

There are standard turbulence length scales for each of the eddy sizes. The length scale in this thesis will refer to the radial component of each eddy. The length scales used here are principally based on the properties of the medium. The ocean is considered purely stratified. In the case of pure stratification, layer growth is eventually arrested due to buoyancy effects, because there is no energy source to balance losses to buoyancy and viscosity, turbulence decays in time (Symth & Moum 2000). The Ozmidov scale L_o, is the scale at which eddies are deformed by buoyancy.

$$L_o = \sqrt{\frac{\varepsilon}{N^3}} \tag{4-14}$$

Respectively, the Ozmidov velocity and time scales are:

$$U_{L_o} = \sqrt[3]{L_o \varepsilon} \tag{4-15}$$

$$\tau_{L_o} = \frac{\sqrt{\varepsilon / N^3}}{\sqrt[3]{L_o \varepsilon}} \tag{4-16}$$

The largest eddy size in the *r*-direction is taken as 10km, the boundary of the short range propagation flow. The viscous dissipation length scale or the Kolmogorov scale characterizes the very smallest, dissipative eddies.

$$\eta = \sqrt[4]{\frac{\nu^3}{\varepsilon}} \tag{4-17}$$

Respectively, the Kolmogorov velocity and time scales are:

$$u_\eta = (\nu\varepsilon)^{1/4} \tag{4-18}$$

$$\tau_\eta = \sqrt{\frac{\nu}{\varepsilon}} \tag{4-19}$$

The smallest eddy diameter is taken to be 0.00001km. Eddies of the inertial subrange, those of sizes that fall in between the Ozmidov scale and the Kolmogorov scale have velocity and time scales that can be found from ε and ℓ, and are shown in relation to the Kolmogorov scale. Eddies of the inertial subrange will be modeled in these simulations.

$$u(\ell) = (\varepsilon\ell)^{1/3} = u_\eta (\ell/\eta)^{1/3} \tag{4-20}$$

$$\tau(\ell) = \left(\frac{\ell^2}{\varepsilon}\right)^{1/3} = \tau_\eta \left(\frac{\ell}{\eta}\right)^{2/3} \tag{4-21}$$

The upper limit of the Kolmogorov scale is $\ell_{DI} = 10\eta$, where DI = Dissipation-Inertial (Symth & Moum, 2000). The lower bound of the energy containing range is $\ell_{OI} = (1/6)L_0$, where OI = Ozmidov-Inertial (Pope 2001). Therefore the bound of the inertial scale is $10\eta \le \ell \le (1/6)L_0$. These limits can be observed in Figure 4-2.

4.2.2 *Frozen Turbulence Hypothesis*

In this work the G. Taylor (1938) "Frozen Turbulence Hypothesis" will be applied. This hypothesis postulates that since the sound will pass through the turbulence in a time that is short compared to the timescale of the evolution of turbulence, the turbulence can be approximated as "frozen" during the passage of an acoustic wave. Thereby, the sound-speed dependence on time can be neglected for a sound impulse transmitted from a source to a receiver (Figure 1-1).

4.3 Turbulence Spectrum

As mentioned previously, a random field is statistically stationary if all statistics are invariant under a shift in time. Similarly, the field is statistically homogeneous if all statistics are invariant under a shift in position. For homogeneous turbulence, the spectra

remain the same in both the temporal and spatial domains (Tennekes & Lumley, 1972). If the field is also statistically invariant under rotations and reflections of the coordinate system then the field is isotropic and is analyzed using the Kolmogorov spectrum for isotropic turbulence in the spatial domain.

4.3.1 *Kolmogorov Spectrum*

In 1941, A. Kolmogorov postulated that the one-dimensional energy spectrum *E(k),* within the inertial subrange can only depend on length scale, measured by wavenumber *k*, and dissipation rate ε, and through dimensional analysis arrived at the famous Kolmogorov $-5/3$ spectrum as a function of vortex size:

$$E(k) = C\varepsilon^{2/3}k^{-5/3}, k = 2\pi/L \quad \textbf{(4-22)}$$

Here *C* is the universal Kolmogorov constant and is empirically taken to be 1.5. The Kolmogorov hypothesis is consistent only for only a portion of the spectrum, the inertial subrange, (further discussed in Section 4.2.1). This spectrum has a slope of $k^{-5/3}$.

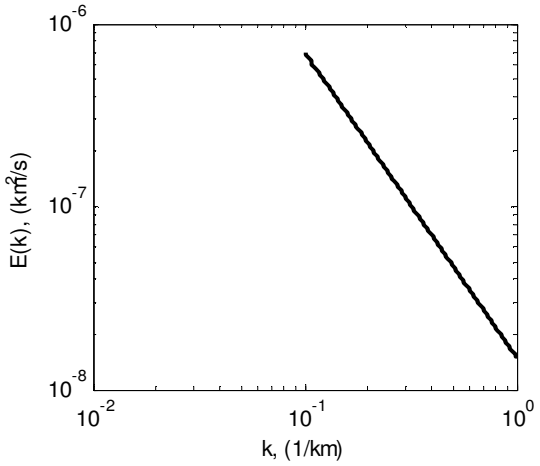

Figure 4-3: Kolmogorov Spectrum *E(k),* Inertial Subrange.

The Kolmogorov hypothesis can be developed to form a model energy spectrum for all wavenumbers, including the energy-containing subrange and the dissipation subrange. The following is a simple representation of a model spectrum taken from Pope (2001), see Figure 4-4.

$$E(k) = C\varepsilon^{2/3}k^{-5/3}f_{L_o}(kL_o)f_\eta(k\eta) \quad \textbf{(4-23)}$$

Where,

$$f_{L_o}(kL_o) = \left(\frac{kL_o}{\left[(kL_o)^2 + C_{L_o} \right]} \right)^{5/3+p_0} \tag{4-24}$$

$$f_\eta(k\eta) = \exp\left\{ -\beta\left([k\eta]^4 + C_\eta^4 \right)^{1/4} - C_\eta \right\} \tag{4-25}$$

Here C, C_{L_o}, C_η, and β, are positive constants found empirically to be: $C \approx 1.5$, $C_{L_o} \approx 6.78$, $C_\eta \approx 0.40$, $p_0 = 2$, and $\beta \approx 5.2$. The energy spectrum is a useful tool in analysis because it indicates how much activity is occurring on a given length scale. The wavenumber specifies the scale at which the perturbations can form and the amplitude of the spectrum represents the amount to expect for a given length scale. This spectrum has the same dissipation slope as before, $k^{-5/3}$, but has an added production slope of k^2.

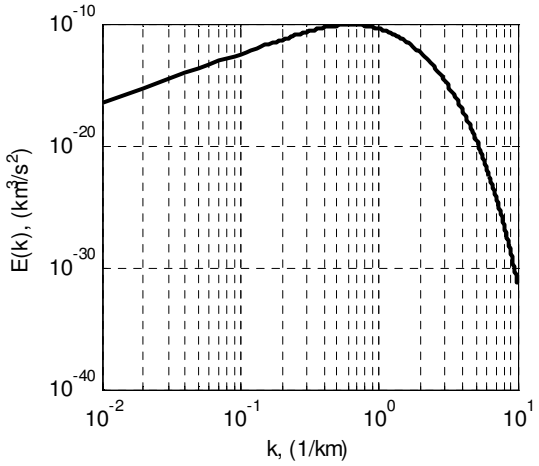

Figure 4-4: Kolmogorov Spectrum *E(k)*, over all length scales.

4.3 Garrett-Munk Spectrum of Internal Waves

The internal wave spectrum in the deep ocean has consistently the same shape wherever it is observed, except when the observations are made close to a strong source of internal waves (Lvov & Tabak, 2001). Based on these field observations, Garrett and Munk (1979) developed an energy-frequency spectrum, known as the Garrett-Munk spectrum of internal waves, Figure 4-5. In Figure 4-5, the wave frequency is plotted on the x-axis in cycles per hour (cph) and the energy per wave frequency $\left(m^2/cph\right)$ is plotted on the y-axis. Internal waves evolve over a wide spectrum of frequency scales,

depending on their wavelength. In internal wave spectrum below, the buoyancy frequency is the upper limit of wave frequencies, ω that can propagate through a system. The lower limit of internal wave frequencies is the Coriolis or inertial wave frequency, *f*. The inertial frequency is defined as $f = 2\Omega\sin\varphi$, where Ω is the angular velocity of the earth's rotation and φ is the latitude. At *f*, wave motions become inertial oscillations, where particles have horizontally circular trajectories (Wadzuk & Hodges, 2004)

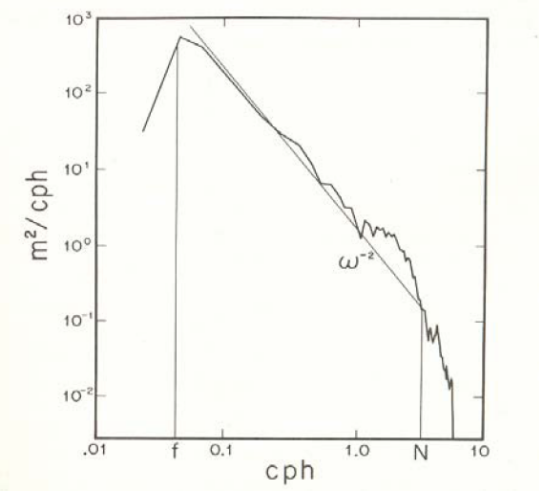

Figure 4-5: Garrett-Munk Spectrum of Internal Waves, *E(ω)*

The following is the empirical expression for spectral energy as proposed by Garrett and Munk:

$$E(k,m) = \frac{2fNE\left(m/m^*\right)}{\pi\left(1+\left(m/m^*\right)^{5/2}\left(N^2k^2+f^2m^2\right)\right)} \quad \textbf{(4-26)}$$

Where *E* is a constant quantifying the total energy content of the internal wave spectrum, *N* is the buoyancy frequency, *f* is the Coriolis parameter, *k* and *m* are the horizontal and vertical components of the wavevector respectively, and m^* is a reference vertical wavenumber to be determined from observations. This spectrum is further simplified by Lvov & Tabak (2001) by assuming $|m| >> m^*$ and $|\omega| >> f$, ω is the frequency of the wave. The Garrett-Munk spectrum then becomes:

$$E(k,m) \cong \left(k^2 m^{3/2}\right)^{-1} \quad \textbf{(4-27)}$$

This equation shows the Garrett-Munk spectrum to have a slope of k^{-2}.

5 SIMULATION

This section describes the programs developed for this thesis and the subroutines within those programs. Scripts were written in MATLAB 7.1, software developed by the MathWorks Company, and license agreements are held by Worcester Polytechnic Institute.

This research simulates typical ocean environments for both long range and short range propagation. The algorithms pertaining to long range propagation are discussed in Part I of this Chapter and those simulating short range propagation are presented in Part II. Each solves the ray-based systems of ODEs, derived from the eikonal equations (Chapter 3), using a fourth-order Runge-Kutta method on a set of grid points uniformly spaced in range.

PART I

Long Range Propagation

The long range propagation environment is dominated by the internal wave field. This wave field is represented by a forcing function that is randomly perturbed in phase and amplitude by additive Gaussian white noise. In the analysis chapter the effects of noise intensity on chaotic ray behavior are investigated through the construction of bifurcation and phase diagrams, Poincaré maps, and maximum propagation range and timefront plots. The algorithms developed for the representation of the internal waves and the formation of the analysis plots are described below.

5.1 Bifurcation Algorithm

The bifurcation program is the main algorithm used in the chaos analysis, all other diagrams (phase planes, Poincaré maps, and maximum propagation plots) are variations based on this program. The attention is thereby focused to the development of bifurcation.m. The full script for this program can be found in Appendix I.

5.1.1 *Internal Wave Representation*

In Chapter 3 the following governing equations were derived:

$$\begin{aligned}
\frac{dz}{dr} &= p, \\
\frac{dp}{dr} &= -\frac{2}{B}c_0^2 c_{ch}\varepsilon\frac{1-e^{-2(z-z_a)/B}}{c(z)^3} + \frac{\sqrt{3}}{2B}e^{-3z/2B}(A+\zeta)\sin q(r), \\
\frac{dq}{dr} &= \frac{2\pi}{R} + \xi \\
\frac{d\tau}{dr} &= \frac{1}{2c_0}\left[1+p^2+\left(\frac{c_0}{c(z)}\right)^2\right] + \frac{1}{c_0}\left[\sqrt{2}e^{-3z/2B}(A+\zeta)\sin q(r)\right]
\end{aligned} \tag{5-1}$$

This set of ODE's can be solved using MATLAB's built-in function ode45, a fourth order Runge-Kutta solver:

◊ `[r,y] = ode45('oceanequations_IW',rspan,x,options)`

The first input to the function is oceanequations_IW, which is a subroutine containing the ODE's from Equation 5.1. The second is rspan, this serves as the "time-step." It is a vector that begins at the acoustic source, r = 0km and steps by the specified distance, for instance 1km, to the desired propagation distance, or location of the hydrophones, r =

1000km. The input x is an array containing the initial conditions needed for oceanequations_IW. An initial condition array of length 4, consisting of initial depth (z), ray slowness (p), internal wave phase (q), and time (τ) is needed for the ODE set. All initial condition values were chosen using the SLICE89 parameters listed in Table 2-2. The last input is options, which allows the change of the default integration properties, for example the use of a smaller tolerance. The outputs of the function ode45 are a vector r and a matrix y. The vector r is a column vector of range points and y is the solution matrix, where each row in y corresponds to the solution at a range returned in the corresponding row of r and each column in y corresponds to a parameter for which the initial conditions were specified (Mathworks. 2006). The subroutine oceanequations_IW is seen below; the equations are identical to those in Equation 5.1.

```
function xdot = oceanequations_IW(r,x)

global B za co c_ch ep A R D rspan noiseR noiseA
% calculating intermediate variables
z=x(1);  a=1-(exp(-2*(z-za)/B));   b=exp((-3*(z))/(2*B));
cz = c_ch*(1+ep*(exp((-2*(z-za))/B)+(2*(z-za)/B)-1));
% calculating dz/dr
xdot(1,1) = x(2);
% calculating dp/dr
xdot(2,1) = (-2/B)*(co*co)*(c_ch*ep)*(a/(cz*cz*cz)) +
((3*sqrt(2))/(2*B))*(noiseA)*b*sin(x(3));
% calculating dq/dr
xdot(3,1) = noiseR;
% calculating dT/dr
xdot(4,1) =
(1/(2*co))*(1+(x(2))^2+(co/cz)^2)+(1/co)*(sqrt(2)*noiseA*b*sin(x(3)));
```

The Gaussian white noise parameters for amplitude and wavelength are represented by the variables noiseA and noiseR, respectively. These variables are defined in the main program. Additive Gaussian white noise is represented by the built-in MATLAB function awgn.

- `noiseA = awgn(A,SNR)`
- `noiseR = awgn((2*pi)/R,SNR)`

The awgn function adds zero mean Gaussian white noise to the amplitude or phase vector, the scalar SNR specifies the signal-to-noise ratio per sample, in decibels, dB

(Mathworks, 2006). The SNR is a measure of signal strength relative to background noise (Lathi, 1998).

$$SNR = 20\log_{10}\left(\frac{Signal}{Noise}\right) \tag{5-2}$$

If the signal and noise strength are equivalent the SNR is 0dB and the signal is unreadable. A large the SNR indicates a stronger signal with little noise influence and a decrease in SNR suggests the presence of increased noise effects.

5.1.2 *User Inputs*

In the analysis of long range propagation it is necessary to vary different parameters of the internal wave fields: the amplitude, wavelength, and noise. This program makes constructing a desired wave field user friendly. Figure 5-1 is a block diagram of the overall flow of the program; this will help illustrate the role of the user prompts.

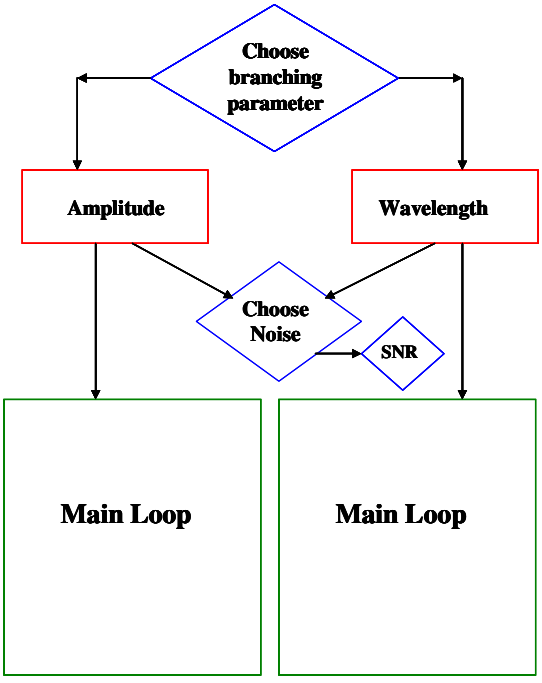

Figure 5-1: Block diagram for bifurcation.m

The program begins by prompting the user to decide which branch of the bifurcation diagram to vary, the internal wave wavelength or amplitude.

```
Choose your scenario:
1 - Varying IW Wavelength
2 - Varying IW Amplitude
```

This decision determines which main loop is to be run, one that runs through varying amplitude or one that runs through varying wavelength. The noise scenario is next chosen.

```
Stochastic scenario:
1 - R only
2 - A only
3 - both
4 - no noise
```

If the option for no noise is selected the program skips the next steps and proceeds to the main loop. If noise is to be added to only one parameter, a value of SNR is selected.

```
Enter a value for SNR (5dB, 15dB, 25dB) :
```

For noise added to both parameters the user must provide SNR values for both A and R.

```
Enter a value for SNR in R(5dB, 15dB, 25dB) :
Enter a value for SNR in A(5dB, 15dB, 25dB) :
```

5.1.3 *Main Loop*

The program is now directed to the main loop. The loops are varied for the desired bifurcation parameter, both loops follow identical procedures. Figure 5-2 is a block diagram describing the flow of the main loop for a varying branching parameter.

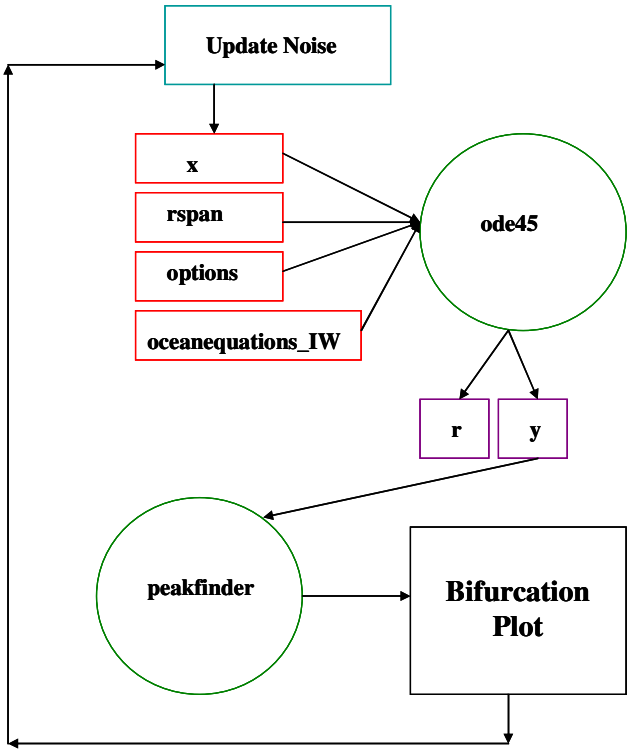

Figure 5-2: Block Diagram of main loop, bifurcation.m

The loop first updates the noiseA and noiseR variables depending on what was chosen as a scenario. The inputs for the ode45 function, as described in the previous section are defined and sent to the function. The function outputs the solution matrix. The variables, z, p, q, and τ, are extracted from the solution matrix. A bifurcation plot, describes the behavior of the traveling ray, a plot of the depth of each traveling ray at its peaks versus the current value of the branching parameter. The developed function peakfinder.m determines the peaks based on the change in slope of p, the ray slowness. The input is the p column vector taken from the solution matrix. The output is an array containing the peak values of p and index number at which they occur. The indices determine the corresponding depth value. These depth values are plotted as a scatter plot versus the branching parameter, forming the bifurcation diagram, either as a function of internal wave amplitude or wavelength. The loop updates and repeats for all values of the branching parameter.

```
function [peak,index] = peakfinder(array)

slope1 = 0;  slope2 = 0;  n = 0;

for i = 1:1:(length(array)-1)
    slope1 = (array(i+1)+array(i));
        if (slope1 > 0) & (slope2 < 0)
        n = n + 1;
        index(n) = i;
        peak(n) = array(i);
        end
    slope2 = slope1;
end
```

5.2 Variations of the Bifurcation Algorithm

Variations of this algorithm are used for chaos analysis, poincare.m and phase.m can be found in Appendix II and III, respectively. Poincare.m runs very similarly to this bifurcation algorithm, the only exception is that instead of the internal wave amplitude and wavelength being varied, the initial launch angle is varied.

5.3 Travel Time Prediction Algorithm

Again this program is based on solving the governing system of ODE's with the built-in MATLAB Runge-Kutta solver ode45. This program is structured similarly to the poincare.m coding, in that the main loop varies the initial launch angle at the source. The difference here is in the construction of the timefront plot. The subroutine peakfinder.m is longer needed. The timefront plot is the plot of the arrival depth versus the time of arrival of a ray. The arrival times and depths are extracted from the *y* matrix, and their values at the final propagation distance, for example, r = 1000km are plotted for each initial condition. These values are written to a file formatted as ASCII text, using the form bulleted below, time_iw is the variable being saved and Timefront_iw.dat is the file name. This format is compatible with MATLAB and as well as Microsoft Wordpad and Notebook.

- `save timefront_iw.dat time_iw -ascii`

PART II

Short Range Propagation

Our short range propagation environment is composed of three different turbulent environments.

- ◊ Simulated Turbulence
- ◊ Internal Wave Field
- ◊ Internal Wave and Simulated Turbulence Combined

The sound variation with depth found in the ocean environment is represented using Munk's canonical profile, the internal wave field by a forcing function randomly perturbed in phase and amplitude by additive Gaussian white noise, and the turbulence is modeled using the potential theory two wavenumber model. The analysis chapter presents the effects of these turbulent scenarios through ray tracing diagrams, timefront and phase plots, and turbulent velocity spectra. The algorithms developed for the representation of the turbulent features and the formation of the analysis plots are described below.

5.4 Travel Time Prediction Algorithm

The travel time prediction algorithm predicts the arrival behavior of a traveling pulse over short range propagation, 10km, for several realizations of the environment. The governing equations derived in Chapter 3 are solved using the fourth order Runge-Kutta ode45 solver, for details of this solver refer to PART I. First the representation of the environments is discussed.

5.4.1 *Munk's Canonical Profile Only*

This environment serves as the baseline for our simulations, it contains no outside perturbations. The one way ray equations include only Munk's canonical sound speed profile, which accounts for average temperature, salinity, depth, and pressure fluctuations. Equation 5.2, is the set of ODE's that is solved for an environment containing only the sound speed profile.

$$\frac{dz}{dr} = p,$$
$$\frac{dp}{dr} = -\frac{2}{B} c_0^2 c_{ch} \varepsilon \frac{1 - e^{-2(z-z_a)/B}}{c(z)^3}, \tag{5-3}$$
$$\frac{d\tau}{dr} = \frac{1}{2c_0}\left[1 + p^2 + \left(\frac{c_0}{c(z)}\right)^2\right]$$

An initial condition array of length 3, consisting of initial depth (z), ray slowness (p), and time (τ), is input to the function, oceanequations_SS.m, seen below. The ode45 solver returns a range vector and a solution matrix containing the values for each parameter at each corresponding range step. The equations seen in oceanequations_SS.m are identical to the equations from 5.2.

```
function xdot = oceanequations_SS(r,x)

global B za co c_ch ep
% calculating intermediate variables
z=x(1);     a=1-(exp(-2*(z-za)/B));    b=exp((-3*(z))/(2*B));
cz=c_ch*(1+ep*(exp((-2*(z-za))/B)+(2*(z-za)/B)-1));
% calculating dz/dr
xdot(1,1) = x(2);
% calculating dp/dr
xdot(2,1) = (-2/B)*(co*co)*(c_ch*ep)*(a/(cz*cz*cz));
% calculating dT/dr
xdot(3,1) = (1/(2*co))*(1+(x(2))^2+(co/cz)^2);
```

5.4.2 *Internal Wave Perturbations Only*

The internal wave ODE function oceanequations_IW.m was discussed in PART I and is again mentioned here. Below are the governing equations that are solved for an environment with an internal wave field.

$$\frac{dz}{dr} = p,$$
$$\frac{dp}{dr} = -\frac{2}{B} c_0^2 c_{ch} \varepsilon \frac{1 - e^{-2(z-z_a)/B}}{c(z)^3} + \frac{\sqrt{3}}{2B} e^{-3z/2B}(A + \zeta)\sin q(r),$$
$$\frac{dq}{dr} = \frac{2\pi}{R} + \xi \tag{5-4}$$
$$\frac{d\tau}{dr} = \frac{1}{2c_0}\left[1 + p^2 + \left(\frac{c_0}{c(z)}\right)^2\right] + \frac{1}{c_0}\left[\sqrt{2} e^{-3z/2B}(A + \zeta)\sin q(r)\right]$$

An initial condition array of length 4, consisting of initial depth (z), ray slowness (p), internal wave phase (q), and time (τ) is input to the solver. The output is a range vector and respective solution matrix. The subroutine oceanequations_IW.m is depicted below; the equations are identical to those in Equation 5.3. Additive Gaussian white noise is represented by the built-in MATLAB function awgn.

```
function xdot = oceanequations_IW(r,x)

global B za co c_ch ep A R D rspan noiseR noiseA
% calculating intermediate variables
z=x(1);  a=1-(exp(-2*(z-za)/B));   b=exp((-3*(z))/(2*B));
cz = c_ch*(1+ep*(exp((-2*(z-za))/B)+(2*(z-za)/B)-1));
% calculating dz/dr
xdot(1,1) = x(2);
% calculating dp/dr
xdot(2,1) = (-2/B)*(co*co)*(c_ch*ep)*(a/(cz*cz*cz)) +
((3*sqrt(2))/(2*B))*(noiseA)*b*sin(x(3));
% calculating dq/dr
xdot(3,1) = noiseR;
% calculating dT/dr
xdot(4,1) =
(1/(2*co))*(1+(x(2))^2+(co/cz)^2)+(1/co)*(sqrt(2)*noiseA*b*sin(x(3)));
```

5.4.3 *Simulated Turbulence Field*

This system of ODE's is solved for an environment of sound speed perturbations induced by an eddy field and those sound speed fluctuations attributed to Munk's canonical sound speed profile.

$$\begin{aligned}
\frac{dz}{dr} &= p, \\
\frac{dp}{dr} &= -\frac{2}{B} c_0^2 c_{ch} \varepsilon \frac{1 - e^{-2(z-z_a)/B}}{c(z)^3}, \\
\frac{d\tau}{dr} &= \frac{1}{2c_0}\left[1 + p^2 + \left(\frac{c_0}{c(z)}\right)^2\right]
\end{aligned} \tag{5-5}$$

An initial condition array of length 3, consisting of initial depth (z), ray slowness (p), and time (τ), is input to the function, oceanequations_ED.m.

```
function xdot = oceanequations1(r,x)

global B za co c_ch ep rspan

% calculating intermediate variables
z=x(1);    a=1-(exp(-2*(z-za)/B));   b=exp((-3*(z))/(2*B));
cz=c_ch*(1+ep*(exp((-2*(z-za))/B)+(2*(z-za)/B)-1));
[fluct] = eddy1(r,z);
cz = cz + fluct;
% calculating dz/dr
xdot(1,1) = x(2);
% calculating dp/dr
xdot(2,1) = (-2/B)*(co*co)*(c_ch*ep)*(a/(cz*cz*cz));
% calculating dT/dr
xdot(3,1) = (1/(2*co))*(1+(x(2))^2+(co/cz)^2);
```

Within the ODE solver is the subroutine eddy1.m, which accounts for those velocity fluctuations induced by the randomly assembled vortices. This subroutine requires an input of the location of the pulse, the current r and z values. Velocity vectors are calculated by determining the distance between each individual eddy and the current pulse location, the input parameters are r and z. The subroutine uses this information to calculate the horizontal and vertical velocities induced on the traveling pulse due to each eddy from the field. The total fluctuating velocity is the sum of each eddy velocity vector encountered by the pulse. The output is the sum of the resultant fluctuating velocity, which is added to the sound speed, thereby accounting for the turbulence fluctuations induced by the eddy field. The ODE45 solver outputs the range vector and corresponding solution matrix containing the values for each parameter its respective range.

```
function [ufluct,vfluct,fluct] = eddy1(r,z)
global z_eddy r_eddy gamma n
for s=1:n
    dz = z_eddy(s) - z;
    if r < r_eddy(s)
        dr = r_eddy(s) - r;
        theta = dz/dr;
        l = sqrt(dz^2 + dr^2);
        V_eddy = gamma(s)/(2*pi*l);
        u(s) = V_eddy*cos(theta);
        v(s) = V_eddy*sin(theta);
    elseif r == r_eddy(s)
        u(s) = 0;
        v(s) = 0;
    elseif r > r_eddy(s)
        dr = r - r_eddy(s);
```

```
        theta = dz/dr;
        l = sqrt(dz^2 + dr^2);
        V_eddy = gamma(s)/(2*pi*l);
        u(s) = V_eddy*cos(theta);
        v(s) = V_eddy*sin(theta);
    end
end
ufluct = sum(u);
vfluct = sum(v);
fluct = sqrt(ufluct^2 + vfluct^2);
```

5.4.4 *Internal Wave and Simulated Turbulence Combined*

This environment contains all perturbations: ocean property fluctuations, internal waves, and a turbulent field. The same set of ODE equations listed in Equation 5.3 must be solved. An initial condition array of length 4, consisting of initial depth (z), ray slowness (p), internal wave phase (q), and time (τ), is input to the ode45 solver. The function oceanequations_COMBO.m contains the system of ODEs to be solved. This function also contains the eddy1.m subroutine. Again the output is the range vector and respective solution matrix.

```
function xdot = oceanequations_COMBO(r,x)

global B za co c_ch ep A R rspan noiseR noiseA t U q1 q2 beta al y1 x1
% calculating intermediate variables
z=x(1);    a=1-(exp(-2*(z-za)/B));   b=exp((-3*(z))/(2*B));
cz=c_ch*(1+ep*(exp((-2*(z-za))/B)+(2*(z-za)/B)-1));
[fluct] = eddy1(r,z);
cz = cz + fluct;
% calculating dz/dr
xdot(1,1) = x(2);
% calculating dp/dr
xdot(2,1) = (-2/B)*(co*co)*(c_ch*ep)*(a/(cz*cz*cz)) +
((3*sqrt(2))/(2*B))*(noiseA)*b*sin(x(3));
% calculating dq/dr
xdot(3,1) = noiseR;
% calculating dT/dr
xdot(4,1)=
1/(2*co))*(1+(x(2))^2+(co/cz)^2)+(1/co)*(sqrt(2)*noiseA*b*sin(x(3)));
```

5.5 Realization Loop

This algorithm was developed similarly to the timefront_iw.m program discussed in PART I. The difference is that the initial launch angle is not varied; instead a

timeseries is created to analyze the sound passage through the flow field over time. The initial conditions remain constant and only the perturbations evolve through time. Since the speed of sound is so much greater than the phase speed of internal waves or the turnover time of eddies, the ocean medium is assumed frozen for the acoustical transmissions. Code for realizations_short.m is found in Appendix V.

Figure 5-3 is a block diagram representing the flow of this algorithm. The program first defines the constant variables: timeseries array, sound speed constants, internal wave parameters, and noise parameters. The strategy used here is to populate the fluid with a finite number of two-dimensional vortices of random strengths and of random locations. Location is chosen to be within the region of the sound channel axis and specified range of propagation. The eddy dimensions, r_{vortex} and $v_{\theta_{vortex}}$, are necessary for calculating the circulation values. The eddy radius, r_{vortex}, is chosen to be typical to the defined length scales of inertial and lower portion of the energy containing subrange. Average circulations values for eddies of this size are a few cm^2/s, the eddy velocity $v_{\theta_{vortex}}$ is thereby chose accordingly, (NOAA, 1997). These values are randomly generated, using the MATLAB command, rand. The rand command generates random values for between 0 and 1, and these are multiplied by a scaling factor appropriate to the parameter, these are depicted in Table 6-1. A table of the eddy radius, circulation values, and location is printed to the screen for reference. The respective circulation values and eddy locations passed on to the main loop.

Eddy Parameters			
r_vortex	Circulation	r-position	z-position
0.615432	-1.79985e-008	7.62097	1.14016
0.791937	-2.81289e-008	4.56468	0.277366
0.921813	1.04944e-008	0.185036	0.728211
0.738207	-6.02593e-009	8.21407	0.583179
0.176266	-5.64512e-007	4.44703	1.06956

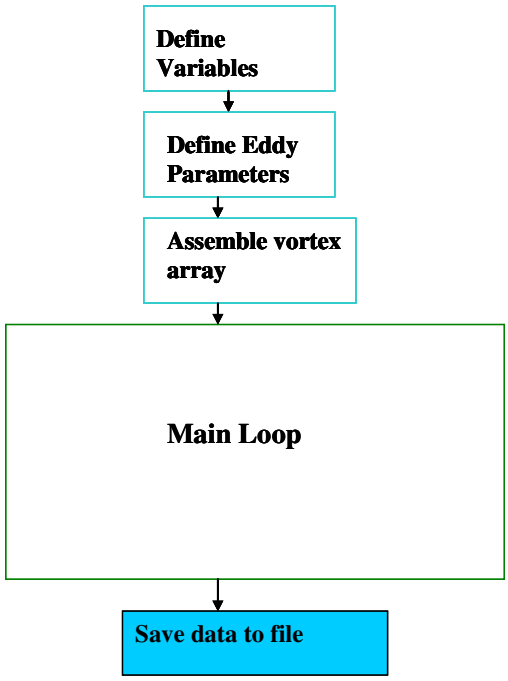

Figure 5-3: Block diagram for realizations_short.m

The main loop updates the eddy field positioning, which is being conducted with the ambient current, noise parameters are also updated to be a new random value for each realization. The scenarios are solved using the ode45 solver with its respective function containing its governing set of ODE's, described in the previous sections. This loop is carried out over the specified timeseries and the arrival time, arrival angle, and arrival depth at the maximum propagation distance are stored in an array for each realization and scenario. At the termination of the loop these matrices are written to a file formatted as ASCII text, using the form bulleted below.

- `save time_ss.dat time_ss -ascii`
- `save time_ed.dat time_ed -ascii`
- `save time_combo.dat time_combo -ascii`
- `save time_iw.dat time_iw -ascii`

This format is compatible with MALTAB and as well as Microsoft Wordpad and Notebook.

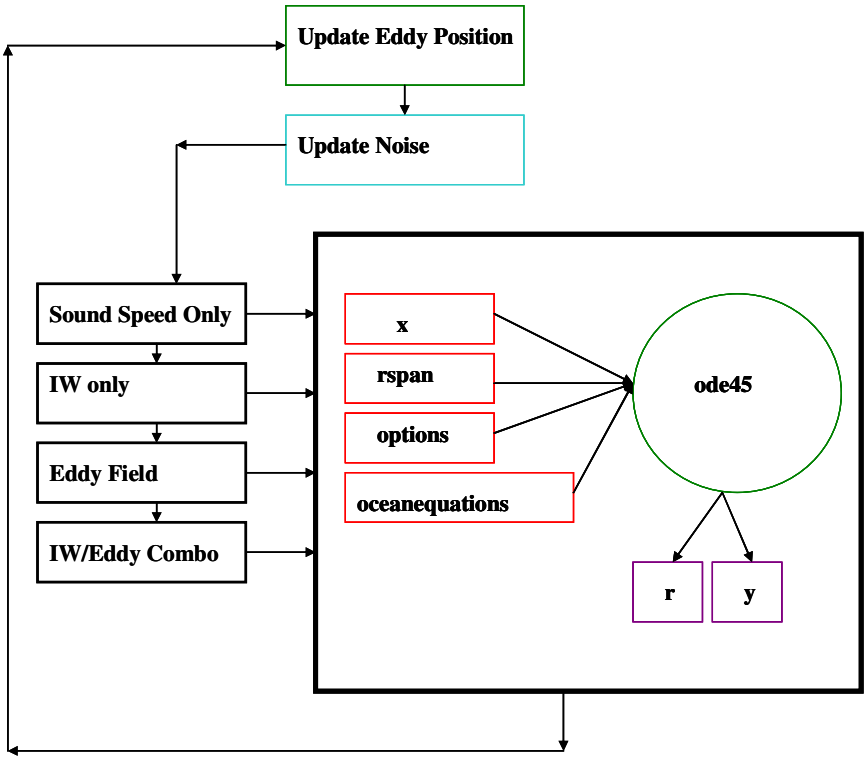

Figure 5-4: Block Diagram of Main loop, realizations_short.m

5.6 Spectrum Algorithm

The script for this algorithm is in Appendix VI. The program realizations_short.m recorded the arrival time, depth, and angle over the maximum propagation distance for each realization. This program utilizes those created ASCII files to plot the fluctuating MTV spectrums of each scenario.

5.6.1 *Main Program*

This algorithm creates the fluctuating velocity spectrum in frequency space, the timefront plot, and a plot of the fluctuating MTV over time for each of the turbulent environments. All environments are plotted on the same axes for easy observation; accept for the environment with no perturbations, which is plotted separately.

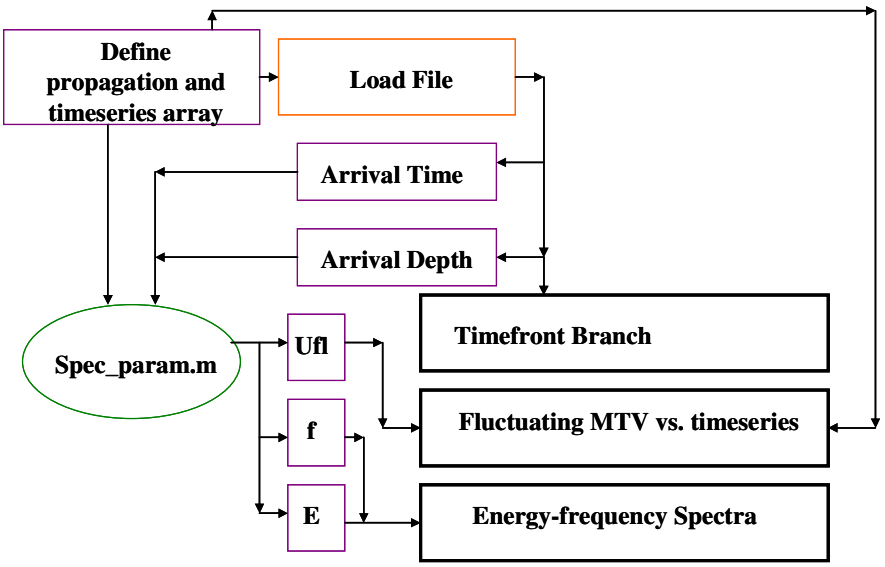

Figure 5-5: Block Diagram of main program, spectrum.m

The arrival times and depths are extracted from the ASCII files and sent to the function, Spec_param.m. The fluctuating portion of the mean travel velocity is separated from the mean and the autocovariance is taken. The Fourier transform of the autocovariance is twice the frequency spectrum of the fluctuation. The fast Fourier transform of the autocovariance is taken using the MATLAB built in function FFT. If the time series has an odd number of elements, to improve computation efficiency the vector length must be a power of 2, so the time series needs to be padded with zeros and extended to have even elements (MathWorks, 2006). Only the real part of the spectrum is considered. Taking the transform yields elements that are equally spaced in frequency within the Nyquist interval. The Nyquist interval is the maximum time interval between the equally spaced samples of a timeseries (Lathi, 1998). The Nyquist interval is the reciprocal of twice the sampling frequency (Lathi, 1998).

$$f_{Ny} = \frac{1}{f_s} \tag{5-6}$$

Thereby, frequency values for this spectrum in frequency space are multiplied by the Nyquist frequency.

```
function [E,f,Ufl] = spec_param(T)

global rfinal

for i=1:length(T)
    Uvel(i) = rfinal/T(i);
end

Uvel = Uvel';
cm = mean(Uvel);
Ufl = Uvel - cm;
U = xcorr(Ufl);
E = fft(U,30);
E = E.*conj(E)/(30*30);
E = (1/2)*E(1:16,:);
f = (1/(2*10))*(0:15)/15;
```

This function outputs the following vectors, energy, frequency, and turbulent velocity. These variables are plotted accordingly.

6 ANALYSIS

This Analysis chapter is separated into two parts. The first intends to justify this internal wave model. Here this intension is not precisely quantifying the acoustic fluctuations due to the internal waves but rather to demonstrate that the addition of random fluctuations leads to different characteristics in the acoustic arrivals during long range propagation, where it is believed that internal waves are the dominant source of acoustic fluctuations (Tang & Tappert, 1997). The effect of noise intensity on chaotic ray behavior is examined through the construction of bifurcation and phase diagrams, Poincaré maps, and maximum propagation range and timefront plots. The latter section presents the numerical results for the other perturbations scenarios that affect sound transmission during short-range propagation. This section characterizes the acoustic signals in a multi-path underwater environment by predicting signal delay and behavior. Results are presented through ray tracing diagrams, branches of timefront plots, and turbulent velocity spectra.

PART I

Long Range Propagation

6.1 Bifurcation and Phase Plane Analysis

"Bifurcation analysis by means of a control parameter is very useful from an engineering perspective; one may investigate the qualitative changes of the system dynamics," states Weircigroch *et al.* (1999). In considering an autonomous system a bifurcation diagram is constructed using Poincaré maps computed for different values of the branching parameter. The internal wave amplitude, *A,* and the internal wave wavelength, *R*, are the appropriate variables to use as branching parameters. Figure 6-1 demonstrates the process by which these diagrams are constructed. The Figure is drawn in the *z-p* phase plane, mapping of $z_N \rightarrow z_{N+1}$ is taken at the *z*-axis where *p=0*, where the ray crosses in the direction of $p^- \rightarrow p^+$. These points are recorded for each parameter value and assembled as the bifurcation diagrams. In a more physical sense, the bifurcation is a plot of the depth at which the traveling ray peaks, versus the varying branching parameter.

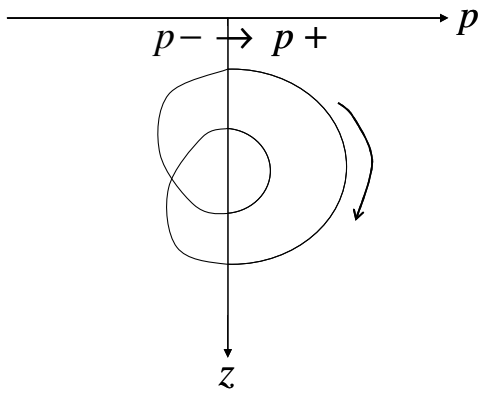

Figure 6-1: Schematic of Bifurcation Diagram Assembly

In order to present comparison in the following results, bifurcation diagrams and phase planes are plotted for two cases: (I) for purely deterministic excitation (no added noise) and (II) for deterministic excitation plus stochastic perturbation (noise in either the wavelength (SNR_R), amplitude (SNR_A), or both parameters of the internal wave).

6.1.1 *Bifurcation and Phase Plane Analysis,* $z = f(R)$

The influence of the wavelength, R onto the depth z, for a fixed value of the amplitude, A ($A = 0.005km$) and propagation range of 1000km is shown in the bifurcation diagram, Figure 6-2 which was constructed based on the ray acoustic equations that do not include the influence of random excitation. The internal wavelength R varies from 0 to 30km. The effect of chaotic behavior of internal waves is small up to $R = 8km$. As R continues to increase, the rays diverge and the system response becomes irregular. There is however no predicted surface intersection on the studied range of R.

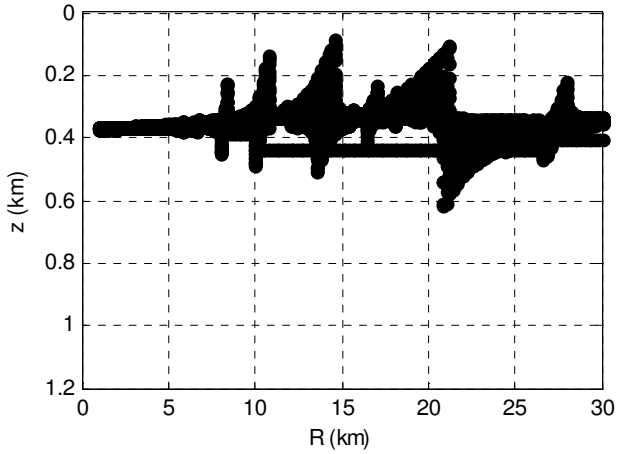

Figure 6-2: Bifurcation Diagram, $z = f(R)$. $A = 0.005km$**, no noise**

Figure 6-3 - Figure 6-5 show bifurcation diagrams for random fluctuations in wavelength, (GWN is added only to R). It is clear that the region with regular steady behavior, $1km \le R \le 8km$ seen in Figure 6-2, has been replaced with irregular chaotic acoustic ray behavior, as the SNR decreases. Rays tend to diverge and intersect the ocean surface (z = 0km) with increasing internal wave wavelength. The first intersection is seen when $SNR_R = 5dB$ and $R = 16km$ and rays continuously intersect the surface at points thereafter. This is behavior that goes unobserved in simulations without the addition of random perturbations. The remainder of the numerical experiments will be conducted using Figure 6-2 as a guide for choosing the wavelengths of interest and then compared to those with the addition on GWN.

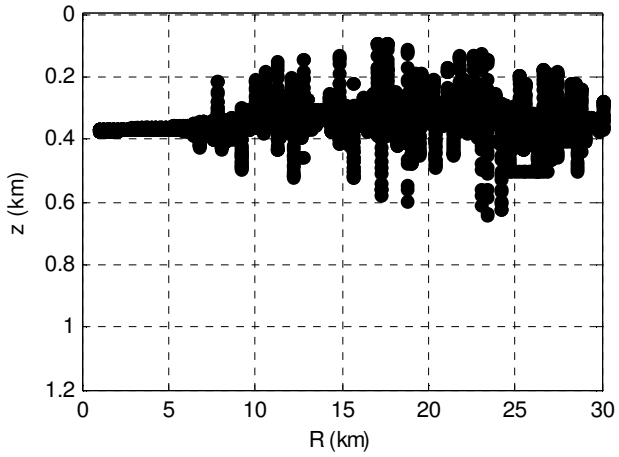

Figure 6-3: Bifurcation Diagram, $z = f(R).\ A = 0.005km, SNR_R = 25dB$

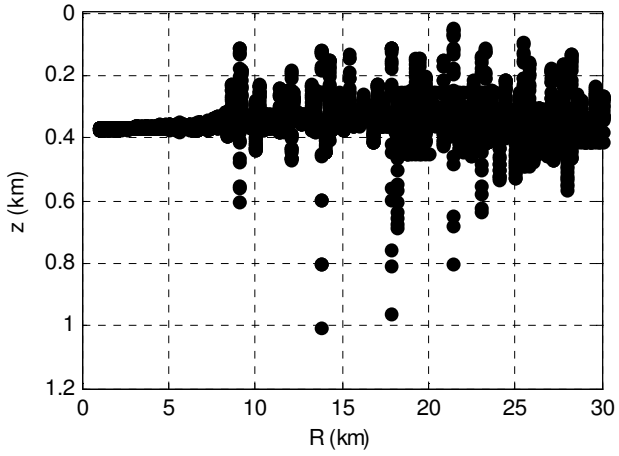

Figure 6-4: Bifurcation Diagram, $z = f(R).\ A = 0.005km, SNR_R = 15dB$

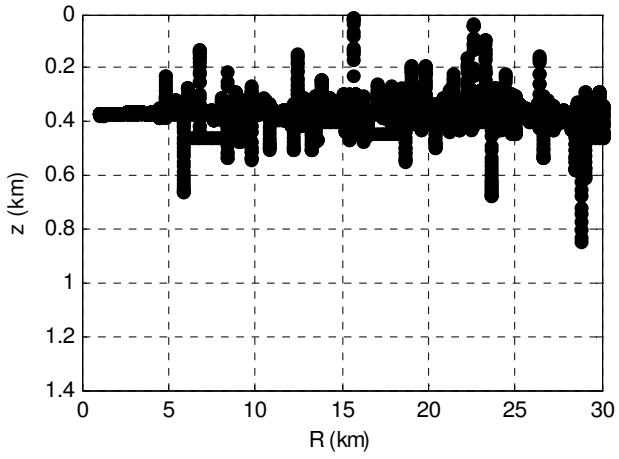

Figure 6-5: Bifurcation Diagram, $z = f(R).\ A = 0.005km, SNR_R = 5dB$

In order to investigate such behavior in detail, the phase planes for specific values of the wavelength are plotted. The phase planes presented below, are the wave ray trajectories in the $z-\varphi$ plane, computed for A=0.005km. The phase diagram plotted for the value R=3.0km, corresponds to the region with the unique stable solution shown in Figure 6-3. The projection is consistent with the characteristic of a quasi-periodic motion which does not break off or change to a different type of motion. This behavior is in agreement with the conclusions made by Wiercigroch *et al.*, (1999), that for an internal wave perturbation of wavelength R=3km and a launch angle 7.5° wherein wave rays remain trapped in the sound channel.

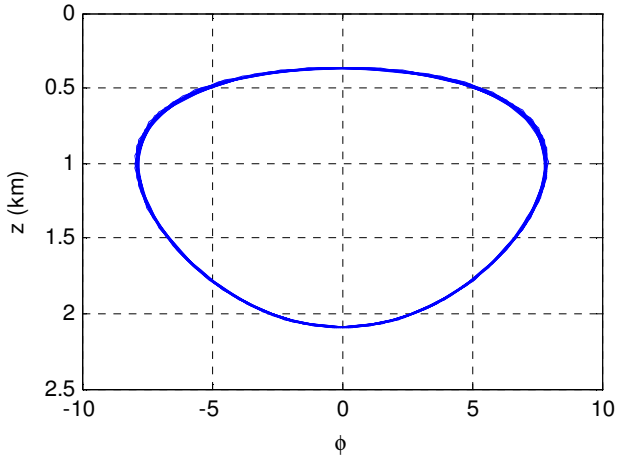

Figure 6-6: Phase Plane. $A = 0.005km, R = 3km, SNR_R = 25dB$

For a value of R=8.2km, the exact location of a spike in the referenced bifurcation diagram, phase planes are plotted for systems both without and with Gaussian white noise, respectively. Figure 6-7, without white noise again reveals the quasi-periodic motion. The left is the entire phase plane while the right is a zoomed-in portion of the trajectories. Figure 6-8, shows the phase plane with added white noise with an SNR of 25dB. The trajectory loop does not close as illustrated in the zoomed-in portion of the plane, indicated by the red dashed rectangle. The increased intensity of added white noise exhibits windings and intricate structure, indicating the presence of microcaustics and microfolds (indicated by the green circle); this is not evident from a phase plane

obtained as a solution of ray equation that accounts for deterministic excitation only (Simmen et al., 1997).

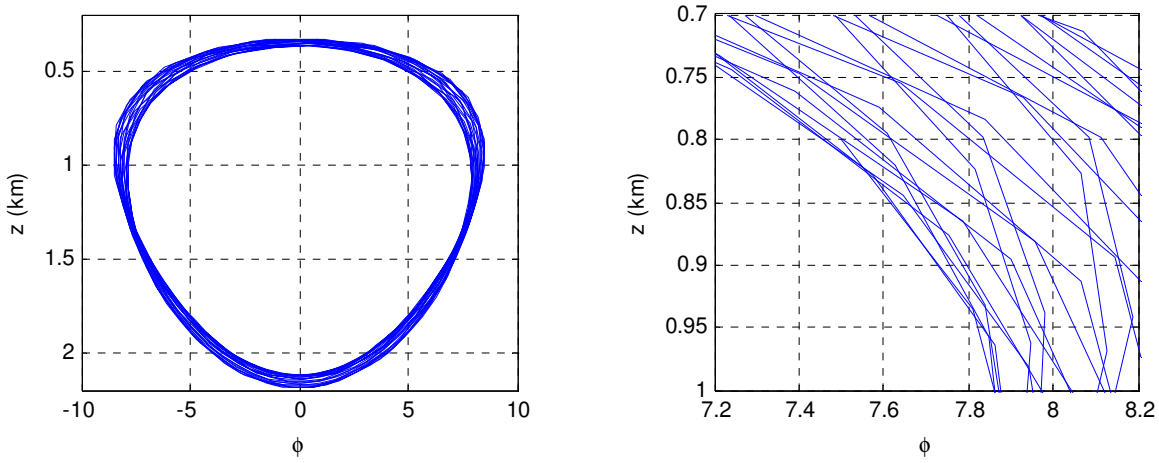

Figure 6-7: Phase Plane. $A = 0.005km, R = 8.2km$ **, no noise. LEFT: full scale. RIGHT: zoom.**

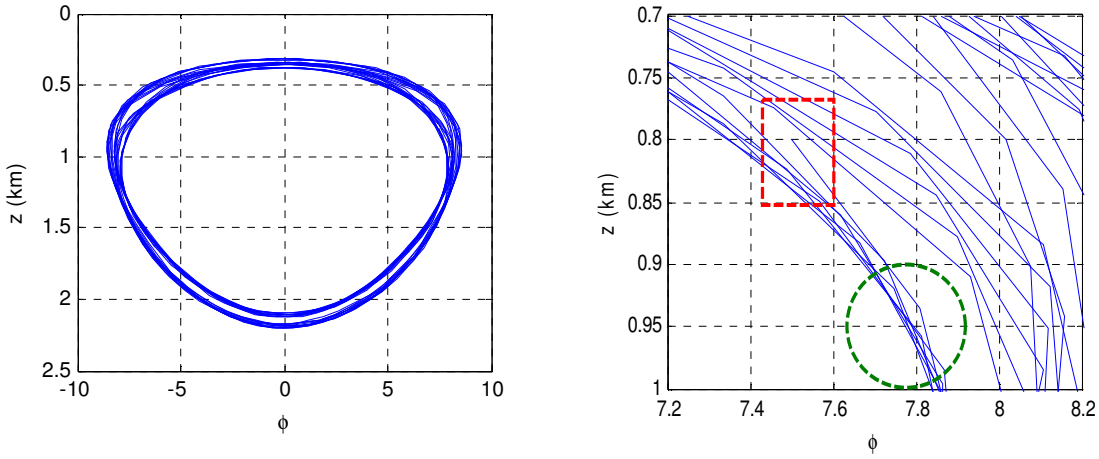

Figure 6-8: Phase Plane. $A = 0.005km, R = 8.2km, SNR_R = 25dB$ **. LEFT: full scale. RIGHT: zoom.**

Figure 6-9 - Figure 6-12, demonstrate the results for a deterministic system with an increased amplitude, *A=0.03km* where there are more frequent irregular responses. Without considering the addition of white noise, the first surface intersection is predicted for a wavelength $R \cong 7km$. Addition of a strong SNR leads to a different response, namely almost immediate ray divergence, rapid surface intersections, and this increase of noise intensity results in a visibly less dense response, which means that some rays immediately intersect the surface. Although this increased amplitude is unrealistic for an

ocean internal wave it is presented here to illustrate that internal wave amplitude does have a substantial effect on ray surface intersection and divergence as a function of wavelength.

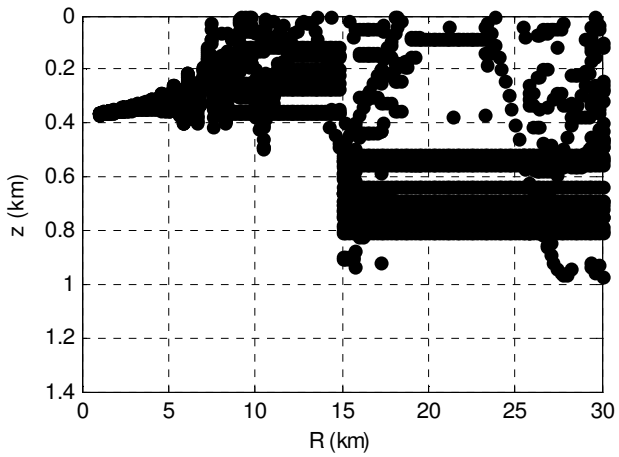

Figure 6-9: Bifurcation Diagram, $z = f(R)$. $A = 0.03km$**, no noise**

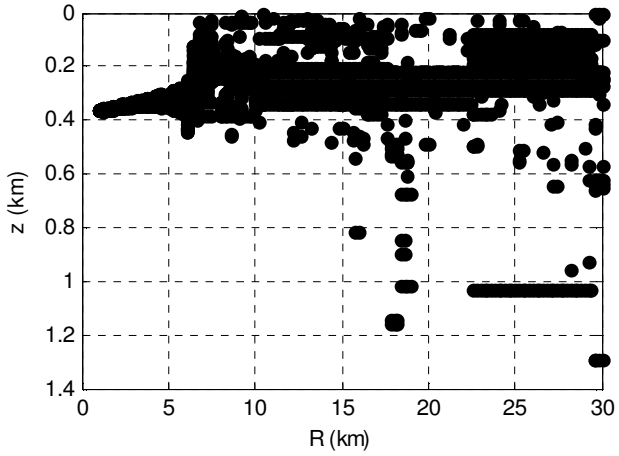

Figure 6-10: Bifurcation Diagram, $z = f(R)$. $A = 0.03km, SNR_R = 25dB$

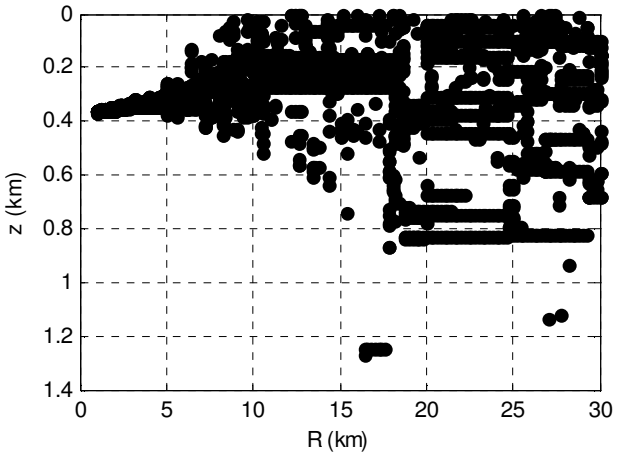

Figure 6-11: Bifurcation Diagram, $z = f(R)$. $A = 0.03km, SNR_R = 15dB$

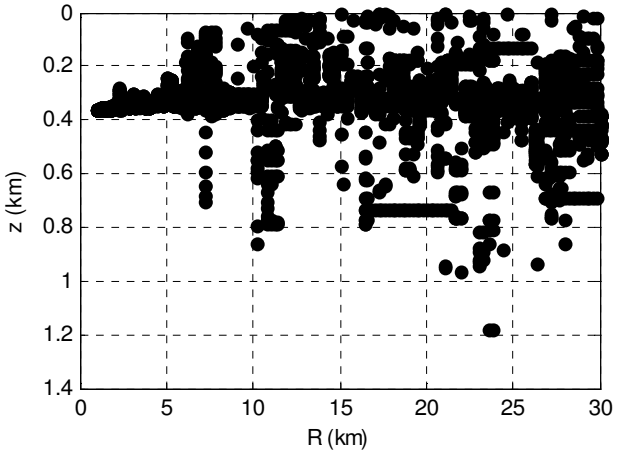

Figure 6-12: Bifurcation Diagram, $z = f(R)$. $A = 0.03km, SNR_R = 5dB$

6.1.2 *Bifurcation and Phase Plane Analysis,* $z = f(A)$

The second parameter of interest is the amplitude of internal waves; here GWN is added only to A. Bifurcation diagrams, $z = f(A)$, are constructed for two fixed wavelengths: $R = 1km$ and $R = 11.2km$, where $R = 1km$ corresponds to the region of regular behavior seen in Figure 6-2, and $R = 11.2km$ is the exact location of a spike on that figure. Again propagation range is 1000km. For the purpose of mathematical interest, an A range is used out of convenience, $0.001 \le A \le 0.03$. At small values of A, the diagram on plotted for non-disturbed media and a fixed wavelength $R = 1km$ suggests a stable unique solution.

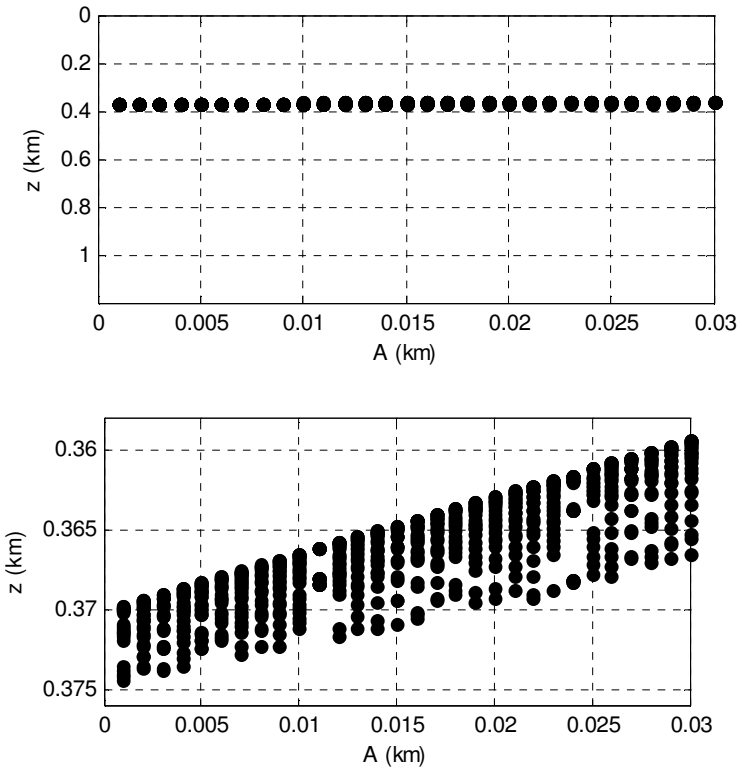

Figure 6-13: Bifurcation diagram, $z = f(A)$. $R = 1km$, no noise. TOP: full scale. BOTTOM: zoom.

The effect of random fluctuations, GWN added to the wave amplitude with SNR of 5dB, 15dB, and 25dB, is examined in Figure 6-14 - Figure 6-16. Here the addition of GWN causes sudden jumps of amplitude and highly instable behavior is apparent, the diagrams again appear less dense indicating rapid surface intersection. This further confirms that behavior of internal waves with chaotic and stochastic effects has a very strong dependence of on the intensity of fluctuations.

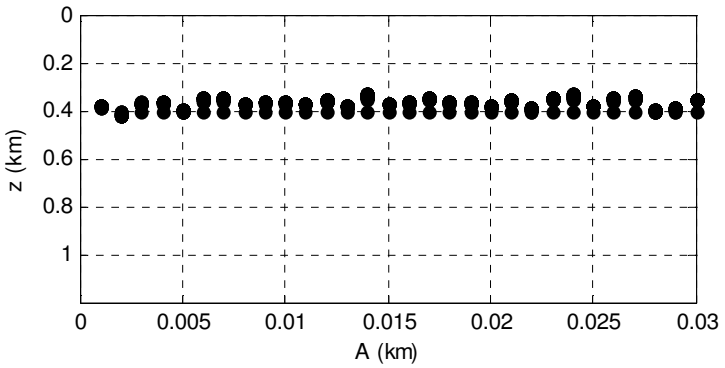

Figure 6-14: Bifurcation diagram, $z = f(A)$. $R = 1km, SNR_A = 25dB$

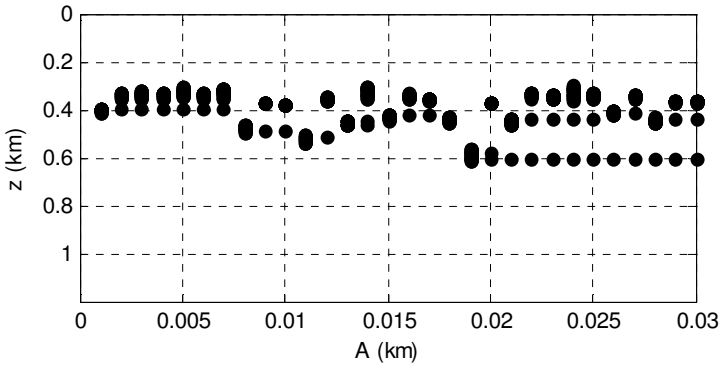

Figure 6-15: Bifurcation diagram, $z = f(A)$. $R = 1km, SNR_A = 15dB$

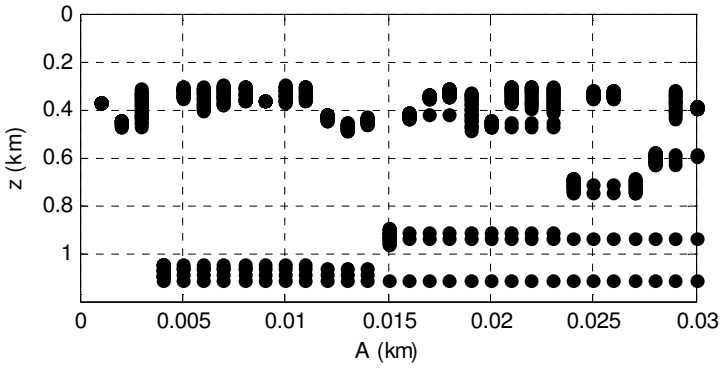

Figure 6-16: Bifurcation diagram, $z = f(A)$. $R = 1km, SNR_A = 5dB$

The bifurcation diagrams for non-perturbed media at a fixed wavelength of $R = 11.2km$, and compared to those the addition of GWN, (SNR_A = 2dB, 25dB, 50dB). It is seen that stability is again replaced with highly unstable behavior as amplitude increases, although still remains stable for small values of amplitude.

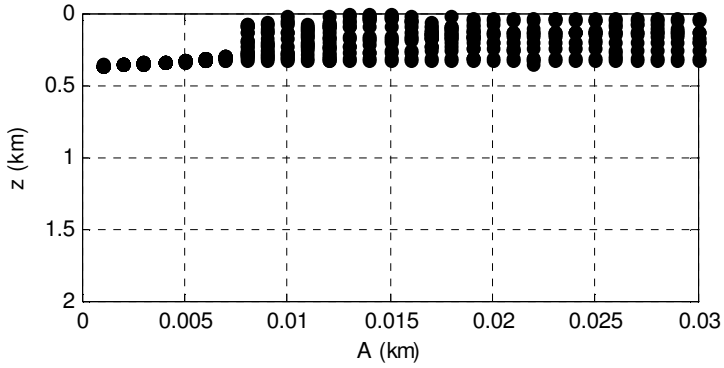

Figure 6-17: Bifurcation diagram, $z = f(A)$. $R = 11.2km$**, no noise.**

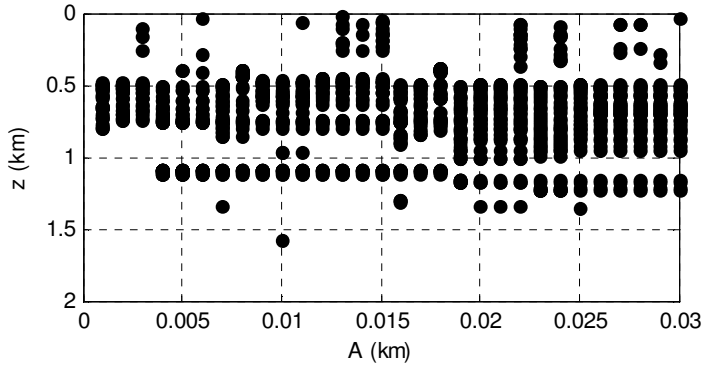

Figure 6-18: Bifurcation diagram, $z = f(A)$. $R = 11.2km, SNR_A = 25dB$

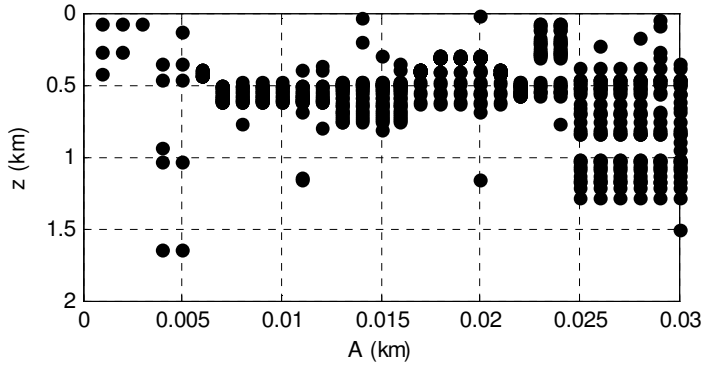

Figure 6-19: Bifurcation diagram, $z = f(A)$. $R = 11.2km, SNR_A = 15dB$

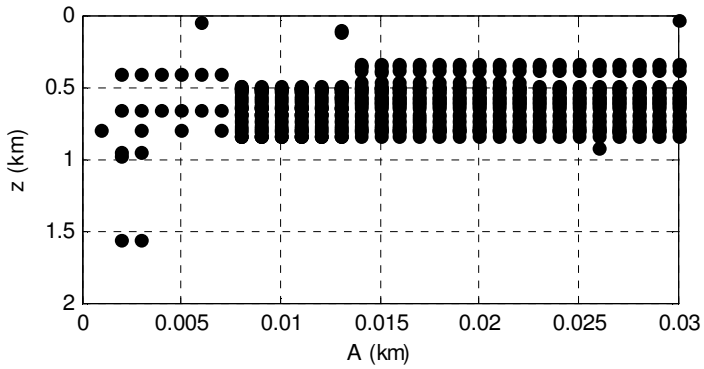

Figure 6-20: Bifurcation diagram, $z = f(A)$**.** $R = 11.2km, SNR_A = 5dB$

Further analysis of the behavior is seen through phase diagrams constructed for A=0.005km and R=11.2km. In Figure 6-21, the phase plane on the right is a simulation with no deterministic effects. Again quasi-periodic behavior is observed indicative of a ray that remains trapped in the sound channel. The phase plane on the right however, includes the deterministic effects and appears distorted in comparison, suggesting highly chaotic behavior. The overlapping and windings again suggests presence of caustics.

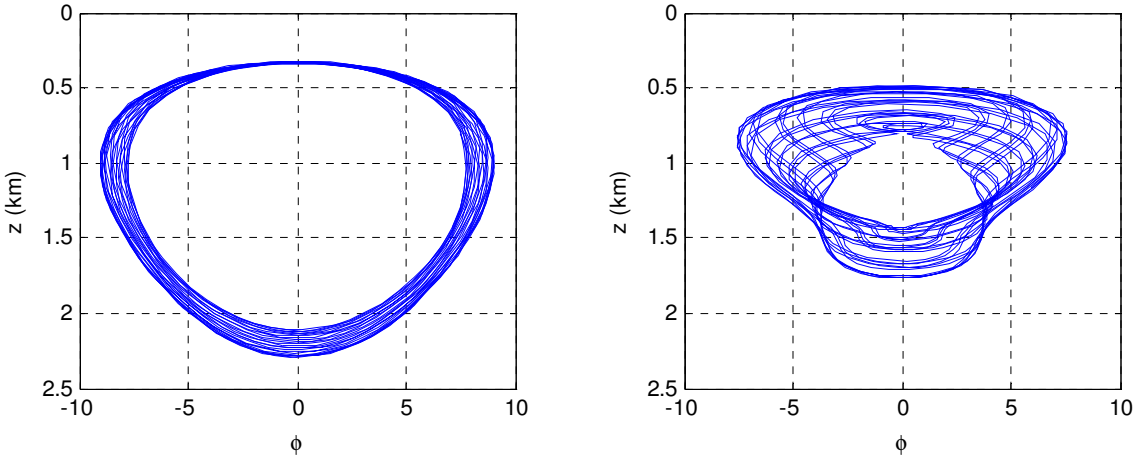

Figure 6-21: Phase Plane. $A = 0.005km, R = 11.2km$**. LEFT: no noise. RIGHT:** $SNR_A = 25dB$**.**

6.1.3 *Bifurcation Analysis with noise in both Amplitude and Wavelength*

The effects of adding noise to both the internal wave wavelength and internal wave amplitude for a propagation range of 1000km are shown in Figure 6-22, the bifurcation plot with a GWN of SNR=25dB. The behavior is extremely erratic. Surface intersection begins almost immediately and rays quickly diverge making ray behavior becomes highly problematic.

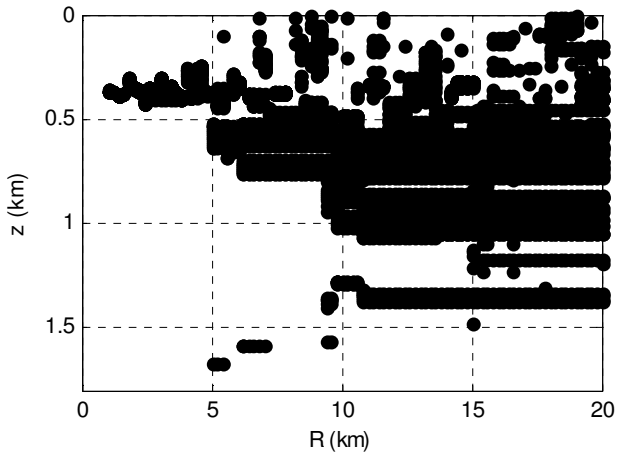

Figure 6-22: Bifurcation Diagram, $z = f(R)$. $A = 0.005km, SNR_R = 25dB, SNR_A = 25dB$

6.2 Poincaré Maps

The instabilities observed in the previous section can also been seen in Poincaré sections. Strictly speaking, the Poincaré section technique is not applicable for an environment with non-constant internal wave frequency, which we are studying. However, the KAM theorem states that chaos features will be preserved but appear distorted, for bounded integrable Hamiltonian systems (Wiercigroch *et al*., 1999). A system of this nature will show extreme sensitivity to small random perturbations. Poincaré sections are constructed using $A = 0.005$ km and two different values of wavelength, R = 1km, and 8.2km, with GWN imposed on the amplitude of the internal waves with SNR = 15dB. The initial launch angle is varied from $7^\circ \le \phi \le 15^\circ$ with $\Delta\varphi = 0.2$, with a total computational range of 1000km.

Figure 6-23 shows a set of Poincaré sections computed for *R*=1km. When no noise is added the all rays fall on smooth, closed curves. With an SNR_A = 15dB, well-organized lines become somewhat distorted and overlap as a result of the imposed random modulations.

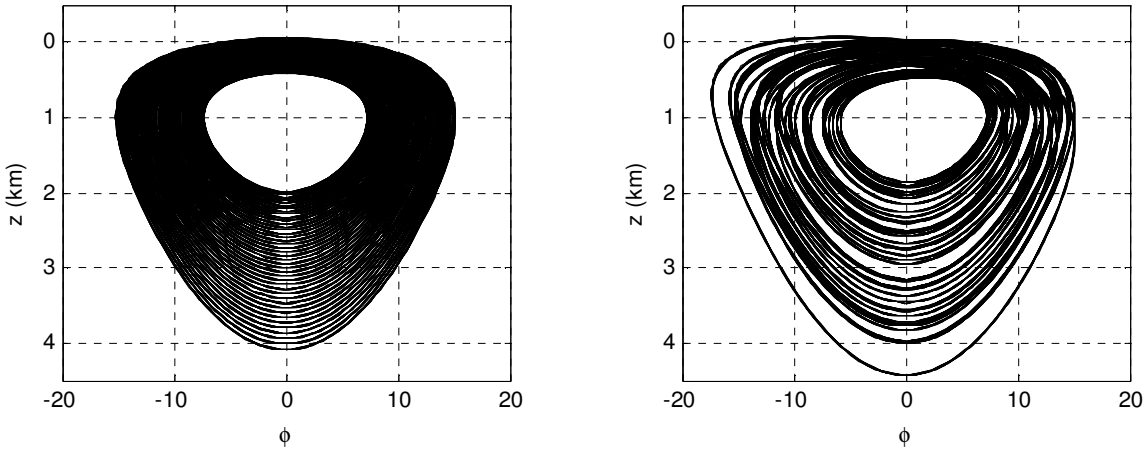

Figure 6-23: Poincaré Map. A=0.005km, R=1km. LEFT: no noise. RIGHT: $SNR_A = 15dB$ **.**

The next choice of a wavelength comes from an exact location of a large spike on the bifurcation diagram *R*=8.2km. In Figure 6-24, for small random modulations smooth curves are observed just as before, which are broken down in the presence of random perturbations. The added noise causes the Poincaré map to take on a completely different form than that with no added noise. The effect of randomness is easier to identify from a bifurcation diagram than from Poincaré section, where the effect of chaos is predominant.

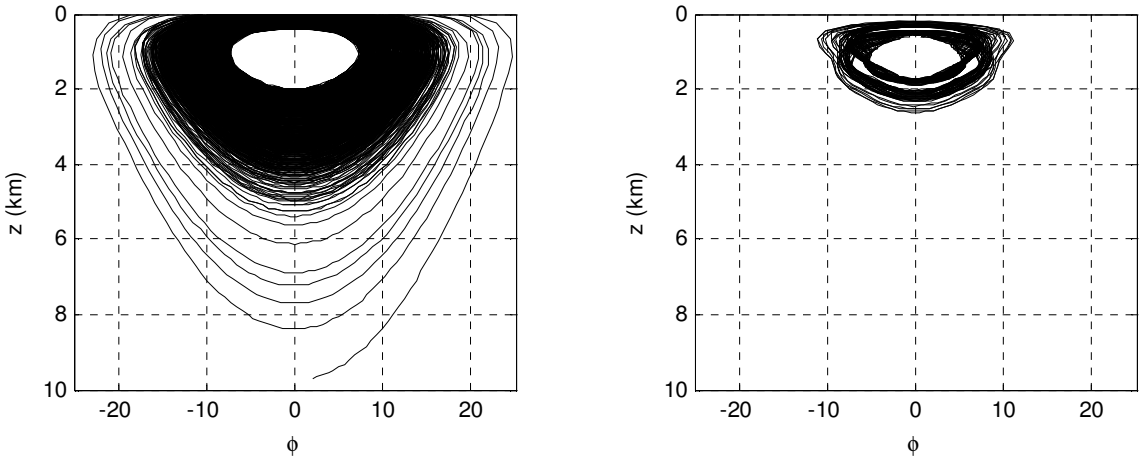

Figure 6-24: Poincaré Map. A=0.005km, R=8.2km. LEFT: no noise. RIGHT: $SNR_A = 15dB$ **.**

6.3 Timefront Analysis for long range propagation

Timefronts are the reconstructed arrivals for a single traveling pulse. The timefront plot depicts arrival times and arrival depths that correspond to uniformly incremented ray launch angles at the source, forming an envelope of expected behavior. The timefront and phase plot for an internal wave that has thus far exhibited steady stable behavior, *A*=0.005km, *R*=1km is observed. The launch angle is varied on the interval $-10^\circ \le \phi(0) \le 10^\circ$. The arrival behavior with and without the effects of the randomly perturbed phase are observed. In Figure 6-25, the timefronts as a function of depth take on an accordion pattern; this is illustrated by the overlapping lines that better define the arrival envelope. The early arriving timefront segments are well distinguished and the smearing of the branches appears in the rear of the pulse, typical behavior of a timefront plot.

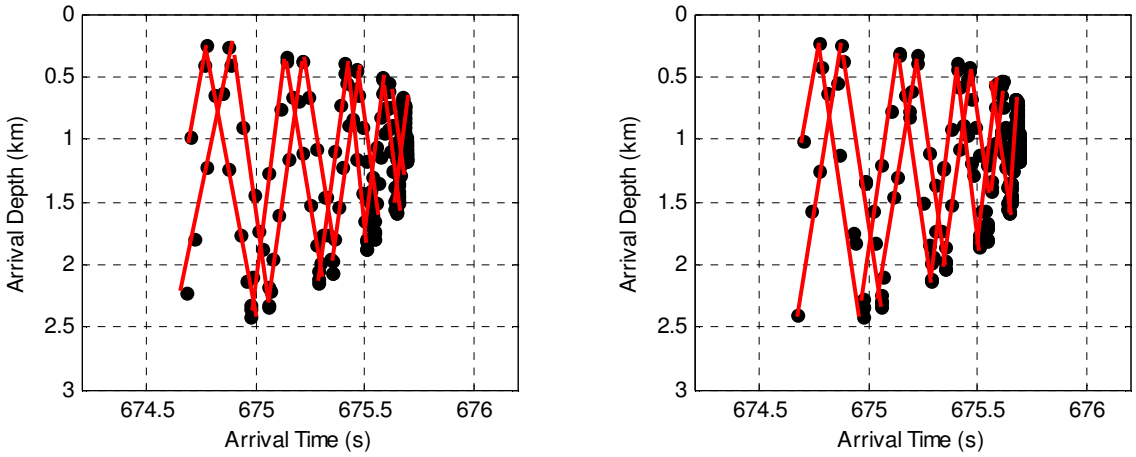

Figure 6-25: Timefront Plot, *A*=0.005km, *R*=1km. LEFT: no noise. RIGHT: $SNR_R = 40dB$**.**

The phase diagram, Figure 6-26, is a scatter plot of p versus z for a fixed propagation range of 1000km. This plot is very useful in detecting folds or caustics on the timefront, those points on the phase curve that have a horizontal tangent, $dz/dp = 0$ (Simmen *et al.*, 1997). A spiral shape is formed around p = 0, when no noise is added. This shape continues to remain intact with the addition of GWN. Again an internal wave of these parameters remains stable and does not exhibit any chaotic behavior.

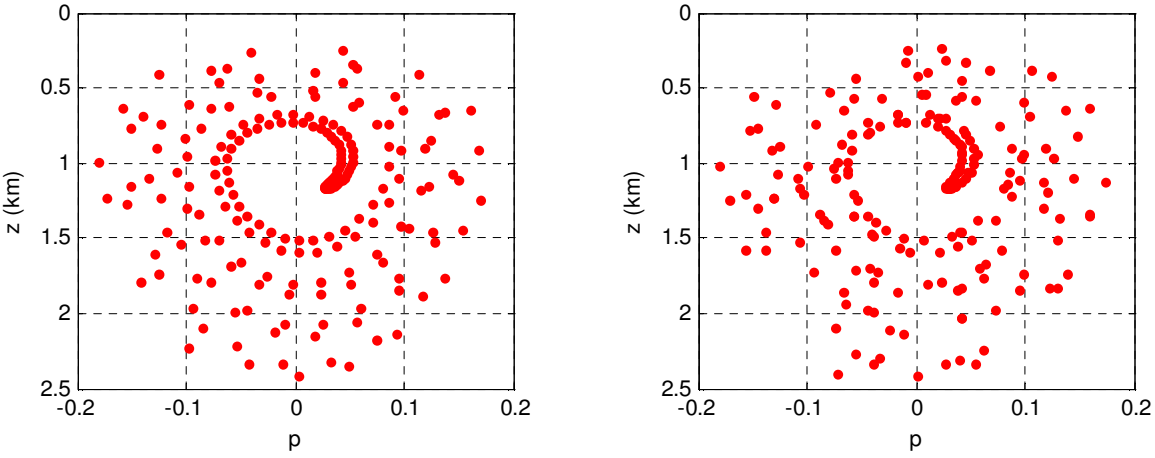

Figure 6-26: Phase Plot, *A*=0.005km, *R*=1km. LEFT: no noise. RIGHT: $SNR_R = 40dB$**.**

The next set of timefront plots corresponds to an internal wave that has shown by previous analysis to cause chaotic behavior, *A*=0.005km, *R*=8.2km. The timefront plot to

the left in Figure 6-27 is that with no added noise. This timefront predicts an arrival envelope ranging from $674.58s \le \tau \le 675.7s$, that similar to that predicted behavior for an internal wave of wavelength R=1km. When GWN is added to the phase we observe much different behavior. The envelope now has a range of $674.45s \le \tau \le 676s$. These arrivals were not accounted for in the previous simulations, which would lead a great deal of inaccuracy in critical communication applications.

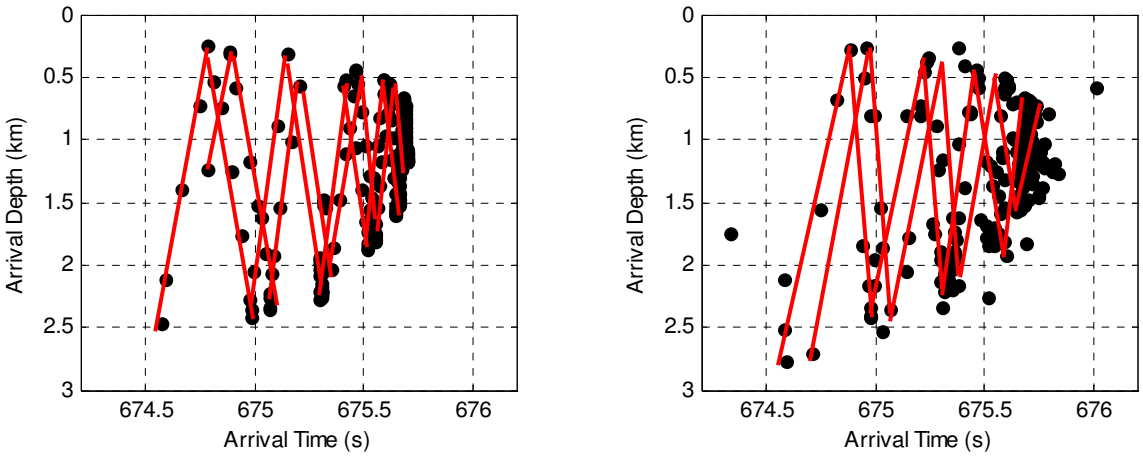

Figure 6-27: Timefront Plot, A=0.005km, R=8.2km. LEFT: no noise. RIGHT: $SNR_R = 40dB$.

The corresponding phase plots shown in Figure 6-28 indicate the presence of chaotic behavior. The smooth spiral curves are again observed when no noise is added, however with the addition of the stochastic parameters, the spiral is replaced by windings, folds, and overlapping, indicating no clear structure. This is consistent with the conclusions from previous sections, an internal wave of wavelength R=8.2km exhibits chaotic behavior.

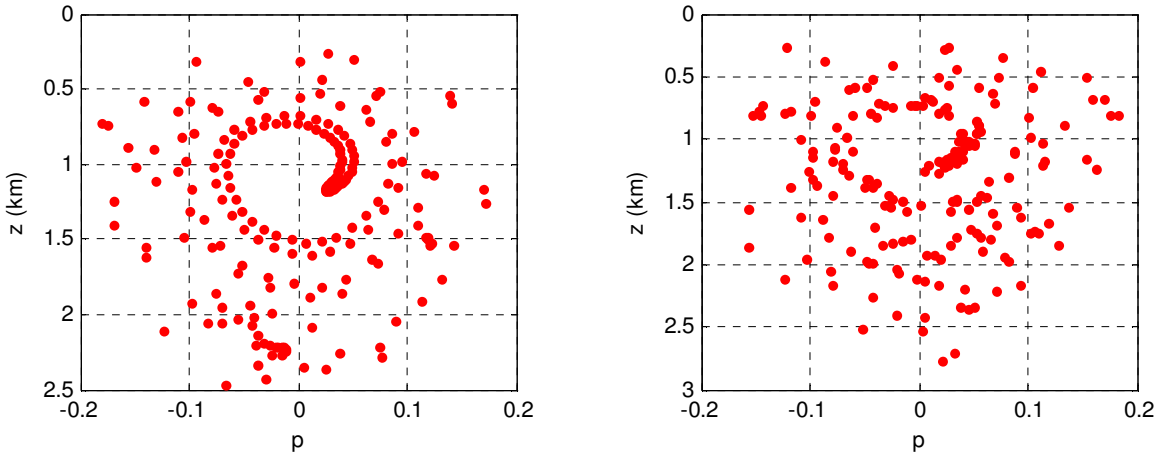

Figure 6-28: Phase Plot, *A*=0.005km, *R*=8.2km. LEFT: no noise. RIGHT: $SNR_R = 40dB$.

6.4 Maximum Ray Propagation Range

The primary objective of ocean acoustic propagation applications is to identify conditions that support long and undisturbed sound propagation. It is well-known by observations in the real ocean that neglecting the internal waves leads to underestimation of the effect of scattered rays. Here specific values of the wavelength and amplitude from the bifurcation diagrams are chosen and diagrams are constructed that define the maximum range that a sound ray propagates before intersecting the ocean surface for internal waves with a added GWN (SNR_R = 15dB) to the phase and no added noise. Figure 6-29, illustrates the maximum range propagation studied as a function of amplitude A for a fixed wavelength $R = 3km$. The maximum value of amplitude was chosen out of mathematical interest. The sound ray channeling is quite effective in this parameter range, none of the rays reach the ocean surface even in the presence of noise.

Next, ray propagation as a function of the wavelength is examined, where $A = 0.005km$ and GWN intensities are identical to those used for Figure 6-29. Here the addition of noise predicts increasing ray divergence to the ocean surface, behavior consistent with the corresponding bifurcation diagrams, *z=f(R)*. Figure 6-30, reveals that in the presence of random noise, the intersection of acoustic rays with the ocean surface occurs sooner and becomes more frequent than predicted by the ray chaos models.

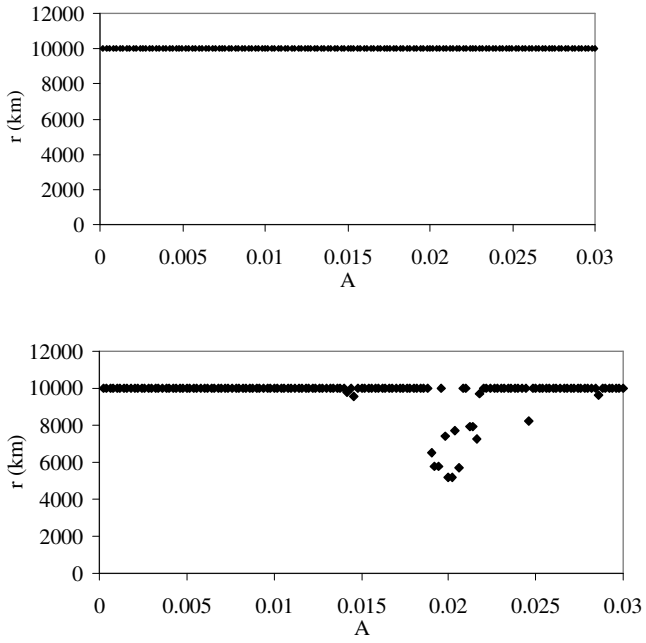

Figure 6-29: Maximum Range Propagation, $r = g(A)$. TOP: *R*=3km, no noise. BOTTOM: *R*=3km, $SNR_R = 15dB$.

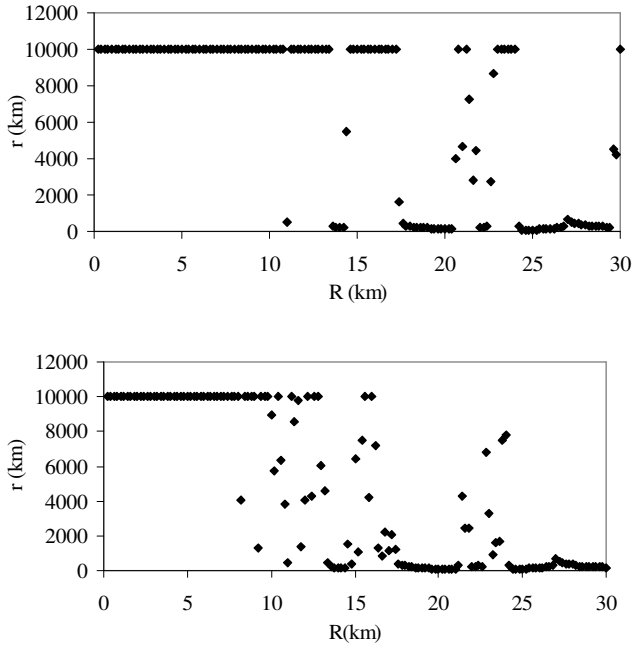

Figure 6-30: Maximum Range Propagation, $r = g(R)$. TOP: *A*=0.005km, no noise. BOTTOM: *A*=0.005km, $SNR_R = 15dB$.

PART II

Short Range Propagation

An acoustic wave carries some structural information regarding the turbulent medium. It is possible to use the behavior of the acoustic wave during its interaction with the turbulence as a diagnostic tool to obtain some statistical information about the medium, (Andreeva, 2003). Part II is organized as follows; first, the simulated turbulence model is justified through comparison with experimentally measured ocean turbulent velocity data, this is followed with analysis of the statistics of the arrival times and depths for a series of simulation experiments for various strengths of the perturbation fields and for varying initial launch angle.

6.5 Comparison of Measured and Simulated Turbulence

The strategy used here is to populate the fluid with a finite number of two-dimensional vortices of random strengths and of random locations. Location is chosen to be within the region of the sound channel axis and specified range of propagation. The eddy dimensions, r_{vortex} and $v_{\theta_{vortex}}$, are necessary for calculating the circulation values. The eddy radius, r_{vortex}, is chosen to be typical to the defined length scales of inertial and lower portion of the energy containing subrange and average circulations values for eddies of this size are a few cm^2/s, the eddy velocity $v_{\theta_{vortex}}$ is thereby chosen accordingly, (NOAA, 1997). The range of these values is listed in Table 6-1. The acoustic ray propagates through the induced velocity field of the vortices and is therefore affected by the "turbulence" generated by the vortices. It is the intension here to represent the ocean as realistically and accurately as possible, therefore comparison of simulation to those of experimentally measured velocities is necessary. D'Asaro and Lien (2000), took measurements in August and September of 1995, of the *u* and *v* induced fluctuating velocities from turbulence in the Knight Inlet in British Columbia, using a Lagrangian method. A Lagrangian method is neither strictly spatial nor temporal, but retains properties of both. The inlet is 100 km long, 3 km wide, and is strongly stratified by freshwater from the Klinaklini and contains a large amount of stratified turbulence comparable to the mixed turbulence found in the thermocline of the ocean (D'Asaro & Lien, 2000). This study does also consider measurements of turbulence from the

thermocline from the northeast Pacific Ocean taken in February 1993 and 1995 to serve as a comparison between the stratified and mixed layer turbulence (D'Asaro & Lien, 2000). Figure 6-31 illustrates spectrum of the *u* and *v* velocity components in the frequency domain for the 29 measurement trajectories; each color corresponds to the flow region where the data was measured. This spectrum peaks at an energy on the order of $10^0 m^2 s^{-1}$ and the majority of activity pertains to a frequency range on the order of $10^{-3} s^{-1} \le \omega \le 10^{-1} s^{-1}$. The ω seen here is identical to our frequency variable *f*.

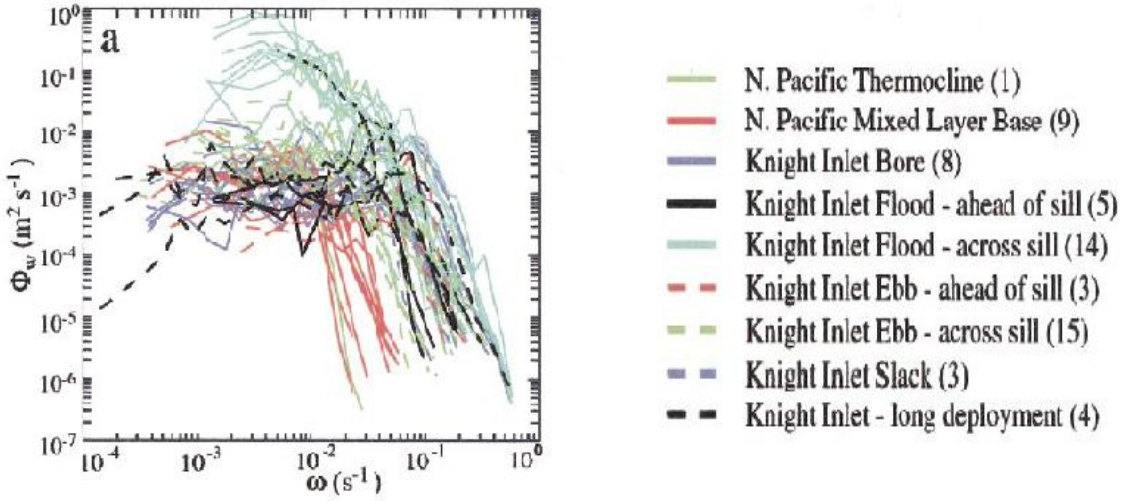

Figure 6-31: Energy spectrum of the *u* and *v* fluctuating velocity components measured from the Knight Inlet (D'Asaro & Lien, 2000).

From this spectrum, two simple idealized shapes can be formed. Figure 6-32, on the left depicts a shape that is at first flat and constant and is then followed by a steep drop off; this is consistent for the turbulence measured in the inlet flow. Thermocline velocities produce a smoother decreasing curve, seen on the right in Figure 6-32. These idealized shapes are used as comparison for the simulated spectra, which is taken in the wavenumber domain. This comparison is appropriate because the flow is considered homogenous and as mentioned earlier, spectra for homogeneous turbulent flow is identical in the spatial and temporal domains (Tennekes & Lumley, 1972). The measured velocities are again Lagrangian, and therefore their spectra would exhibit similar properties in wavenumber space.

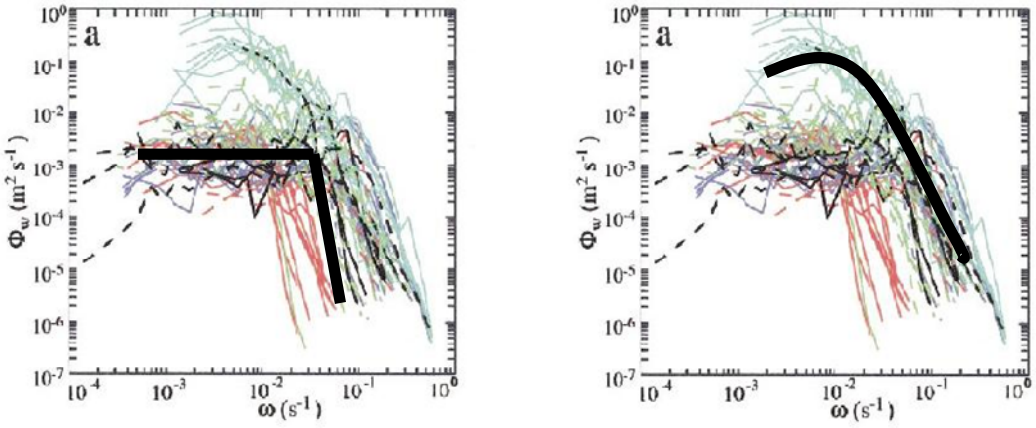

Figure 6-32: LEFT: Shape of flows in inlets. RIGHT: Shape of flows in Thermocline.

The simulated turbulence is constructed over a propagation distance of 10km. The flow is observed over 30 realizations, each realization corresponding to 10s of geophysical time for a total sample 300s. Each vortex is conducted with the ambient current taken as $U_\infty = 0.0005\,km/s$, and is considered "frozen" during the passage of the sound pulse, since the propagation time of the acoustic pulse is short compared to the fluid motion (Weber, 2003). The velocity at any point, P, will vary in time. The perturbation strength of the eddy field is the ratio of the average r.m.s. value of the *u* velocity to the ambient flow velocity, this strength should be typically about 10%. The number and strengths of the vortices are adjusted to results in turbulence intensity of about 10% and to produce spectra similar to those of Figure 6-31. Thus a relatively small number of relatively large turbulent eddies will provide perturbations to the ray propagation. Flows containing three different eddy densities, 10, 25, and 50 eddies, are observed to ensure an accurate representation.

$$\mathrm{X} = \left(\frac{\sqrt{\sigma^2}}{U_\infty} \right) \cdot 100\% \qquad \textbf{(6-1)}$$

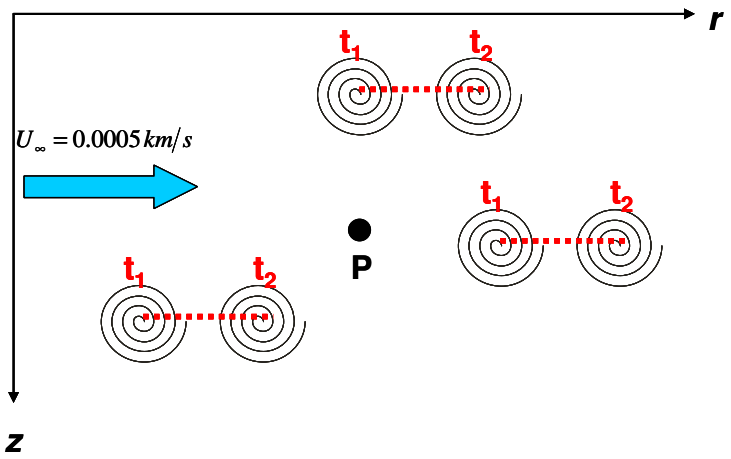

Figure 6-33: Schematic of turbulence simulation.

Table 6-1: Parameter Range for Simulated Vortices.

Parameter Range
$0km \le r_{vortex} \le 1km$
$0km/s \le V \le 1 \cdot 10^{-7}\,km/s$
$0km \le r \le 10km$
$0km \le z \le 1.2km$

Flow containing 10 Eddies

A total of 10 eddies are randomly scattered throughout the propagation region, these locations are plotted in Figure 6-34 and the corresponding circulation strengths are listed in Table 6-2.

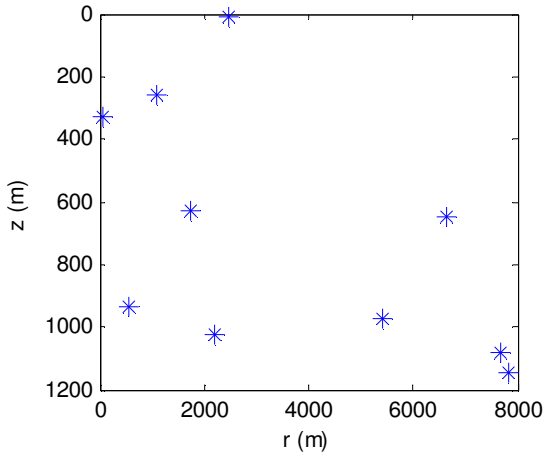

Figure 6-34: Turbulence Field containing 10 eddies.

Table 6-2: Circulation strength and location for Turbulence Field containing 10 eddies.

$\Gamma(km^2 s^{-1})$	r-position (km)	z-position (km)
-9.38E-06	7.03252	0.441611
-3.78E-06	9.19907	0.230152
-5.65E-04	8.66496	0.636222
-4.67E-06	2.88692	0.088144
6.43E-05	3.7263	0.409006
3.68E-06	6.95627	0.420295
2.56E-07	5.86964	1.14785
-1.63E-06	1.60811	0.106107
8.66E-07	4.30014	0.294673
-1.34E-07	6.03027	0.96586

The spatial locations (1000m, 800m), (5000m, 800m), and (7000m, 800m) are chosen as stationary points at which to observe the *u* and *v* induced velocities over time in order to gain an indication of the flow activity. Figure 6-35 shows the *u* and *v* fluctuating velocities over 300s. The intensity of perturbation strength is $X = 2.0\%$, which is lower than that desired to represent the turbulence. Since the vortex population is sparse, there are long times of minimal fluctuation. The fluctuation is dependent on the eddy location. The velocity observed at the point (5000m, 800m) shows fluctuation at about 200s, behavior not seen for other two points in the flow. The spectra of the *u* and *v* velocities are taken as a function of range at fixed time (realization). Such flows in the ocean are known to be quasi-homogenous; we will thereby use the assumption that spectra are comparable to those of Figure 6-31. Each realization is indicated by a different color.

The shape is consistent with that of the measured turbulence, so the vortex representation is accurate however the density of perturbations is not.

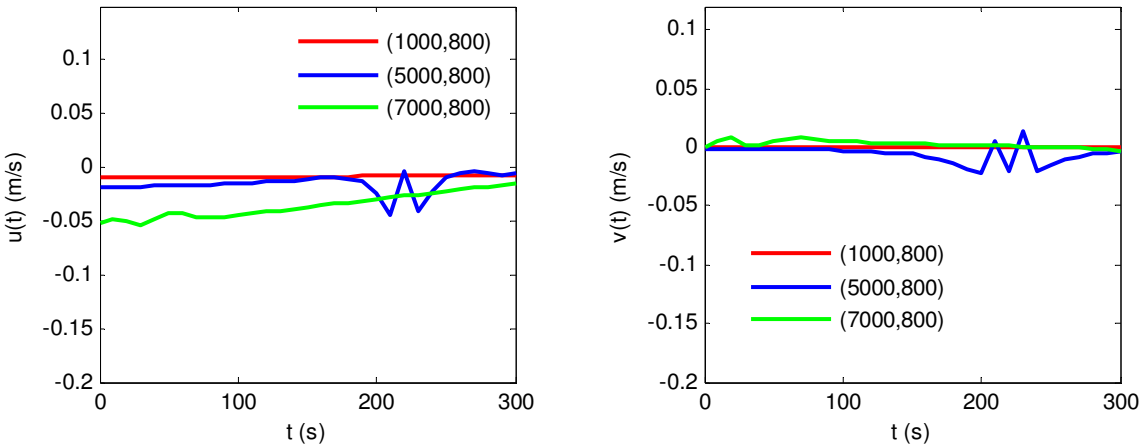

Figure 6-35: Flow containing 10 eddies. LEFT: *u*-velocity over time. RIGHT: *v*-velocity over time.

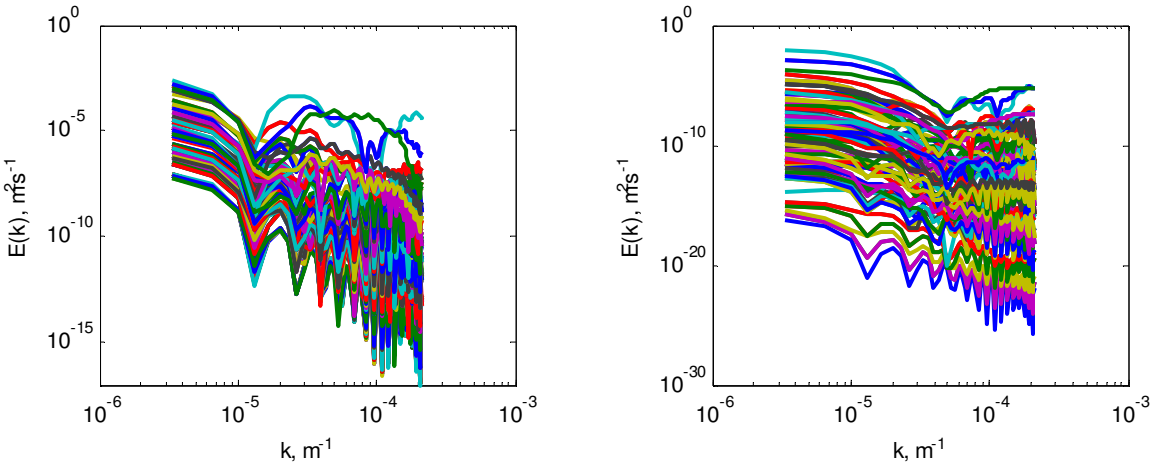

Figure 6-36: Flow containing 10 eddies. LEFT: *u*-velocity frequency spectra. RIGHT: *v*-velocity frequency spectra.

Flow containing 25 Eddies

The density of eddies within the flow is now increased to 25 eddies, which yields a perturbation strength of $X = 4.9\%$. The 25 eddies are randomly assembled throughout the propagation region, this field is seen in Figure 6-37. The randomly assigned circulation values for each vortex are listed in Table 6-3.

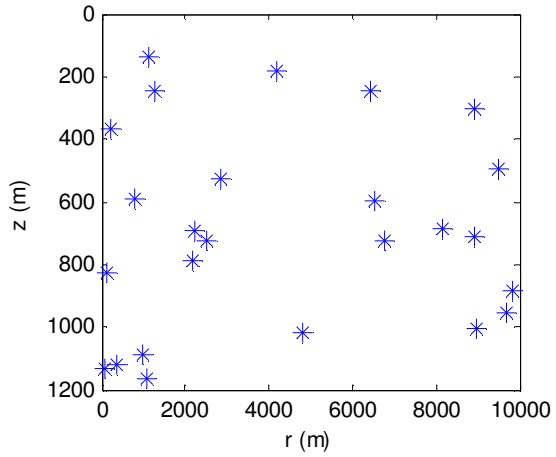

Figure 6-37: Turbulence Field containing 25 eddies.

Table 6-3: Circulation strength and location for Turbulence Field containing 25 eddies.

$\Gamma(km^2 s^{-1})$	r-position (km)	z-position (km)
6.69E-10	2.24733	0.694646
-3.69E-07	2.53315	0.725911
3.25E-08	0.957711	1.08894
-5.64E-10	6.74741	0.727547
-8.81E-09	9.84675	0.883836
3.91E-08	9.4987	0.491965
-4.95E-07	2.82324	0.524772
6.19E-08	1.10202	0.137686
-4.05E-09	8.14338	0.684888
6.34E-08	1.07039	1.16602
-2.81E-08	8.92655	0.708612
-5.04E-07	6.54845	0.595615
8.82E-09	6.45288	0.247684
-3.39E-06	0.115	0.824149
2.37E-07	9.70771	0.95581
3.27E-09	2.18262	0.791318
3.41E-06	0.060963	1.13059
-1.96E-08	0.372102	1.12132
1.83E-06	8.92774	0.306232
5.49E-09	1.26893	0.245443
3.72E-04	0.210988	0.368957
-1.91E-06	8.96284	1.00556
-5.68E-08	4.19101	0.181769
3.33E-08	0.781229	0.589162
2.09E-10	4.78803	1.01613

The same locations (1000m, 800m), (5000m, 800m), and (7000m, 800m) are observed over time. This increase in perturbation strength did not produce more consistent fluctuation in the *u* and *v* induced velocities as was expected. This is because of the random placement of the vortices in the field, there is not a strong enough eddy density for the induced velocities to be observed everywhere in the flow. Increased eddy density will induce more consistent fluctuation. The spectra again taken of *u* and *v* velocities over range for each realization are indicated by a different color, and are in good agreement with the shape of the measured turbulence.

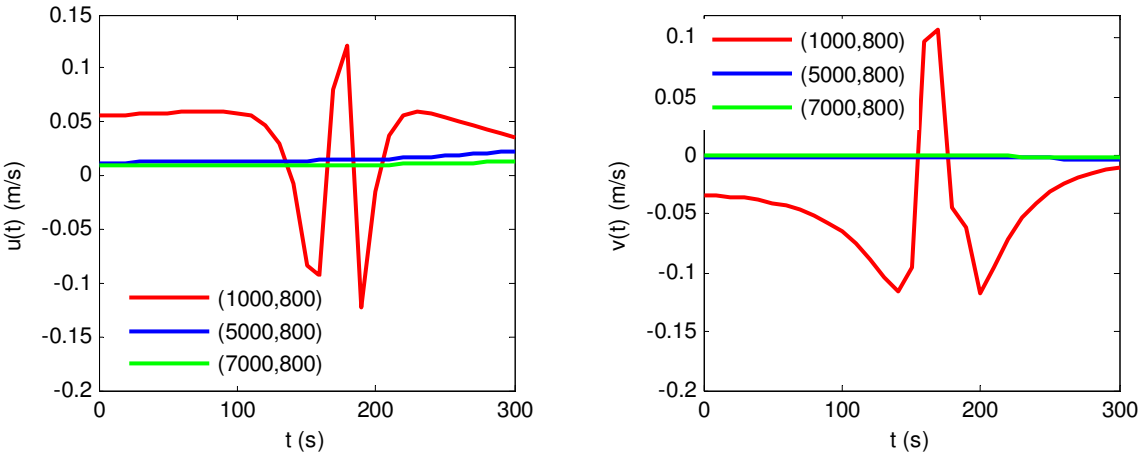

Figure 6-38: Flow containing 25 eddies. LEFT: *u*-velocity over time. RIGHT: *v*-velocity over time.

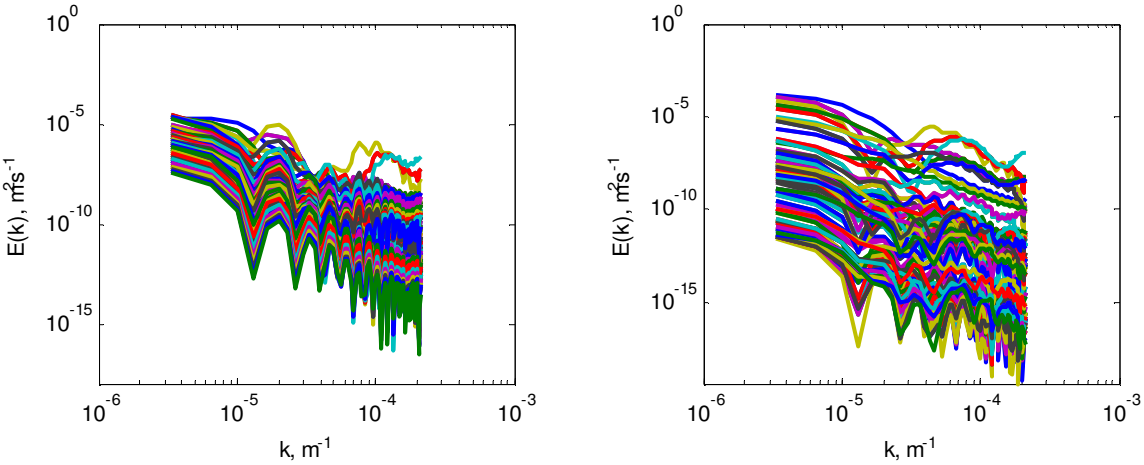

Figure 6-39: Flow containing 25 eddies. LEFT: *u*-velocity frequency spectra. RIGHT: *v*-velocity frequency spectra.

Flow containing 50 Eddies

A flow containing 50 eddies increases the perturbation strength to $X = 10\%$, comparable to typically naturally occurring flows. Figure 6-40 illustrates the location of eddies throughout the flow section and their respective circulation strengths are listed in Table 6-4.

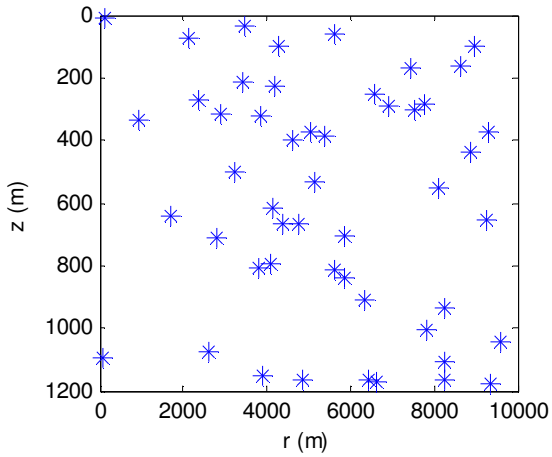

Figure 6-40: Turbulence Field containing 50 eddies.

Table 6-4: Circulation strength and location for Turbulence Field containing 50 eddies.

$\Gamma(km^2 s^{-1})$	r-position (km)	z-position (km)
-2.62E-05	8.89376	0.437971
2.51E-05	9.31905	0.372959
-2.62E-05	4.59964	0.396071
2.49E-05	8.1282	0.551866
-7.78E-06	6.58178	0.249623
1.64E-06	2.81189	0.713916
-1.99E-07	2.6085	1.07647
2.12E-05	6.34025	0.911656
5.19E-06	5.04038	0.371158
2.07E-05	5.86188	0.838776
-2.19E-06	3.4028	0.216849
2.47E-07	9.25998	0.656929
1.78E-05	9.36352	1.17881
3.94E-06	5.87009	0.707009
1.31E-05	7.76973	0.283996
2.90E-05	2.36892	0.268194
1.79E-05	7.42714	0.169194
2.51E-05	4.27532	0.096883
-5.36E-07	7.801	1.00592
3.81E-05	1.71944	0.643395

Table 6-4: Circulation strength and location for Turbulence Field containing 50 eddies., continued.

$\Gamma(km^2 s^{-1})$	**r-position (km)**	**z-position (km)**
3.92E-05	8.24598	0.933397
1.51E-05	0.139397	0.011414
1.01E-05	4.73764	0.667456
4.63E-05	3.24629	0.502778
1.73E-05	5.38826	0.385981
3.82E-05	3.9184	1.15279
-9.73E-06	0.093891	1.0971
1.00E-05	4.10133	0.79152
1.69E-05	4.86104	1.168
3.70E-05	8.27289	1.11007
1.33E-06	4.14305	0.617231
1.04E-05	3.7805	0.806904
5.31E-06	2.1107	0.072193
3.26E-05	8.98065	0.100279
-5.14E-06	8.64419	0.164649
2.99E-05	3.45154	0.036658
-5.77E-06	6.64829	1.17316
1.67E-05	5.61357	0.814758
3.08E-06	3.86717	0.323395
4.42E-06	4.39911	0.665679
1.97E-06	4.18457	0.22669
1.55E-05	5.12678	0.534907
-2.50E-05	0.950383	0.334343
1.89E-05	2.9107	0.317068
3.21E-05	6.42827	1.16638
4.09E-05	6.91458	0.288464
5.41E-05	7.55138	0.300823
1.95E-06	5.59841	0.061955
-1.42E-05	8.25327	1.16541
2.59E-05	9.60836	1.04449

Figure 6-41 illustrates consistent fluctuation over time in the *u* and *v* fluctuating velocities at all points within the flow, a typical characteristic for a turbulent flow. The again illustrates accurate representation. This eddy field is of idealized intensity and its spectra follow the form observed for measured thermocline turbulence. It can be thought of as a "large" eddy simulation in two dimensions of the quasi-homogeneous turbulent structure of ocean turbulence. At the very least, it forms a basis for random turbulent

effect on acoustic ray propagation that will induce perturbations to the ray arrivals. This eddy field is used for the remainder of the simulations.

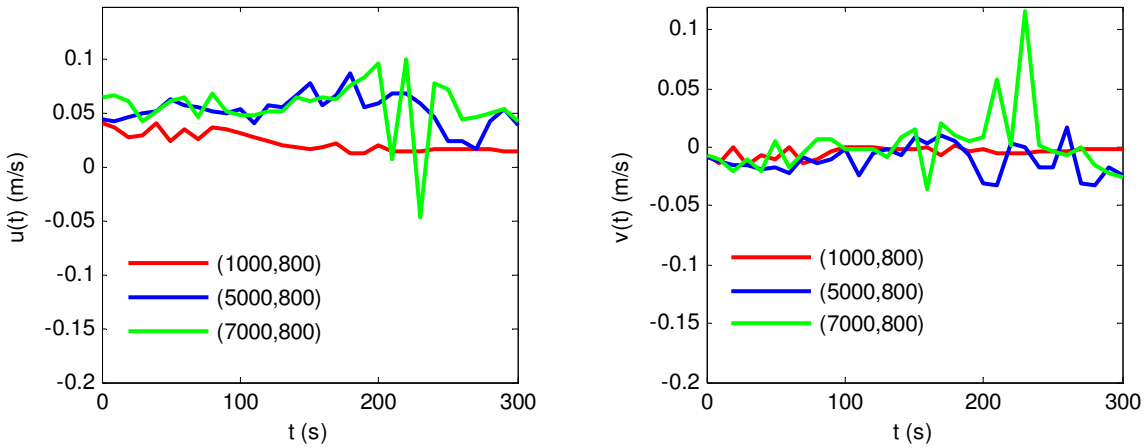

Figure 6-41: Flow containing 50 eddies. LEFT: *u*-velocity over time. RIGHT: *v*-velocity over time.

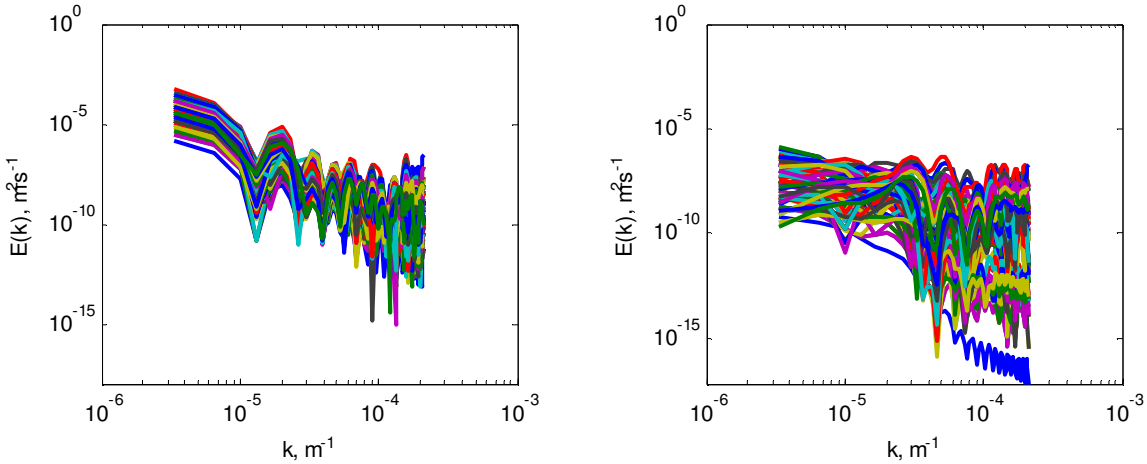

Figure 6-42: Flow containing 50 eddies. LEFT: *u*-velocity frequency spectra. RIGHT: *v*-velocity frequency spectra.

6.6 Propagation through Turbulent Scenarios

Rays with initial launch angles of $\phi(0) = 7.5^{\circ}$ and 0°, are propagated through three perturbation environments: internal waves, turbulence, and both internal waves and turbulence combined. Two cases of internal waves are of interest, an internal wave representing stability and a wave where chaotic behavior is observed, see Table 6-5.

These results were taken from simulations of long range propagation. The same turbulent field analyzed in the previous section is used throughout these simulations; refer to Table 6-6 for location and circulation strengths. The ambient current remains to be $U_{\infty} = 0.0005\, km/s$. The propagation distance is 10km. The flow is observed over 30 realizations, each realization corresponding to 10s of geophysical time for a total sample 300s. The turbulent features are again assumed "frozen." A simulation containing no perturbation fields, only the Munk sound speed profile serves as a baseline for these simulation experiments, as there is no induced fluctuating component. Predicted arrival structures for turbulent scenarios are compared to the baseline simulation though a percent difference relation.

$$\%\text{Difference} = \left(\frac{\left| (\text{turbulent arrival - baseline arrival}) \right|}{\text{baseline arrival}} \right) \times 100\% \qquad \textbf{6-2)}$$

Table 6-5: Internal Wave Parameters for Simulation

	A (km)	R (km)	SNR_R (dB)	SNR_A (dB)
IW (stable)	0.005	1	30	30
IW (chaotic)	0.005	8.2	30	30

6.6.1 *Ray propagation with initial launch angle,* $\phi(0) = 7.5^{\circ}$

This plot illustrates the path a ray takes through an ocean described by Munk's sound speed profile propagating from a source with a launch angle of $\phi(0) = 7.5^{\circ}$, to a receiver array 10km from the source.

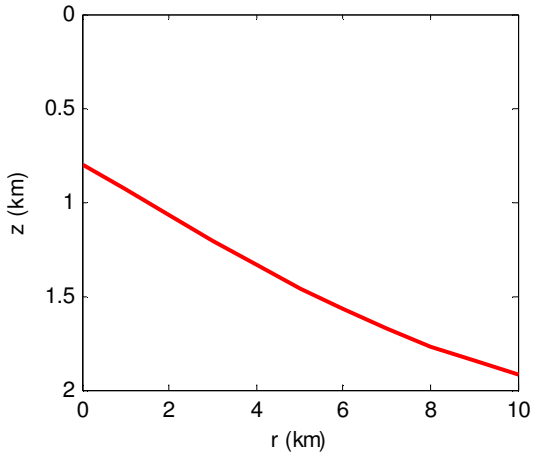

Figure 6-43: Ray Trace, $\phi(0) = 7.5^{\circ}$.

Baseline Simulation: $\phi(0) = 7.5^{\circ}$

A pulse traveling through an ocean containing the canonical sound speed profile only, has a delay of $6.7816 \pm 3.6114 \cdot 10^{-15}\, s$ and a predicted arrival depth of $1.9175 \pm 1.3543 \cdot 10^{-15}\, km$, illustrated by the timefront branch seen in Figure 6-44. The arrival structure has very small deviation from the mean indicating only computational round off error.

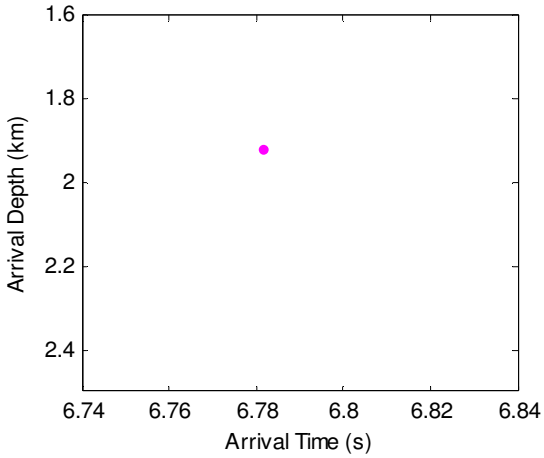

Figure 6-44: Sound Speed, $\phi(0) = 7.5^{\circ}$. Timefront.

Computational error is also seen in the energy-spectra of the pulse fluctuating portion of mean travel velocity (MTV) calculated from the predicted arrival time at 10km, is taken over the timeseries and plotted in Figure 6-45. There is essentially no activity observed.

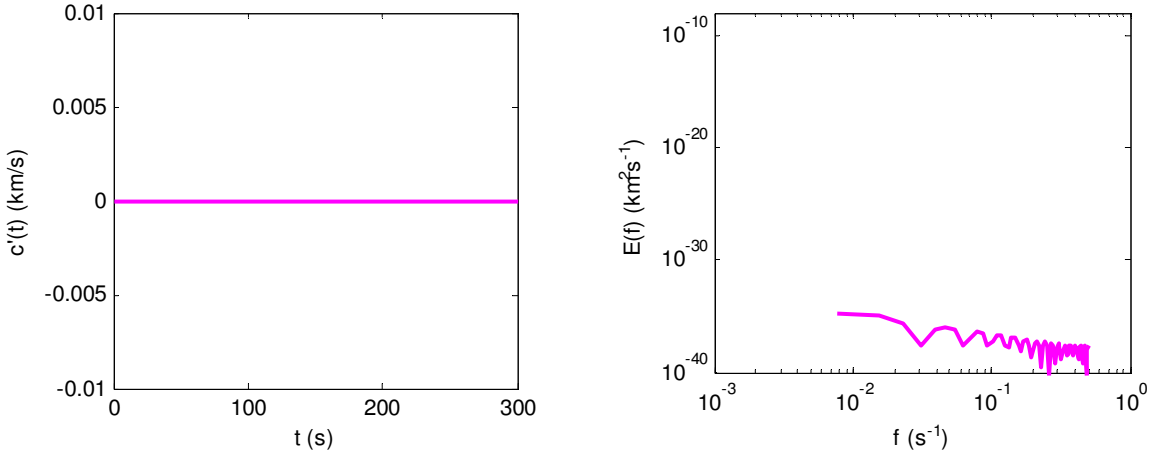

Figure 6-45: Sound Speed, $\phi(0) = 7.5^\circ$. LEFT: Fluctuating MTV. Energy-frequency Spectrum.

SIMULATION 1: $\phi(0) = 7.5^{\circ}$

Propagation through a Stable Internal Wave, a Turbulent Field, and a Stable Internal Wave + Turbulent Field Combined

The results for propagation through the turbulent scenarios are plotted simultaneously for clear observation. The arrival times for each case are plotted in Figure 6-46 as a timefront branch. It is clear that the internal waves are responsible for the path degradation of the pulse, while the eddy field contributes the majority of temporal fluctuations. The dots in red represent the case where both the internal waves and the eddy field were present, and as expected both depth and delay variation are observed. Sound passage through an eddy field yields a delay of $6.7731 \pm 0.0021s$ and arrival depth of $1.9190 \pm 1.0606 \cdot 10^{-4} km$. Transmission through an internal wave field gives an arrival time of $6.7823 \pm 0.0016s$ and depth of $1.9252 \pm 0.0238km$. The average arrival for a pulse through the combination scenario is $6.7739 \pm 0.0028s$ at a depth of $1.9268 \pm 0.0238km$. These results are summarized through the comparison of the percentage difference to the baseline in Table 6-6. Internal waves arrive 0.4016% deeper than the baseline, thereby concluding that internal waves lead to the path variation of the pulse. The turbulent field arrives 0.1253% earlier than the baseline thereby contributing strong delay fluctuations. Propagation through the combination environment illustrates both effects with a 0.1135% earlier arrival and a 0.4850% deeper arrival than that observed in the baseline experiment.

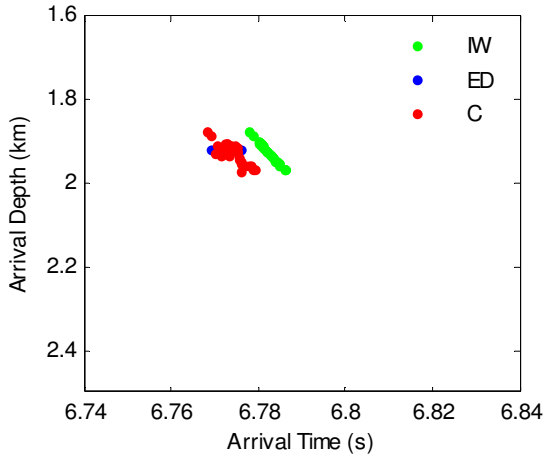

Figure 6-46: Timefront branch for all perturbation scenarios of Simulation 1.

Table 6-6: Summary of arrival predictions for Simulation 1.

	Delay (%)	Depth (%)
Eddy Field	0.1253	0.0782
Internal Waves	0.0103	0.4016
Combination	0.1135	0.4850

The contributions of the fluctuations are easily observed from the timefront plot. However the spectra of the fluctuating MTV observed at 10km over the timeseries for these scenarios are unrevealing. The spectrum for the combination environment takes on the shape of the internal wave spectra, indicting a dominance of internal wave fluctuations; otherwise, the spectra are inconclusive.

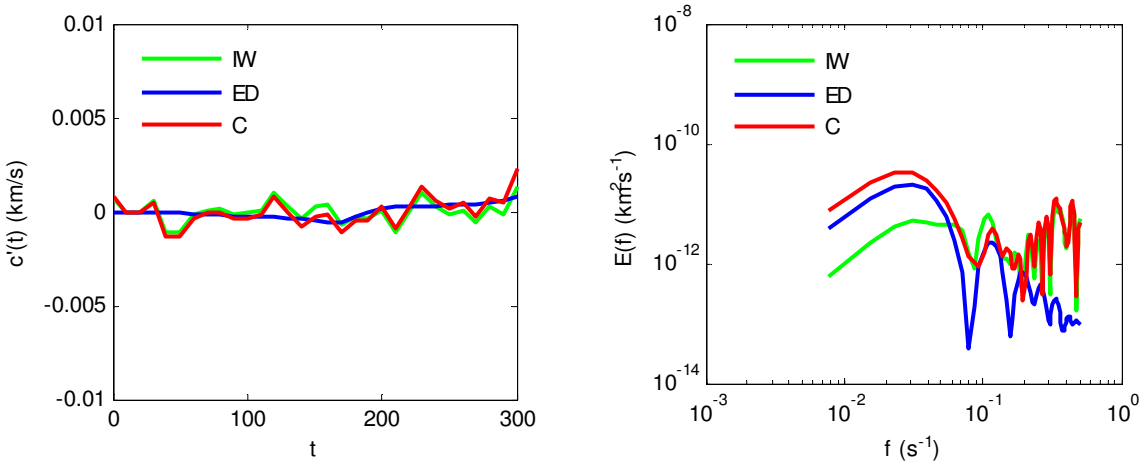

Figure 6-47: Turbulence, $\phi(0) = 7.5^\circ$. LEFT: Fluctuating MTV. Energy-frequency Spectrum.

SIMULATION 2: $\phi(0) = 7.5^{\circ}$

Propagation through a Chaotic Internal Wave, a Turbulent Field, and a Chaotic Internal Wave + Turbulent Field Combined

The results for propagation through the turbulent scenarios are again plotted simultaneously for clear observation. The timefront branch is seen in Figure 6-48. The contributions are clear, internal waves supply a highly variable arrival depth, the turbulent field is responsible for delay instability, and the combination environment hosts both fluctuations. The turbulent field predicts the exact arrival structure as before, since there are no varying parameters for the field. However, transmission through an internal wave field that has demonstrated chaotic behavior gives an arrival time of $6.7863 \pm 0.0173s$ and depth of $1.9556 \pm 0.1721km$, this arrival depth is 1.9870% deeper than the baseline experiment. The combination environment produces a $6.7780 \pm 0.0178s$ delay, 0.0531% earlier than the baseline and arrives at a depth of $1.9571 \pm 0.1723km$, 2.0652% deeper than the baseline, which suggests that the amount of ray path degradation is dependant on the intensity of the internal waves.

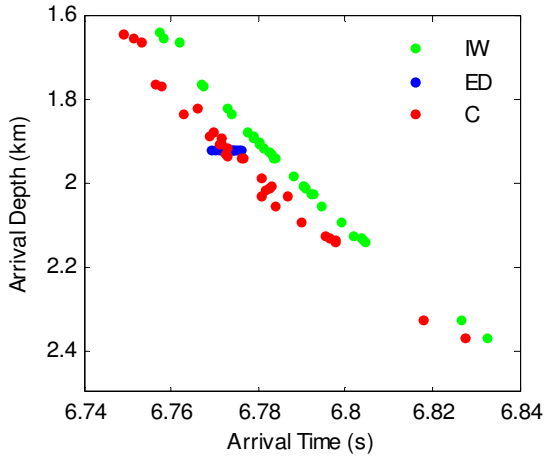

Figure 6-48: Timefront branch for all perturbation scenarios of Simulation 2.

Table 6-7: Summary of arrival predictions for Simulation 2.

	Delay (%)	Depth (%)
Eddy Field	0.1253	0.0782
Internal Waves	0.0693	1.9870
Combination	0.0531	2.0652

The intensity of the internal waves also plays a role in the frequency spectra where it is clear that the combination environment spectrum takes on the shape of the internal wave spectrum. This increase of intensity causes a stronger dominance of the internal wave perturbation in the combination environment spectrum, thereby making any separation of contributions extremely difficult.

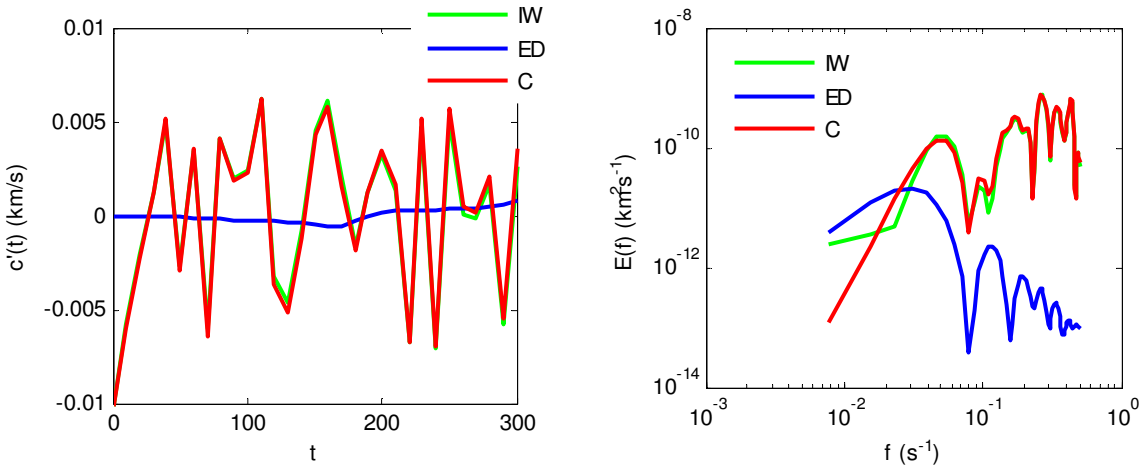

Figure 6-49: Turbulence, $\phi(0) = 7.5^\circ$. LEFT: Fluctuating MTV. Energy-frequency Spectrum.

6.6.2 *Ray propagation with initial launch angle,* $\phi(0) = 0^\circ$

Figure 6-50, depicts a ray with launch angle $\phi(0) = 0^\circ$ transmitting through an ocean described by Munk's sound speed profile over a distance of 10km.

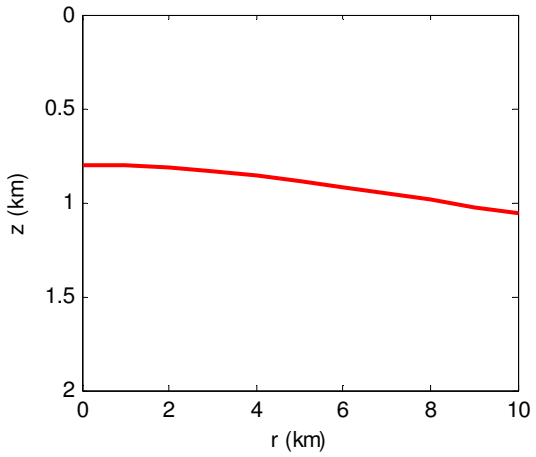

Figure 6-50: Ray Trace, $\phi(0) = 0^\circ$**.**

<u>Baseline Simulation:</u> $\phi(0) = 0^\circ$

The baseline experiment contains no perturbation fields, only the Munk sound speed profile. This pulse has a delay of $6.7578 \pm 3.6114 \cdot 10^{-15}\, s$ and a predicted arrival depth of $1.0616 \pm 2.2572 \cdot 10^{-16}\, km$, see Figure 6-51. The arrival structure again shows only very small deviation from the mean indicating only computational round off error. This predicted arrival behavior is different from that of a pulse leaving an angle of $\phi(0) = 7.5^\circ$. A pulse leaving from the source at $\phi(0) = 0^\circ$ remains trapped in the sound channel and has very little path deviation due to the structure of the sound speed profile, therefore arrives earlier and closer to launch depth.

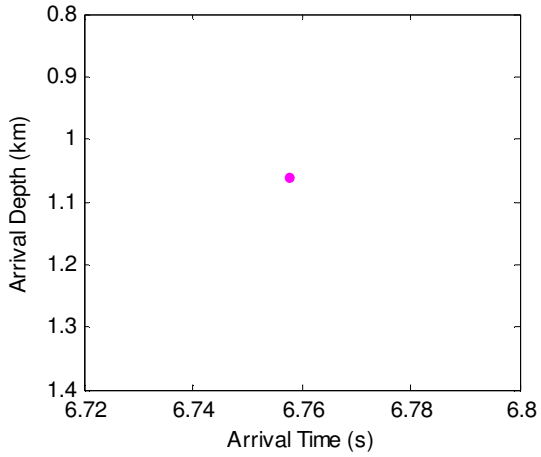

Figure 6-51: Sound Speed, $\phi(0) = 0^\circ$. Timefront.

Computational error is also seen in the energy-spectra of the pulse fluctuating MTV, calculated from the predicted arrival time, no activity is observed, Figure 6-52.

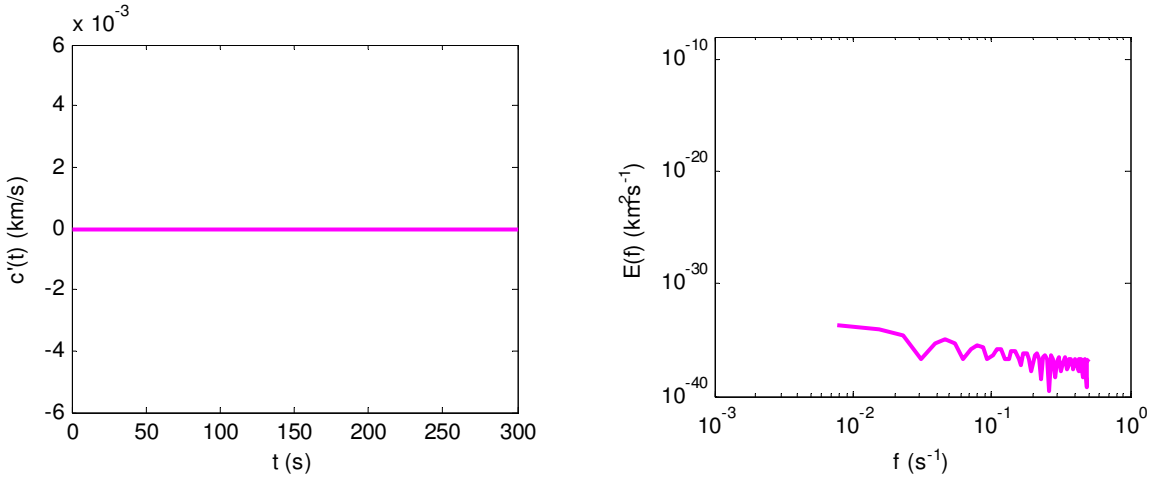

Figure 6-52: Sound Speed, $\phi(0) = 0^\circ$. LEFT: Fluctuating MTV. Energy-frequency Spectrum.

SIMULATION 3: $\phi(0) = 0^\circ$

Propagation through a Chaotic Internal Wave, a Turbulent Field, and a Chaotic Internal Wave + Turbulent Field Combined

The results for propagation through the turbulent scenarios are plotted simultaneously for clear observation. The arrival times for each case are plotted in Figure 6-53. Arrival fluctuations illustrate similar behavior to that seen for a launch angle of $\phi(0) = 7.5^\circ$; internal waves are responsible for the majority of the path degradation, while eddy turbulence primarily contributes to temporal fluctuations. Sound passage through an eddy field yields a delay of $6.7420 \pm 0.0017 s$ and arrival depth of $1.9190 \pm 1.0606 \cdot 10^{-4} km$, a 0.2338% earlier arrival than the baseline simulation. This percentage difference indicates that the eddy field has a stronger affect of delay than previously observed, which can be attributed to the multi-path channeling of the ocean, the pulse is now encountering a larger percentage of eddies than before. This behavior is dependant on the positioning of eddies, for a different field the reverse effect may have been observed, the majority may have been encountered in the latter simulations.

Transmission through an internal wave field gives an arrival time of $6.7580 \pm 2.0062 \cdot 10^{-4} s$ and depth of $1.0649 \pm 0.0170 km$. The arrival depth is 0.3109% deeper than the simulation. The average arrival for a pulse through the combination scenario is $6.7422 \pm 0.0026 s$ at a depth of $1.0639 \pm 0.0171 km$. These predictions compared to the baseline simulation arrival 0.2308% earlier and 0.2167% deeper.

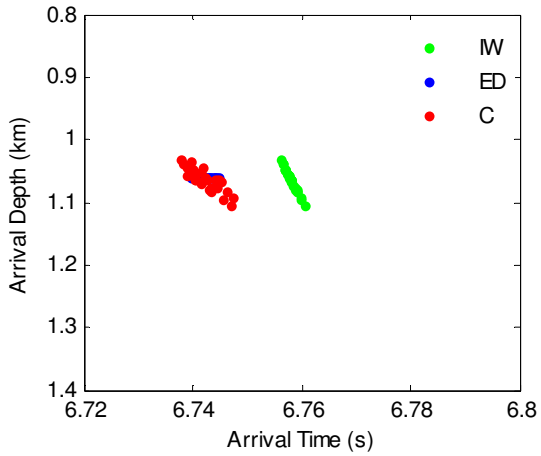

Figure 6-53: Timefront branch for all perturbation scenarios of Simulation 3.

Table 6-8: Summary of arrival predictions for Simulation 3.

	Delay (%)	Depth (%)
Eddy Field	0.2338	0.0942
Internal Waves	0.0030	0.3109
Combination	0.2308	0.2167

The frequency spectra again show the dominance of the internal wave environment, making the separation of the fluctuations a very difficult task. It is thereby more practical to observe the timefront structure of arrival pulse.

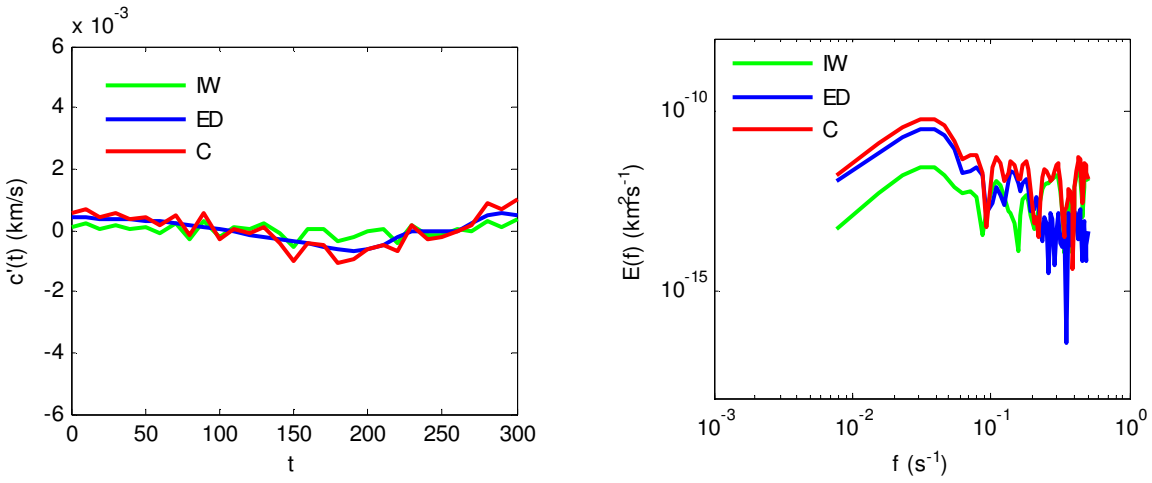

Figure 6-54: Turbulence, $\phi(0) = 0^\circ$. LEFT: Fluctuating MTV. Energy-frequency Spectrum.

SIMULATION 4: $\phi(0) = 0^\circ$

Propagation through a Chaotic Internal Wave, a Turbulent Field, and a Chaotic Internal Wave + Turbulent Field Combined

The arrival structure is plotted Figure 6-48. The contributions are again clear and conclusive, variation in depth in attributed to the internal waves and fluctuation in delay is attributed to turbulent eddies. The eddy field predicts the exact arrival structure as seen in Simulation 3 as there are no varying parameters for the field. However, transmission through an internal wave that has demonstrated chaotic behavior gives an arrival time of $6.7621 \pm 0.0108s$ and depth of $1.1026 \pm 0.1062km$, this arrival depth is 3.8621% deeper than the baseline experiment. The combination environment produces a $6.7467 \pm 0.0127s$ delay, 0.1643% earlier than the baseline and arrives at a depth of $1.1016 \pm 0.1070km$, 3.7679% deeper than the baseline. Based on previous analysis it can thereby be concluded that amount of ray path degradation is dependant on the intensity of the internal waves.

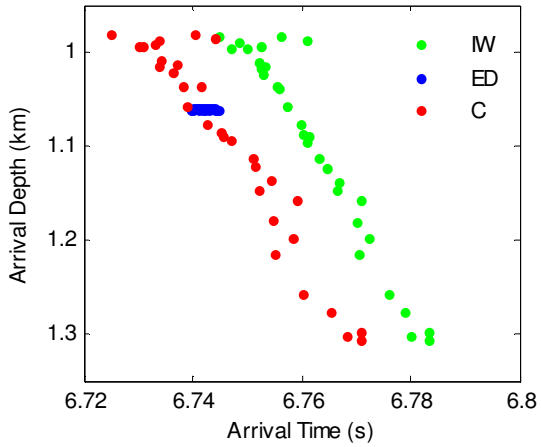

Figure 6-55: Timefront branch for all perturbation scenarios of Simulation 4.

Table 6-9: Summary of arrival predictions for Simulation 4.

	Delay (%)	Depth (%)
Eddy Field	0.2338	0.0942
Internal Waves	0.0636	3.8621
Combination	0.1643	3.7679

The intensity of the internal waves again demonstrates influence in spectral behavior. The spectra of the MTV at 10km in frequency space clearly show the combination environment spectrum to assume the shape of the internal wave spectrum. This increase of intensity causes a stronger dominance of the internal wave perturbation in the combination environment spectrum, thereby making any separation of contributions extremely difficult for this case.

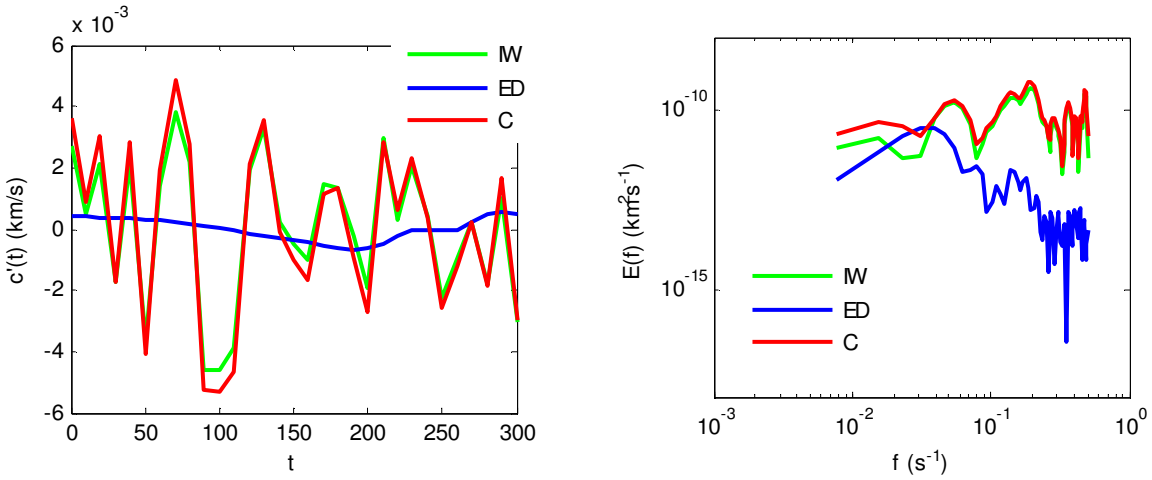

Figure 6-56: Turbulence, $\phi(0) = 0^\circ$. LEFT: Fluctuating MTV. Energy-frequency Spectrum.

7 CONCLUSION

This chapter offers a brief summary of the work described in this thesis report, which is accompanied by a discussion of the results presented in Chapter 6, followed by recommendations and suggestions for extending this research.

7.1 Summary and Discussion

The ocean acoustic channel creates strong amplitude and phase fluctuations in acoustic transmissions (long range and short range) used for underwater communications. These fluctuations can be induced by internal waves, turbulence, temperature gradients, density stratification or by other related phenomena that cause local perturbations in the sound speed. Received signal fluctuations arise from these medium fluctuations and cause the signal to oftentimes become unreadable. Underwater acoustic communications systems rely heavily on having prior knowledge of the underwater acoustic environment.

The ocean is a stratified medium containing several layers. The layer of interest is the thermocline, which hosts a large temperature gradient and thereby a region where the sound speed is at a minimum, the sound channel axis. The sound channel axis acts as a waveguide, sound speed increases linearly toward the ocean floor and increases exponentially toward the ocean surface. The ocean's sound speed is a function of depth, salinity, and temperature. It is represented by the canonical profile developed by Munk (1974), which accounts for the mentioned variability. Profile parameters were taken from the long range propagation experiment, the SLICE89.

The governing equations for the acoustic propagation model were derived from the wave equation which is simplified to the eikonal equation. The solution of the eikonal equation describes the behavior of ray trajectories and the travel time along them. For guided wave propagation the range can be viewed as the "time-step" variable, and the solution to the eikonal equation can be reduced to that of Hamiltonian form, known as the one-way ray equations, a set of second-order nonlinear differential equations.

Long Range Propagation

For long range propagation, transmission through an internal wave field is considered; this environment has been shown to cause ray chaos and associated stochastic properties. Previous models consider these nondeterministic effects and deterministic

effects individually. This internal wave model accounts for both by representing the field as a harmonic function with randomly perturbed phase and/or amplitude by additive Gaussian white noise.

Numerical analysis served as a means to justify our internal wave model and to demonstrate that the addition of random fluctuations leads to different characteristics in the acoustic arrivals during long range propagation, where it is believed that internal waves are the dominant source of acoustic fluctuations (Tang and Tappert 1997). The effect of noise intensity on chaotic ray behavior was examined through the construction of bifurcation and phase diagrams, Poincaré maps, and maximum propagation range and timefront plots.

It was demonstrated that long range wave propagation behaves differently in the presence of imperfectly periodic internal waves. Bifurcation diagrams verified the various regimes of sound ray behavior, showing that addition of random phase modulation results in almost immediate ray divergence. These imperfect internal waves also cause the distortion of Poincaré sections for a non-chaotic environment. In a chaotic environment the diagrams appear stable; it is the stochastic properties of this internal wave model that cause instability. Timefront plots demonstrated the multi-path structure that occurs in the ocean channel. The smearing of this predicted the arrival structure in the tail end of the timefront plots suggests the development of micro-folds and micro-caustics which significantly complicate the identification of signals. This study of 1000km range undisturbed underwater sound propagation has revealed that random phase fluctuations are responsible for poor propagation, indiscernible arrival structure, and in some cases surface intersection. This behavior is highly dependent on the intensity of the stochastic perturbations.

Short Range Propagation

Short range ray propagation was investigated using three simulated turbulence environments: internal waves, simulated eddy turbulence, and the combination of internal waves and eddy turbulence. Each vortex in the eddy field was characterized by two-dimensional potential vortex, with randomly assigned strength and location within the region of the sound channel axis and 10km propagation range. The number and

strengths of the vortices resulted in a turbulence intensity of about 10%. Internal waves were represented by the imperfectly harmonic forcing function.

A numerical study was done over two initial launch angles of $\phi(0) = 7.5^\circ$ and 0°, using both a stable and chaotic internal waves and a consistent eddy field for all simulations. The following conclusions are made based on predicted arrival structure observed from the timefront branch.

- ◊ The internal waves supply the majority of variation in arrival depth.
- ◊ The turbulent eddy field is primarily responsible for delay fluctuation.
- ◊ The combination environment hosts both fluctuations.
- ◊ The amount of ray path degradation is dependant on the intensity of the internal waves.
- ◊ The amount of temporal fluctuation is dependant of the location of eddies and initial launch angle.

One motivation for these simulations was to determine if there were any trends in the energy-frequency spectra that were common to each perturbation scenario, in order to provide a means to separate each contribution from the combination environment. The spectra of fluctuating MTV at 10km over time offered no clear distinction for this separation. However, it can be concluded that the internal waves are the dominant perturbation observed in the spectra. This observed internal wave dominance is dependent on the intensity of the wave.

It has been demonstrated that the predicted arrival patterns of rays traveling through ocean turbulence for long and short range propagation are dependant on initial conditions, intensity of the perturbations, and propagation distance. The results of these reference environments can serve as a prediction tool for transmitted signal behavior during underwater communication applications as well as the optimization of signal filters and hydrophone apertures.

7.2 Recommendations

The following is a categorized list of improvements that will further develop our acoustic propagation model.

Eddy Modeling Improvements:

- ◊ Change the rotation axes of eddy structures to have a vertical axis of rotation
- ◊ Vary the orientation of the eddy fields
- ◊ Propagate eddies with respect to the ambient current as well as mutually induced velocities from other vortices in the flow
- ◊ Obtain CTD data for typical temperature gradients observed in eddy fields and incorporate these fluctuations into the sound speed model

Internal Wave Modeling Improvements:

- ◊ Put GWN into the ODE function to allow for the deterministic condition to be included at every step of propagation

Other Modeling Improvements:

- ◊ Use CTD data to more accurately represent the sound speed structure of the ocean
- ◊ Model the transport equation to analyze how the amplitude of the signal will decay over the transmission subject to these environmental conditions
- ◊ Further develop the MATLAB code as a GUI (Graphical User Interface), to more easily create scenarios and to view the results more clearly

7.3 Future Work

This preliminary work with the suggested recommendations could ultimately be compared to hydrophone arrival data observed during long and short range propagation experiments to perceive the practicality of the model. This work would verify computational accuracy and offer the opportunity for further enhancement. Arrival formations, i.e. timefront plots, spectra, and new analysis on the signal structure could eventually be organized into a database to make the results more accessible for applications such as match-field processing.

8 REFERENCES

Alexandrou, A. (2001). *Principles of Fluid Mechanics* (1st ed.). Upper Saddle River, NJ: Prentice-Hall, INC.

Andreeva, T. A. (2003). Ultrasonic Technique in Determination of Grid-generated Turbulent Flow Characteristics. Unpublished PhD Dissertation, Worcester Polytechnic Institute, Worcester, MA.

Andreeva, T. A., Wojcik, S. E., & Durgin, W. W. (2005, May). *Influence of internal wave propagation on underwater wave propagation*. Paper presented at the 149th Meeting of the Acoustical Society of America, Vancouver, Canada.

Baggeroer, A. (1984). Acoustic Telemetry - An Overview. *Ieee Journal of Ocean Engineering, OE-9*(4), 229-235.

Beron-Vera, F., & Brown, M. (2003). Ray stability in weakly range-dependant sound channels. *Journal of the Acoustical Society of America, 114*(1), 123-130.

Beron-Vera, F., & Brown, M. (2004). Travel time stability in weakly range-dependant sound channels. *Journal of the Acoustical Society of America, 115*(3), 1068-1077.

Beron-Vera, F., Brown, M., Colosi J., Tomsovic., S., & Virovlyansky, A. (2003). Ray dynamics in a long range acoustic propagation experiment. *Journal of the Acoustical Society of America, 114*(3), 1226-1242.

Bleistein, N. (1984). *Mathematical Methods for Wave Phenomena* (1st ed.). San Francisco: Academic Press, INC.

Brekhovskikh, L. (1982). *Fundamentals of Ocean Acoustics* (G. Ecker, Ed.). Berlin, Germany: Springer-Verlag.

Brown, M., Colosi, J., Tomsovic, S., Virovlyansky, A. L., Wolfson, M. A., & Zaslavsky, G. (2005). Ray Dynamics in Ocean Acoustics. *Journal of the Acoustical Society of America, 113*(5), 2533-2547.

Brown, M., & Viechnicki, J. (1998). Stochastic ray theory for long-range sound propagation in deep ocean environments. *Journal of the Acoustical Society of America, 104*(4), 2090-2104.

Catipovic, J. (1990). Performance Limitations in Underwater Acoustic Telemetry. *Ieee Journal of Ocean Engineering, 15*(3), 205-216.

Chamberlin, S. (2005). Whirlpools in your bathtub. Retrieved January 30, 2006. http://www.oceansonline.com/ocean_currents.htm

Chernov, L. A. (1960). *Wave Propagation in a Random Medium* (1st ed., R. Silverman, Trans.). London: McGraw-Hill Book Company, Inc.

Colosi, J., Flatte, S., & Bracher, C. (1994). Internal wave effects on 1000-km oceanic acoustic pulse propagation: Simulation and comparison with experiment. *Journal of the Acoustical Society of America, 96*(1), 452-468.

D'Asaro, E., & Lien, R. (2000). Lagrangian Measurements of Waves and Turbulence in Stratified Flows. *Journal of Physical Oceanography, 30*, 641-654.

Duda, T., & Bowlin, J. (1994). Ray-acoustic caustic formation and timing effects from ocean sound-speed relative curvature. *Journal of the Acoustical Society of America, 96*(2-1), 1033-1046.

Duda, T., Flatte, S., Colosi, J., Cornuelle, B., Hildebrand, J. A., Hodgkiss, W., et al. (1992). Measured wave-front fluctuations in 1000-km pulse propagation in the Pacfic Ocean. *Journal of the Acoustical Society of America, 92*(1-1), 939-955.

Dushaw, B., Worcester, P., Cornuelle, B., & Howe, B. (1993). On equations for the speed of sound in seawater. *Journal of the Acoustical Society of America, 93*(1), 255-275.

Dzieciuch, M., Munk, W., & Rudnick, D. (2004). Propagation of sound through a spicy ocean, the SOFAR overture. *Journal of the Acoustical Society of America, 116*(3), 1447-1461.

Eggen, C., Howe, B., & Dushaw, B. (2002). A MATLAB GUI for Ocean Acoustic Propagation. *Ieee, 1*(1), 1415-1421.

EvoLogics (2006). Evologics – Hydro-acoustic modems with SC2 intelligent underwater telemetry. Retrieved January 30, 2006. http://www.naval-technology.com/contractors/navigation/evologics/

Flatte, S. (2002). Calculations of wave propagation through statistical random media, with and without a waveguide. *Optics Express, 10*(16), 777-804.

Flatte, S. (1983). Principles of Acoustic Tomography of Internal Waves. *Ieee, 1*(1), 372-377.

Gendron, P. (2005). Estimating mutual information for the underwater acoustic channel. Manuscript in preparation, Naval Research Laboratory, Washington, DC.

Gill, A. (1982). *Atmosphere-ocean dynamics*. New York: Academic Press.

Gitterman, M. (1999). Simple treatment of correlated multiplicative noise and additive noises. *Journal of Physics and Applied Math, 32*, L293-L297.

Hegewisch, K., Cerruiti, N., & Tomsovic, S. (2005). Ocean acoustic wave propagation and ray methods correspondence: Internal wave fine structure. *Journal of the Acoustical Society of America, 117*(3), 1582-1594.

Henyey, F., Rouseff, D., Grochocinski, J., Reynolds, S., Williams, K., & Ewart, T. (1997). Effects of Internal Waves and Turbulence on Horizontal Aperture Sonar. *Ieee, 22*(2), 270-279.

Hinze, J. O. (1959). *Turbulence* (1st ed.). New York: McGraw-Hill Book Company, INC.

Holden, A. (1986). *Chaos* (1st ed.). Princeton, NJ: Princeton University Press.

Jarrot, C. Ioana., & A. Quinquis. (2005). De-noising Underwater Signals Propagating Through Multi-path Channels. *Oceans, 1*(1), 1-6.

Jenson, F., Kuperman, W., Porter, M., & Schmidt, H. (1994). *Computational Ocean Acoustics* (1st ed.) [Computational Ocean Acoustics]. Woodbury, NY: AIP Press.

Lathi, B. P. (1998). *Signal Processing and Linear Systems* (1st ed.). Carmichael, CA: Berkeley-Cambridge Press.

Kilfoyle, D., & Baggeroer, A. (2000). The State of the Art in Underwater Acoustic Telemetry. *Ieee Journal of Ocean Engineering, 25*(1), 4-27.

Lvov, Y., & Tabak, E. (2001). Hamiltonian formalism and the Garrett-Munk spectrum of internal waves in the ocean. *Prl, 87*, 1-5.

Mathworks (2006). MATLAB Function Reference. Retrieved January 31, 2006. http://www.mathworks.com/access/helpdesk/help/techdoc/ref/ref.html

Munk, W. (1974). Sound Channel in an exponentially stratified ocean, with application to SOFAR. *Journal of the Acoustical Society of America, 55*(2), 220-226.

NASA (2005). Visible Earth. Retrieved January 30, 2006. http://visibleearth.nasa.gov

NOAA (1997). Eddy finding in the Bering Sea. Retrieved January 30, 2006. http://www.pmel.noaa.gov/sebscc/results/stabeno/eddy_finding.html

NOAA/EPIC (2005). Oceanographic In-Situ Data Access. Retrieved January 30, 2006. http://www.epic.noaa.gov/epic/ewb/ewb_epicselect.htm

Pope, S. (2000). *Turbulent Flows* (1st ed.). Cambridge, MA: Cambridge University Press.

Simmen, J., & Flatte, S. (1999). Near-caustic behavior in a 270-km acoustical experiment. *Journal of the Acoustical Society of America, 105*(6-1), 323-3244.

Simmen, J., Flatte, S., & Wang, G. (1997). Wavefront folding, chaos, and diffraction for sound propagation through ocean internal waves. *Journal of the Acoustical Society of America, 102*(1), 235-255.

Stewart, R. (1969). Turbulence and waves in a stratified atmosphere. *Radio Scientific, 4*, 1269-1278.

Smith, K., Brown, M., & Tappert, F. (1992). Acoustic ray chaos induced by mesoscale ocean structure. *Journal of the Acoustical Society of America, 91*(4-1), 1950-1959.

Symth, W., & Moum, J. (2000). Length Scales of Turbulence in Stably Stratified Mixing Layes. *Physics of Fluids, 12*, 1327-1342.

Smyth, W. D., & Moum, J. N. (2000). 3D Turbulence. *Academic Press Encyclopedia of Ocean Sciences*.

Tang, X., & Tappert, F. (1997). Effects of Internal Waves on Sound Pulse Propagation in the Straits of Florida. *Ieee Journal of Ocean Engineering, 22*(2), 245-255.

Tatarski, V. (1961). *Wave Propagation in a Turbulent Medium* (1st ed., R. Silverman, Trans.). New York: McGraw-Hill Book Company, INC.

Taroudakis, M., & Markaki, M. (1997). On the use of matched-field processing and hybrid algorithms for vertical slice tomography. *Journal of the Acoustical Society of America, 102*(2-1), 885-895.

Tennekes, H., & Lumley, J. (1972). *A First Course in Turbulence* (1st ed.). Cambridge, MA: The MIT Press.

Tomczak, M. (1996). Internal Waves. Unpublished manuscript, Oregon State University, Corvallies, OR.

Wadzuk, B., & Hodges, B. (2004). Comparing Hydrostatic and Non-hydrostatic Navier Stokes Models of Internal Waves. Unpublished manuscript, Office of Naval Research, Washington, Washington D.C.

Weber, F. (2003). Ultrasonic Beam Propagation in Turbulent Flow. Unpublished PhD Dissertation, Worcester Polytechnic Institute, Worcester, MA.

White, F. (2006). *Viscous Fluid Flow* (3rd ed.). New York: McGraw Hill. (Original work published 1974)

Wiercigroch, M., Badiey, M., Simmen, J., & Cheng, A. (1999). Non-Linear Dynamics of Underwater Acoustics. *Journal of Sound and Vibration, 220*(5), 771-786.

Worcester, P., & Spindel, R. (2005). North Pacific Acoustic Laboratory. *Journal of the Acoustical Society of America, 117*(3-2), 1499-1510.

Zaslavsky, G., & Abullaev, S. (1997). Chaotic Transmission of waves and "cooling" of signals. *Chaos, 7*(1), 182-186.

Zaslavsky, G., & Edelman, M. (1997). Self-similarity, renormalization, and phase space non-uniformity of Hamiltonian chaotic dynamics. *Chaos, 7*(1), 159-181.

Appendix I – bifurcation.m

```
% Stefanie Wojcik
% Last Modified 01/31/2006
% This program constructs bifucrcation diagrams for varying IW
% wavelength or varying IW amplitude.  Noise can be added to either the
% wavelength, amplitude, or both simultaneously.

close all
clear all

global B za co c_ch ep A R D rspan noiseA noiseR

% User Inputs*************************************************************
method = input('Choose your scenario:\n1 - Varying IW Wavelength\n2 -
Varying IW Amplitude\n');
noise = input('Noise:\n1 - R only\n2 - A only\n3 - both\n4 - no
noise\n');
if noise < 3
    D = input('Enter a value for SNR (5dB, 15dB, 25dB) : \n');
    D1 = D; D2 = D;
end
if noise == 3
    D1 = input('Enter a value for SNR in R (5dB, 15dB, 25dB) : \n');
    D2 = input('Enter a value for SNR in A (5dB, 15dB, 25dB) : \n');
end
% Sound Speed Constants**************************************************
c_ch = 1.48;                        % SS at sound channel axis (km/s)
ep = 0.0074;                        % perturbation coefficient
B = 1;                              % Scale Depth (km)
za = 1;                             % depth at the sound channel axis
(km)
co = 1.49;                          % reference sound speed (km/s)
% IW Parameters**********************************************************
A = 0.005;                             % Internal Wave Amplitude
R = 11.2;                                 % Internal Wave Wavelength
phi0 = 7.5;                            % Initial deployment angle
%************************************************************************

if method == 1
    for R = [1:0.2:30]
        fprintf('R : %g \n',R)
        % Initial Conditions*************************************************
        z0 = 0.8;                               % Initial depth (km)
        P0 = tand(phi0);                        % Initial ray momentum
(degrees)
        q0 = 0;                                 % Initial phase
        T0 = 0;                                 % Initial time (s)
        % Noise for IW*******************************************************
        if noise == 1
            noiseR = awgn((2*pi/R),D1); noiseA = A;
        elseif noise == 2
            noiseR = 2*pi/R; noiseA = awgn(A,D2);
```

```
        elseif noise == 3
            noiseR = awgn((2*pi/R),D1); noiseA = awgn(A,D2);
        elseif noise == 4
            noiseR = 2*pi/R; noiseA = A;
        end
        % ODE45*****************************************************
        rstep = 1; rinital = 0; rfinal = 1000;
        x = [z0; P0; q0; T0];
        options = odeset('RelTol',1e-9,'AbsTol',1e-9);
        rspan = [rinital: rstep: rfinal];
        [r,y] = ode45('oceanequations_IW',rspan,x,options);
        z = y(:,1);
        p = y(:,2);
        q = y(:,3);
        phi = atand(p);
        % Peaks*****************************************************
        [peak,index] = peakfinder(p);
        for i=1:length(index)
            znew(i)=z(index(i));
        end
        % Plots*****************************************************
        figure(1)
        plot(R,znew,'k.','MarkerSize',15)
        title('Bifurcation Diagram, z=f(R)')
        xlabel('R (km)'), ylabel('z (km)'),axis ij, hold on, grid on
    end
else
    for A = [.001:0.001:0.03]
        fprintf('A : %g \n',A)
        % Initial Conditions*****************************************
        z0 = 0.8;                           % Initial depth (km)
        P0 = tand(phi0);                    % Initial ray momentum
(degrees)
        q0 = 0;                             % Initial phase
        T0 = 0;                             % Initial time (s)
        % Noise for IW***********************************************
        if noise == 1
            noiseR = awgn((2*pi/R),D); noiseA = A;
        elseif noise == 2
            noiseR = 2*pi/R; noiseA = awgn(A,D);
        elseif noise == 3
            noiseR = awgn((2*pi/R),D); noiseA = awgn(A,D);
        elseif noise == 4
            noiseR = 2*pi/R; noiseA = A;
        end
        % ODE45*****************************************************
        rstep = 1; rinital = 0; rfinal = 1000;
        x = [z0; P0; q0; T0];
        options = odeset('RelTol',1e-9,'AbsTol',1e-9);
        rspan = [rinital: rstep: rfinal];
        [r,y] = ode45('oceanequations2',rspan,x,options);
        z = y(:,1);
        p = y(:,2);
        q = y(:,3);
        phi = atand(p);
        % Peaks*****************************************************
        [peak,index] = peakfinder(p);
```

```
        for i=1:length(index)
            znew(i)=z(index(i));
        end
        % Plots*****************************************************
        figure(1)
        plot(A,znew,'k.','MarkerSize',15)
        title('Bifurcation Diagram, z=f(A)')
        xlabel('A (km)'), ylabel('z (km)'),axis ij, hold on, grid on
    end
end
```

Appendix II - poincare.m

```
% Stefanie Wojcik
% Last Modified 01/31/2006
% This program constructs poincare sections with for varying initial
% launch angles.  Noise can be added to either then wavelength,
% amplitude, or both simultaneously.

close all
clear all

global B za co c_ch ep A R D rspan noiseA noiseR

noise = input('Stochastic scenario:\n1 - R only\n2 - A only\n3 -
both\n4 - no noise\n')
if noise < 4
    D = input('Enter a value for SNR (2dB, 25dB, 50dB) : \n')
end
% Sound Speed Constants*************************************************
c_ch = 1.48;                        % SS at sound channel axis (km/s)
ep = 0.0074;                        % perturbation coefficient
B = 1;                              % Scale Depth (km)
za = 1;                             % depth at the sound channel axis
(km)
co = 1.49;                          % reference sound speed (km/s)
% IW Parameters*********************************************************
A = 0.005;                          % Internal Wave Amplitude
R = 1;                              % Internal Wave Wavelength
%***********************************************************************

for phi0 = [7:0.2:15]
    fprintf('phi0 : %g \n',phi0)
    % Initial Conditions************************************************
    z0 = 0.8;                           % Initial depth (km)
    P0 = tand(phi0);                    % Initial ray momentum
(degrees)
    q0 = 0;                             % Initial phase
    T0 = 0;                             % Initial time (s)
    % Noise*************************************************************
    if noise == 1
        noiseR = awgn((2*pi/R),D); noiseA = A;
    elseif noise == 2
        noiseR = 2*pi/R; noiseA = awgn(A,D);
    elseif noise == 3
        noiseR = awgn((2*pi/R),D); noiseA = awgn(A,D);
    elseif noise == 4
        noiseR = 2*pi/R; noiseA = A;
    end
    % ODE45 ************************************************************
    rstep = 1; rinital = 0; rfinal = 1000;
    x = [z0; P0; q0; T0];
    options = odeset('RelTol',1e-9,'AbsTol',1e-9);
    rspan = [rinital: rstep: rfinal];
    [r,y] = ode45('oceanequations_IW',rspan,x,options);
```

```
    z = y(:,1);
    p = y(:,2);
    q = y(:,3);
    phi = atand(p);
    m = length(y);
    % Peaks***************************************************************
    [peak,index] = peakfinder(p);
    for i=1:length(index)
        znew(i)=z(index(i));
        phinew(i)=phi(index(i));
    end
    % Plots***************************************************************
    figure(1)
    plot(phi,z,'k')
    title('Poincare Section')
    xlabel('phi'), ylabel('z (km)'),axis ij, hold on, grid on
end
```

Appendix III – phase.m

```
% Stefanie Wojcik
% Last Modified 01/31/2006
% This program constructs phase planes for specific values of IW
% wavelength and amplitude.
close all
clear all

global B za co c_ch ep A R D rspan noiseA noiseR
% Sound Speed Constants*********************************************
c_ch = 1.48;                        % SS at sound channel axis (km/s)
ep = 0.0074;                        % perturbation coefficient
B = 1;                              % Scale Depth (km)
za = 1;                             % depth at the sound channel axis
co = 1.49;                          % reference sound speed (km/s)
%  IW Parameters*****************************************************
A = 0.005;                          % Internal Wave Amplitude
R = 11.2;                           % Internal Wave Wavelength
% Initial Conditions************************************************
phi0 = 7.5;                           % Initial launch angle
z0 = 0.8;                             % Initial depth (km)
P0 = tand(phi0);                      % Initial ray momentum (degrees)
q0 = 0;                               % Initial phase
T0 = 0;                               % Initial time (s)
% Noise*************************************************************
noise = input('Stochastic scenario:\n1 - R only\n2 - A only\n3 -
both\n4 - no noise\n')
if noise < 4
    D = input('Enter a value for SNR (2dB, 25dB, 50dB) : \n')
end
if noise == 1
    noiseR = awgn((2*pi/R),D); noiseA = A;
elseif noise == 2
    noiseR = 2*pi/R; noiseA = awgn(A,D);
elseif noise == 3
    noiseR = awgn((2*pi/R),D); noiseA = awgn(A,D);
elseif noise == 4
    noiseR = 2*pi/R; noiseA = A;
end
% ODE45 ************************************************************
rstep = 1; rinital = 0; rfinal = 1000;
x = [z0; P0; q0; T0];
options = odeset('RelTol',1e-9,'AbsTol',1e-9);
rspan = [rinital: rstep: rfinal];
[r,y] = ode45('oceanequations_IW',rspan,x,options);
z = y(:,1);
p = y(:,2);
phi = atand(p);
% Plots*************************************************************
figure(1)
plot(phi,z,'b','linewidth',1)
title('Phase Diagram')
xlabel('phi'), ylabel('z (km)'),axis ij, grid on
```

Appendix IV – Timefront_iw.m

```
% Stefanie Wojcik
% Last Modified: 01/31/2006
% This program constructs the timefront plots for long range propgation
% through an internal wave field
clear all
close all

global B za co c_ch ep rspan A R noiseA noiseR

% Sound Speed Constants*************************************************
c_ch = 1.48;                            % SS at sound channel axis
(km/s)
ep = 0.0074;                            % perturbation coefficient
B = 1;                                  % Scale Depth (km)
za = 1;                                 % depth of sound channel axis
(km)
co = 1.49;                              % reference sound speed (km/s)
%IW Parameters*********************************************************
R = 8.2;                                % IW Wavelength
A = 0.005;                              % IW Amplitude
D = 100;                                % SNR
i = 0;                                  % counter
%**********************************************************************
for phi0 = [-12:0.1:12]
    i = i+1;
    fprintf('phi_0 : %g \n',phi0)
    % Noise*****************************************************
    noiseR = awgn((2*pi/R),D);  % Noise in Wavelength
    noiseA = awgn(A,D); ;       % Noise in Amplitude
    % ODE45 ****************************************************
    z0 = 0.8;                                       % Source depth (km)
    P0 = tand(phi0);                                % Initial ray
    T0 = 0;                                         % Initial Time
    q0 = 0;                                         % Initial IW phase
    rstep = 1; rinital = 0; rfinal = 1000;
    x = [z0; P0; q0; T0];
    options = odeset('RelTol',1e-9,'AbsTol',1e-9);
    rspan = [rinital: rstep: rfinal];
    [r,yiw] = ode45('oceanequations_IW',rspan,x,options);
    ziw = yiw(:,1);
    piw = yiw(:,2);
    qiw = yiw(:,3);
    Tiw = yiw(:,4);
    phiiw = atan(piw);
    m = length(r);
    time_iw(i,:) = [Tiw(m) ziw(m) piw(m)];
    figure(2), plot(Tiw(m),ziw(m),'k.','Markersize',12)
    title('Timefront'),xlabel('Arrival time'), ylabel('arrival depth')
    axis ij, hold on,grid on
    figure(1), plot(piw(m),ziw(m),'b.')
end
save timefront_iw.dat time_iw -ascii
```

Appendix V – realizations_short.m

```
% Stefanie Wojcik
% Last Modified: 02/14/2006
% The program simulates a traveling pulse through the following
% scenarios: an ocean with a sound sped profile only, an ocean with a
% random eddy field of turbulence of the inertial subrange, an ocean
% with a field of internal waves, and an ocean with a random eddy field
% and an internal wave field.
clear all
close all

global B za co c_ch ep rspan
global A R noiseA noiseR
global z_eddy r_eddy gamma n

% Timeseries Variables*************************************************
no_real = 300;                  % Number of samples
dr = 10;                         % Step size
real = [0:dr:no_real];
% Sound Speed Constants************************************************
c_ch = 1.48;                            % SS at sound channel axis (km/s)
ep = 0.0074;                            % perturbation coefficient
B = 1;                                  % Scale Depth (km)
za = 1;                                 % depth of sound channel axis
(km)
co = 1.49;                              % reference sound speed (km/s)
rstep = 1; rinital = 0; rfinal = 10;  % propagation distance (km)
U = .0005;                              % Mean speed of flow (km/s)
% IW Parameters********************************************************
R = 1;                           % IW Wavelength
A = 0.005;                       % IW Amplitude
D = 30;                          % SNR
% Random Eddies********************************************************
n = 50;                            % Number of eddies
nrvor = 1; nz = 1.2; nr = rfinal; % Scale for depth, range, diameter
nV = 0.00001;
% Creating random locations, diameters, and indicies for CCW circ.
z_eddy = (nz.*rand(n,1));
r_eddy = (nr.*rand(n,1));
rvor = (nrvor.*rand(n,1));
index = ceil(n.*rand((2*(n-1))/2,1));
V = (nV.*rand(n,1));
fprintf('            Eddy Parameters               \n')
fprintf('r_vortex               Circulation          r-position
z-position\n')
for j = 1:n
    gamma(j) = V(j)*2*pi*rvor(j);
end
for j = 1:n
    for i=1:length(index)
        gamma(index(i)) = -gamma(index(i));
    end
```

```
        fprintf('%g         %g          %g
%g\n',rvor(j),gamma(j),r_eddy(j),z_eddy(j))
        ed_info(j,:) = [rvor(j) gamma(j) r_eddy(j) z_eddy(j)];
end
k = 0;
for i = [0:dr:no_real]
    fprintf('realization no : %g \n',i)
    k = k+1;
    %Eddy position*********************************************************
    for j=1:n
        r_eddy(j) = r_eddy(j) + U*i;
    end
    % Noise*****************************************************************
    noiseR = awgn((2*pi/R),D);  % Noise in Wavelength
    noiseA = awgn(A,D); ;       % Noise in Amplitude
    % ODE45*****************************************************************
    phi0 = 7.5;                                     % Initial launch angle
    z0 = 0.8;                                       % Source depth (km)
    P0 = tand(phi0);                                % Initial ray momentum
    T0 = 0;                                         % Initial Time
    q0 = 0;                                         % Initial IW phase
    x_2 = [z0; P0; T0];
    x = [z0; P0; q0; T0];
    options = odeset('RelTol',1e-9,'AbsTol',1e-9);
    rspan = [rinital: rstep: rfinal];
    % Sound Speed Perturbation Only
    [r,yss] = ode45('oceanequations_SS',rspan,x_2,options);
    zss = yss(:,1);
    Tss = yss(:,3);
    pss = yss(:,2);
    m = length(r);
    time_ss(k,:) = [Tss(m) zss(m) pss(m)];
    figure(1), plot(r,zss,'r','linewidth',2),xlabel('r km'), ylabel('z
km'), axis ij
    % IW Only
    [r,y] = ode45('oceanequations_IW',rspan,x,options);
    z = y(:,1);
    p = y(:,2);
    q = y(:,3);
    T = y(:,4);
    m = length(r);
    time_iw(k,:) = [T(m) z(m) p(m)];
    % Eddy Field
    [r,ye] = ode45('oceanequations_ED',rspan,x_2,options);
    ze = ye(:,1);
    pe = ye(:,2);
    Te = ye(:,3);
    m = length(r);
    time_ed(k,:) = [Te(m) ze(m) pe(m)];
    for j=1:m
        [ufluct(j),vfluct(j),fluct(j)] = eddy1(r(j),z0);
        fluct_u(k,j) = [ufluct(j)];
        fluct_v(k,j) = [vfluct(j)];
    end
  % IW & Eddy Combo
    [r,yc] = ode45('oceanequations_COMBO',rspan,x,options);
    zc = yc(:,1);
```

```
    pc = yc(:,2);
    qc = yc(:,3);
    Tc = yc(:,4);
    m = length(r);
    time_combo(k,:) = [Tc(m) zc(m) pc(m)];
end
save time_ed.dat time_ed -ascii
save time_ss.dat time_ss -ascii
save time_combo.dat time_combo -ascii
save time_iw.dat time_iw -ascii
save ufluct.dat fluct_u -ascii
save vfluct.dat fluct_v -ascii
save ed_info.dat ed_info -ascii
```

Appendix VI – spectrum.m

```
% Stefanie Wojcik
% Last Revised on 02/01/2006
% This Program calculated the fluctuating MTV spectrum for each
% turbulent enviornment based on several realizations of the arrival
% time
clear all
close all

global rfinal

rfinal = 10;
no = [0:10:300];
real = [1:1:length(no)];

load time_ss.dat
Tss = time_ss(:,1);
zss = time_ss(:,2);
[Ess,fss,Uflss] = spec_param(Tss);
figure(4)
subplot(2,2,1),plot(fss,Ess,'m'),hold on
xlabel('f (sec^-1)'),ylabel('E(f) (km^3/s^2)')
subplot(2,2,2),loglog(fss,Ess,'m','linewidth',2),hold on
xlabel('k (km^-1)'),ylabel('E(k) (km^3/s^2)')
subplot(2,2,3),plot(real,Uss,'m'),hold on
xlabel('t'),ylabel('c''(t)'),hold on
subplot(2,2,4),plot(Tss,zss,'m.'), axis ij, hold on
xlabel('Arrival Time (s)'),ylabel('Arrival Depth (km)')

load time_iw.dat
Tiw = time_iw(:,1);
meanTiw = mean(Tiw)
stdTiw = std(Tiw)
ziw = time_iw(:,2);
meanziw = mean(ziw)
stdziw = std(ziw)
[Eiw,fiw, Ufliw] = spec_param(Tiw);
load time_ed.dat
Ted = time_ed(:,1);
meanTed = mean(Ted)
stdTed = std(Ted)
zed = time_ed(:,2);
meanzed = mean(zed)
stdzed = std(zed)
[Eed,fed, Ufled] = spec_param(Ted);
load time_combo.dat
Tc = time_combo(:,1);
meanTc = mean(Tc)
srdTc = std(Tc)
zc = time_combo(:,2);
meanzc = mean(zc)
stdzc = std(zc)
```

```
[Ec,fc,Uflc] = spec_param(Tc);

figure(1)
loglog(fiw,Eiw,'g','linewidth',2),hold on
loglog(fed,Eed,'b','linewidth',2),hold on
loglog(fc,Ec,'r','linewidth',2),hold on
xlabel('f (s^-^1)'),ylabel('E(f) (km^2s^-^1)')
legend('IW','ED','C',2)

figure(2)
plot(no,Ufliw,'g','linewidth',2), hold on
plot(no,Ufled,'b','linewidth',2), hold on
plot(no,Uflc,'r','linewidth',2), hold on
xlabel('t'),ylabel('c''(t) (km/s)')
legend('IW','ED','C',2)

figure(3)
plot(Tiw,ziw,'g.','markersize',10), axis ij, hold on
plot(Ted,zed,'b.','markersize',10), axis ij, hold on
plot(Tc,zc,'r.','markersize',10), axis ij, hold on
xlabel('Arrival Time (s)'),ylabel('Arrival Depth (km)')
legend('IW','ED','C',2)
```